Sources of Seismic Hazard in British Columbia: What Controls Earthquakes in the Crust?

by

Natalie Joy Balfour
B.Sc., Victoria University of Wellington, 2002
M.Sc., Victoria University of Wellington, 2005

A Dissertation Submitted in Partial Fulfillment of the
Requirements for the Degree of

DOCTOR OF PHILOSOPHY

in the School of Earth and Ocean Sciences

Sources of Seismic Hazard in British Columbia: What Controls Earthquakes in the Crust?

by

Natalie Joy Balfour

B.Sc., Victoria University of Wellington, 2002

M.Sc., Victoria University of Wellington, 2005

Supervisory Committee

Dr. J. F. Cassidy, Co-Supervisor

(School of Earth and Ocean Sciences)

Dr. S. E. Dosso, Co-Supervisor

(School of Earth and Ocean Sciences)

Dr. G. Rogers, Committee Member

(School of Earth and Ocean Sciences)

Dr. M. Lefebvre, Outside Member

(Department of Physics and Astronomy)

Supervisory Committee

Dr. J. F. Cassidy, Co-Supervisor
(School of Earth and Ocean Sciences)

Dr. S. E. Dosso, Co-Supervisor
(School of Earth and Ocean Sciences)

Dr. G. Rogers, Committee Member
(School of Earth and Ocean Sciences)

Dr. M. Lefebvre, Outside Member
(Department of Physics and Astronomy)

ABSTRACT

This thesis examines processes causing faulting in the North American crust in the northern Cascadia subduction zone. A combination of seismological methods, including source mechanism determination, stress inversion and earthquake relocations are used to determine where earthquakes occur and what forces influence faulting. We also determine if forces that control faulting can be monitored using seismic anisotropy. Investigating the processes that contribute to faulting in the crust is important because these earthquakes pose significant hazard to the large population centres in British Columbia and Washington State.

To determine where crustal earthquakes occur we apply double-difference earthquake

relocation techniques to events in the Fraser River Valley, British Columbia, and the San Juan Islands, Washington. This technique is used to identify "hidden" active structures using both catalogue and waveform cross-correlation data. Results have significantly reduced uncertainty over routine catalogue locations and show lineations in areas of clustered seismicity. In the Fraser River Valley these lineations or streaks appear to be hidden structures that do not disrupt near-surface sediments; however, in the San Juan Islands the identified lineation can be related to recently mapped surface expressions of faults.

To determine forces that influence faulting we investigate the orientation and sources of stress using Bayesian inversion results from focal mechanism data. More than ∼600 focal mechanisms from crustal earthquakes are calculated to identify the dominant style of faulting and inverted to estimate the principal stress orientations and the stress ratio. Results indicate the maximum horizontal compressive stress (S_{Hmax}) orientation changes with distance from the subduction interface, from margin-normal along the coast to margin-parallel further inland. We relate the margin-normal stress direction to subduction-related strain rates due to the locked interface between the North America and Juan de Fuca plates just west of Vancouver Island. Further from the margin the plates are coupled less strongly and the margin-parallel S_{Hmax} relates to the northward push of the Oregon Block. Active faults around the region are generally thrust faults that strike east-west and might accommodate the margin-parallel compression.

Finally, we consider whether crustal anisotropy can be used as a stress monitoring tool in this region. We identify sources and variations of crustal anisotropy using shear-wave splitting analysis on local crustal earthquakes. Results show spatial variations in fast directions, with margin-parallel fast directions at most stations and

margin-perpendicular fast directions at stations in the northeast of the region. To use seismic anisotropy as a stress indicator requires identifying which stations are primarily influenced by stress. We determine the source of anisotropy at each station by comparing fast directions from shear-wave splitting results to the S_{Hmax} orientation. Most stations show agreement between these directions suggesting that anisotropy is stress-related. These stations are further analysed for temporal variations and show variation that could be associated with earthquakes (M_L 3–5) and episodic tremor and slip events.

The combination of earthquake relocations, source mechanisms, stress and anisotropy is unique and provides a better understanding of faulting and stress in the crust of northern Cascadia.

Contents

Supervisory Committee **ii**

Abstract **iii**

Table of Contents **vi**

List of Tables **ix**

List of Figures **x**

Acknowledgements **xv**

Dedication **xvi**

1 Introduction **1**

1.1 Objectives 1

1.1.1 Where do large crustal earthquakes occur? 2

1.1.2 What forces influence faulting? 3

1.1.3 Can we monitor forces that influence faulting using seismic anisotropy? 4

1.2 Tectonic Setting 4

1.3 Motivation 8

1.4 Outline of Thesis 10

2 Identifying Active Structures from Earthquake Relocations 12

2.1 Introduction . . . 13

2.2 Double-Difference Relocation . . . 16

2.2.1 Catalogue Arrival Times . . . 17

2.2.2 Waveform Cross Correlation . . . 18

2.3 Data . . . 20

2.3.1 Networks . . . 20

2.3.2 Standard Locations and Velocity Models . . . 21

2.4 Results . . . 23

2.4.1 Fraser Valley, British Columbia . . . 23

2.4.2 San Juan Islands, Washington . . . 27

2.5 Related Focal Mechanisms and Fault Data . . . 32

2.6 Conclusions . . . 34

3 Mapping Crustal Stress and Strain in Southwest British Columbia 37

3.1 Introduction . . . 38

3.1.1 Previous Studies . . . 40

3.2 Focal Mechanism Determination . . . 43

3.2.1 Focal Mechanism Results . . . 44

3.3 Stress Inversion . . . 48

3.3.1 Bayesian Method . . . 49

3.3.2 Stress Results . . . 50

3.4 Comparison with GPS Strain Rates . . . 54

3.5 Implications for Understanding Tectonics . . . 57

3.6 Conclusions . . . 60

4 Crustal Anisotropy in the Forarc of the Cascadia subduction zone, British Columbia **62**

4.1 Introduction . . . 63

4.1.1 Tectonics . . . 63

4.1.2 Measuring Anisotropy . . . 65

4.1.3 Causes of Crustal Anisotropy . . . 66

4.1.4 Previous Studies . . . 67

4.2 Shear-wave Splitting . . . 68

4.2.1 Data . . . 71

4.3 Results . . . 71

4.3.1 Spatial Variation in Fast Direction . . . 72

4.3.2 Depth Variation in Delay Times . . . 74

4.4 Discussion . . . 76

4.4.1 Comparison with Stress . . . 76

4.4.2 Temporal Variations . . . 83

4.5 Conclusions . . . 87

5 Summary **88**

5.1 Where do large earthquakes occur? . . . 88

5.2 What forces influence faulting? . . . 91

5.3 Can we monitor these forces using anisotropy? . . . 93

5.4 Conclusions . . . 95

Bibliography **98**

A Stress Inversion Results **113**

B Splitting Results **131**

List of Tables

Table 3.1 Quality grades for focal mechanisms. 50

Table A.1 S_{Hmax} and e_{Hmax} values for each cluster, including 95% confidence limit for S_{Hmax} and standard error for e_{Hmax}. Clusters 8, 9 and 26 are omitted as they contained too few (<4) focal mechanisms to perform the stress inversion. 114

Table B.1 Summary of splitting results observed at each station. 132

List of Figures

Figure 1.1 Tectonics of the Cascadia subduction zone. 5
Figure 1.2 Seismicity of northern Cascadia. 7

Figure 2.1 Map of study regions investigated using earthquake relocations. 14
Figure 2.2 Map of faults and seismicity in southwest British Columbia and northwest Washington state. 15
Figure 2.3 Example of cross-correlated waveforms for P- and S-waves recorded at station PGC 19
Figure 2.4 P-wave velocity models used for earthquake relocations. 22
Figure 2.5 Seismicity and stations used for earthquake relocations in the Fraser River Valley. 23
Figure 2.6 Double-difference earthquake relocations for the Fraser Valley region. 24
Figure 2.7 Double-difference earthquake relocations for a subset of 84 events in the Fraser Valley region. 26
Figure 2.8 Seismicity and stations used for earthquake relocations in the San Juan Islands. 28
Figure 2.9 Double-difference earthquake locations for the San Juan Islands. 30
Figure 2.10 Comparison of earthquake relocations with focal mechanisms and recently mapped faults. 33

Figure 3.1 Map of study region for crustal stress and strain. 39

Figure 3.2 Map of source mechanisms from previous studies. 41
Figure 3.3 Map of focal mechanisms determined in this study. 45
Figure 3.4 Ternary plot of focal mechanisms. 46
Figure 3.5 Map of all focal mechanisms coloured according to rake. . . . 47
Figure 3.6 Example of output from Bayesian stress inversion 51
Figure 3.7 Map of S_{Hmax} from stress inversion results. 52
Figure 3.8 Map of S_{Hmax} and associated uncertainties. 53
Figure 3.9 Ternary plot of stress inversion results. 53
Figure 3.10 Observed GPS velocity field and smoothed velocities used to derive strain rates. 55
Figure 3.11 Map comparing S_{Hmax} and e_{Hmax} for subduction models with different amounts of locking. 58
Figure 3.12 Cartoon summary of the dominant stress orientations. 59

Figure 4.1 Map of the study region used for anisotropy. 64
Figure 4.2 Map of the stations locations used for shear-wave splitting measurements and major faults. 65
Figure 4.3 Illustration of shear-wave splitting through an anisotropic medium. 66
Figure 4.4 Example of diagnostic plot from shear-wave splitting analysis. 70
Figure 4.5 Map and cross-section of earthquakes used for shear-wave splitting analysis. 72
Figure 4.6 Mean and standard deviation of fast directions observed at each station. 73
Figure 4.7 Circle plots of fast direction (black bands) with back-azimuth and incidence angle. 74
Figure 4.8 Delay time with error and normalised delay time with depth . 75
Figure 4.9 Map showing comparing fast direction results and S_{Hmax}. . . . 77

Figure 4.10 Regions and stations discussed in the interpretation of the source of anisotropy. 79
Figure 4.11 Temporal variations observed at station OZB. 84
Figure 4.12 Temporal variations observed at station SNB 86

Figure A.1 Stress inversion result for cluster 1. 115
Figure A.2 Stress inversion result for cluster 2. 115
Figure A.3 Stress inversion result for cluster 3. 116
Figure A.4 Stress inversion result for cluster 4. 116
Figure A.5 Stress inversion result for cluster 5. 117
Figure A.6 Stress inversion result for cluster 6. 117
Figure A.7 Stress inversion result for cluster 7. 118
Figure A.8 Stress inversion result for cluster 10. 118
Figure A.9 Stress inversion result for cluster 11. 119
Figure A.10 Stress inversion result for cluster 12. 119
Figure A.11 Stress inversion result for cluster 13. 120
Figure A.12 Stress inversion result for cluster 14. 120
Figure A.13 Stress inversion result for cluster 15. 121
Figure A.14 Stress inversion result for cluster 16. 121
Figure A.15 Stress inversion result for cluster 17. 122
Figure A.16 Stress inversion result for cluster 18. 122
Figure A.17 Stress inversion result for cluster 19. 123
Figure A.18 Stress inversion result for cluster 20. 123
Figure A.19 Stress inversion result for cluster 21. 124
Figure A.20 Stress inversion result for cluster 22. 124
Figure A.21 Stress inversion result for cluster 23. 125
Figure A.22 Stress inversion result for cluster 24. 125

Figure A.23 Stress inversion result for cluster 25. 126
Figure A.24 Stress inversion result for cluster 27. 126
Figure A.25 Stress inversion result for cluster 28. 127
Figure A.26 Stress inversion result for cluster 29. 127
Figure A.27 Stress inversion result for cluster 30. 128
Figure A.28 Stress inversion result for cluster 31. 128
Figure A.29 Stress inversion result for cluster 32. 129
Figure A.30 Stress inversion result for cluster 33. 129
Figure A.31 Stress inversion result for cluster 34. 130

Figure B.1 Summary plots of shear-wave splitting at station AHCB. . . . 133
Figure B.2 Summary plots of shear-wave splitting at station BMSB. . . . 134
Figure B.3 Summary plots of shear-wave splitting at station BTB. 135
Figure B.4 Summary plots of shear-wave splitting at station CBB. 136
Figure B.5 Summary plots of shear-wave splitting at station CLVB. . . . 137
Figure B.6 Summary plots of shear-wave splitting at station CPLB. . . . 138
Figure B.7 Summary plots of shear-wave splitting at station EDB. 139
Figure B.8 Summary plots of shear-wave splitting at station ENGB. . . . 140
Figure B.9 Summary plots of shear-wave splitting at station GNHB. . . . 141
Figure B.10 Summary plots of shear-wave splitting at station GOWB. . . . 142
Figure B.11 Summary plots of shear-wave splitting at station HNB. 143
Figure B.12 Summary plots of shear-wave splitting at station JRBC. . . . 144
Figure B.13 Summary plots of shear-wave splitting at station KHVB. . . . 145
Figure B.14 Summary plots of shear-wave splitting at station LZB. 146
Figure B.15 Summary plots of shear-wave splitting at station MGB. 147
Figure B.16 Summary plots of shear-wave splitting at station NLLB. . . . 148
Figure B.17 Summary plots of shear-wave splitting at station OZB. 149

Figure B.18 Summary plots of shear-wave splitting at station PFB. 150
Figure B.19 Summary plots of shear-wave splitting at station PGC. 151
Figure B.20 Summary plots of shear-wave splitting at station PHYB. . . . 152
Figure B.21 Summary plots of shear-wave splitting at station PIMB. . . . 153
Figure B.22 Summary plots of shear-wave splitting at station SHB. 154
Figure B.23 Summary plots of shear-wave splitting at station SHVB. . . . 155
Figure B.24 Summary plots of shear-wave splitting at station SILB. 156
Figure B.25 Summary plots of shear-wave splitting at station SNB. 157
Figure B.26 Summary plots of shear-wave splitting at station SOKB. . . . 158
Figure B.27 Summary plots of shear-wave splitting at station SSIB. 159
Figure B.28 Summary plots of shear-wave splitting at station THAB. . . . 160
Figure B.29 Summary plots of shear-wave splitting at station TOFB. . . . 161
Figure B.30 Summary plots of shear-wave splitting at station TSJB. 162
Figure B.31 Summary plots of shear-wave splitting at station TWGB. . . . 163
Figure B.32 Summary plots of shear-wave splitting at station TWKB. . . . 164
Figure B.33 Summary plots of shear-wave splitting at station VGZ. 165
Figure B.34 Summary plots of shear-wave splitting at station YOUB. . . . 166

ACKNOWLEDGEMENTS

Most of all, I would like to thank my supervisors John Cassidy and Stan Dosso, for all their guidance with my research and the writing of my thesis. Also to all my committee members, including Garry Rogers and Michel Lefebvre, for their helpful suggestions and for allowing me to pursue opportunities in teaching during my time at the University of Victoria. To my external examiner Joan Gomberg for her useful comments for corrections. It has been a pleasure working with people who are enthusiastic and motivate me to continue research in geophysics.

Thank you to the NSERC who provided grants to fund this research. The employees of Natural Resources Canada, especially Alison Bird, who maintain the CNSN catalogue and provided me with resources and support for this study. The facilities of the IRIS Data Management System, and specifically the IRIS Data Management Center, were used for access to some waveform and metadata required in this study. Thanks to Richard Baldwin, Taimi Mulder, Steve Taylor, Kent Lindquist and the staff at BRTT for their support with the Antelope software and data management.

I would like to thank Stephane Mazzotti for computing strain rates; Richard Arnold and John Townend for their help accessing and using the Bayesian stress inversion code; Natasha Ruppert for the altered code for FPFIT with Antelope; Felix Waldhauser for his advice for using `hypoDD`; Michael West and Celso Reyes for their waveform and cross-correlation packages; Martha Savage and her graduate students for the updates to the automated shear-wave splitting code; Richard Franklin for the cartoon representation of crustal stresses; and Kelin Wang and Vaughn Barrie who participated in helpful discussions.

To my fellow graduate students at the University of Victoria and Pacific Geoscience Centre, especially: Sabine Hippchen, Ikuko Wada, Karen Simon, Sheri Molnar, Camille Brillion and postdoc Lucinda Leonard.

To my New Zealand family for their endless support, especially Lorraine and Craig, Peter and Natalie, and Nic and Tai. Also, thanks to my new Canadian family, Marie Zirk and Dale Olsen, for their support and the delicious homemade dinners.

A very special thank you to my partner Clinton Zirk who is always supportive and helpful. He looked after me in the last 6 months, making me laugh, making me food and getting me out for some exercise. I could not have done this without him.

Thank you to my wonderful friends Jessica Mills, Erin Anderson and Monica Osuchowski, who still support me even though they are far away. And to all my friends at the University, swing dancing Victoria and in other areas of my life. And lastly an apology to anyone who I may have inadvertently forgotten, thank you.

DEDICATION

For my late grandfather, Norman (Buster) Balfour, you will always be an inspiration to keep going not matter what obstacles lie ahead.

Chapter 1

Introduction

1.1 Objectives

The Cascadia subduction zone in Southwest British Columbia experiences both megathrust earthquakes at the subduction interface as well as large events from faults in the overlying crust. These crustal events, with recorded magnitudes of up to 7.3, pose significant hazard to major population centres in the area. Previous studies have shown this is a complex region of deformation located above a bend in the subducting Juan de Fuca plate (Ristau *et al.*, 2007; Currie *et al.*, 2001; Ramachandran *et al.*, 2006).

The objective of this thesis is to gain a better understanding of the processes that result in earthquakes in the North America crust of the northern Cascadia Subduction Zone. This project is centred on answering three main questions that seek to address the objective:

1. Where do large earthquakes occur in the crust of the North American Plate of Northern Cascadia?

2. What forces influence faulting in the crust?

3. Can we monitor forces that influence faulting using seismic anisotropy?

By investigating seismicity patterns and the state of stress, we aim to gain a better understanding of the forces driving earthquake activity and the resulting seismic hazard. Several aspects of seismology are combined to accomplish this, including studying seismicity patterns, focal mechanism determination and stress inversions, and crustal anisotropy from shear-wave splitting.

1.1.1 Where do large crustal earthquakes occur?

To address the question of where earthquakes occur we investigate whether the earthquakes occur on faults that we can trace on the surface or if they occur on "hidden" structures with no surface trace? It appears that seismicity in British Columbia does not relate to surface expressions of faults (Mulder, 1995; Rogers, 1998), therefore it is necessary to use techniques to find structures which are hidden at depth. A component of this project searches for evidence of undiscovered active structures by using the double difference technique for earthquake relocation. This is a precise method for relocating earthquakes relative to one another using the differences in the travel times for closely spaced events. It reduces uncertainty in the relative locations by assuming the difference in travel times is related to the distance between the events. Catalogue phase picks are sufficient for double-difference; however, uncertainties can be further reduced by using highly accurate differential travel times obtained from

cross-correlating waveforms. This method can illuminate the extent of structures with high seismicity and helps identify regions and communities that might be impacted if earthquakes occur on these structures. We also investigate the influences of crustal velocity models on earthquake relocations and how incorrect models can cause artifacts which may lead to misinterpretation.

1.1.2 What forces influence faulting?

To identify what influences faulting we need to identify the regional stress and how it varies spatially. This component of the project involves considering focal mechanisms and moment tensor solutions, which characterize the source mechanism of earthquakes. These mechanisms describe the strike and dip of the nodal planes (one of which is the fault plane) and the motion that resulted in the earthquake. Then by performing stress inversions on source mechanisms we can examine the state of stress in the crust and how it relates to faulting. A Bayesian inversion method is used to determine the three principal stress directions (maximum, intermediate and minimum compressive stress directions) and the stress ratio (Arnold and Townend, 2007). We compare stress and strain orientations to determine what forces influence faulting in the crust. Spatial variations in principal stress orientations can provide clues as to why seismicity patterns and faulting styles vary. Individual source mechanisms from earthquakes that occur on "hidden" structures can help determine what type of faulting occurs, which can be used for understanding source regions and modelling potential ground shaking.

1.1.3 Can we monitor forces that influence faulting using seismic anisotropy?

To use seismic anisotropy as a stress indicator and eventually as a monitoring tool requires identifying which stations observe anisotropy that is influenced by stress and which stations observe anisotropy influenced by structure. Seismic anisotropy can often be used as a proxy for stress as the fast direction can be related to the maximum horizontal compressive stress (Gerst and Savage, 2004; Crampin, 1994). However, anisotropy can be complicated by crustal structure, as sheared and foliated rocks due to faulting and metamorphism have anisotropic fabrics. Stations that show stress-related anisotropy tell us about the orientation of the maximum compressive stress and can be used to monitor temporal changes in the stress over extended time periods. Stations with structure-related anisotropy are used to investigate how crustal faults effect shear-wave splitting results. To this end we examine crustal anisotropy from shear-wave splitting measurements at 35 seismic stations in the vicinity of Vancouver Island. Then we compare the shear-wave splitting results to the maximum horizontal compressive stress direction to identify which stations are influence by stress and which by structure. Finally, we investigate temporal variations at stations that have a long record of observations and stress-related anisotropy.

1.2 Tectonic Setting

Southwest British Columbia is located in the northern Cascadia subduction zone (Figure 1.1). The subduction zone is characterized by the Juan de Fuca Plate subducting beneath the North American Plate and extends along the west coast of North

America from northern California to the northern end of Vancouver Island, British Columbia. The Queen Charlotte Fault and the San Andreas Fault to the north and south of the subduction zone, respectively, are two large right-lateral transform faults that mark the boundary between the Pacific and North American plates.

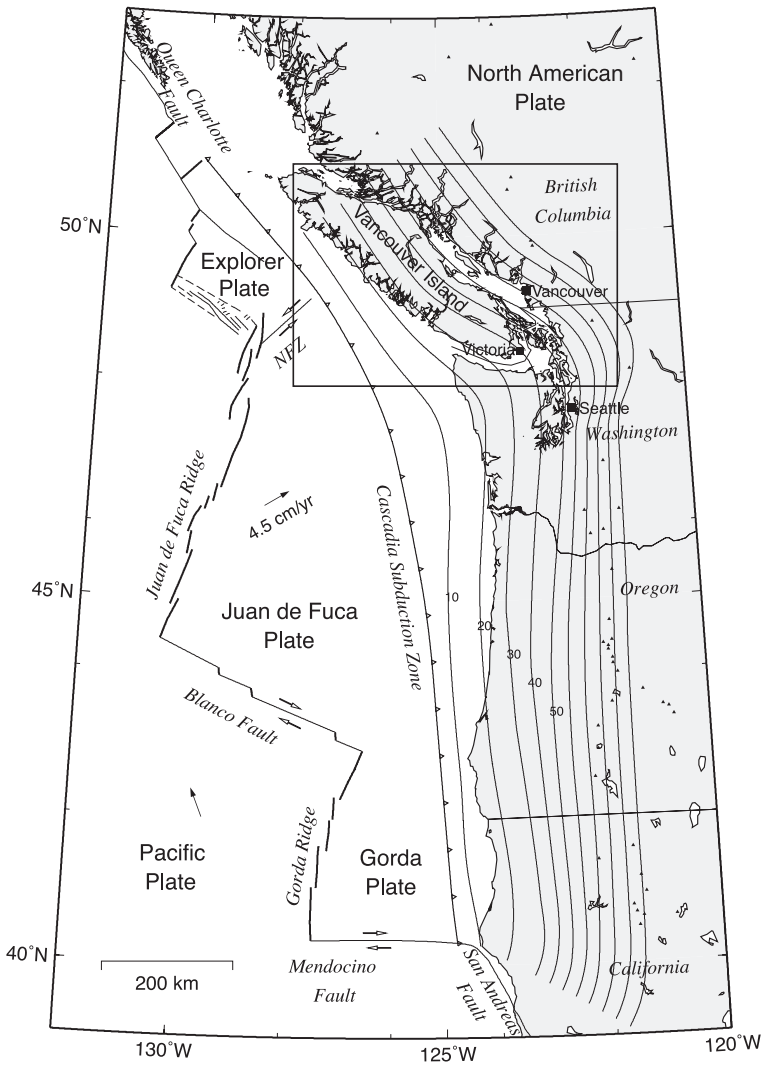

Figure 1.1: Cascadia subduction zone. Contours show depth to the top of the subducting slab in kilometres (McCrory et al., 2004). Area outlined by the box is the region discussed in this study.

The Cascadia subduction zone is part of a complex system where the Juan de Fuca plate is diverging from the Pacific plate with a half spreading rate of 2.9–3.1 cm/yr

(Atwater, 1970; Riddihough, 1977) and subducting at rate of 4.5 cm/yr relative to the North American Plate (Riddihough, 1984). The Juan de Fuca plate (like the Rivera and Cocos plates) is a remanent of the ancient Farallon plate. This system is further complicated by the break up of the Juan de Fuca plate into the Explorer plate to the north and the Gorda plate to the south; however, this study is mostly concerned with the interaction between the Juan de Fuca and North American plates. The subducting portion of the Juan de Fuca plate is relatively young (5–10 Ma) (Atwater, 1970). Young subducting slabs are relatively hot and buoyant compared to subduction zones where the oceanic crust is older (Wang and Jiangheng, 1999). This results in the angle of subduction to be shallow reaching $\sim 17^{\circ}$ beneath Vancouver Island (Hyndman *et al.*, 1990) and also results in relatively shallow earthquakes in the subducting plate (maximum depth 80–100 km).

The crust in southwest British Columbia lies above a bend in subducting Juan de Fuca plate, where the strike of the subduction margin changes from north-south to northwest-southeast. There are several plate driving forces that affect the deformation of the crust: the plate motion from subduction to the west (Atwater, 1970) and the northward motion of the west coast of the United States (DeMets *et al.*, 1990; McCaffrey *et al.*, 2000). Southwest British Columbia, and in particular Vancouver Island, is made up of metamorphic and igneous terranes which are remanents of island arcs that were accreted to the edge of the North American Plate (Monger *et al.*, 1972; Monger *et al.*, 1982). The boundaries between these terranes are marked by large faults, such as the San Juan Fault.

There are three types of earthquakes in this region which are the result of the plate motions. The first are interplate (or megathrust) earthquakes that occur between the Juan de Fuca and North American plates. In Cascadia, these occur 200–1000 yrs

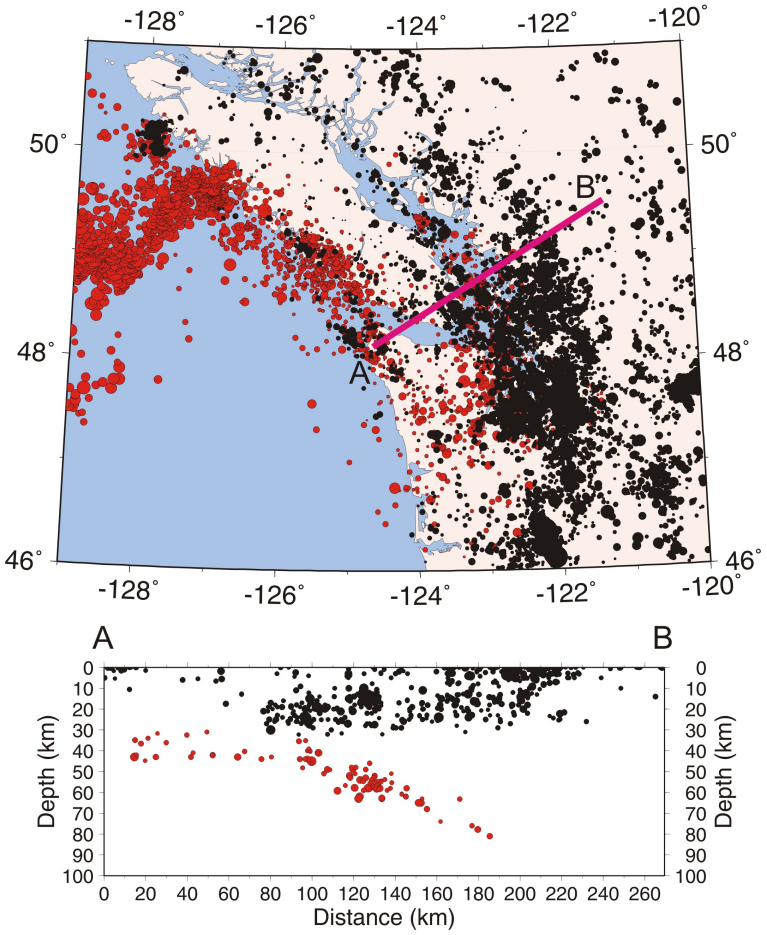

Figure 1.2: Map (top) and cross-section (bottom) of seismicity in northern Cascadia. Black circles are earthquakes that occur within the North American plate and red circles are earthquakes within the Juan de Fuca plate. Image was created by Taimi Mulder and Robert Kung (Pacific Geoscience Centre, Geological Survey of Canada)

apart (Goldfinger *et al.*, 2008) and result in approximately magnitude 9 events. A megathrust earthquake is the result of a substantial portion of the interface between the two plates being locked. As a result, strain accumulates over hundreds of years until eventually the stress overcomes the frictional strength of the fault and causes a large rupture. The rupture will be large enough to displace the seafloor and generate a tsunami. The most recent megathrust event occurred on January 26th, 1700 (Satake

et al., 1996). The second type of earthquake are deep intraplate events (Figure 1.2, red). These occur within the subducting Juan de Fuca plate and are concentrated along the west coast of Vancouver Island (25–30 km depth) and beneath Puget Sound (50–60 km depth). They have magnitudes up to ∼7 and occur frequently in historical records (e.g., 1949, 1965 and 2001) (Rogers, 1998). The third type of earthquake are crustal earthquakes which occur in the North American crust (Figure 1.2, black). These are the focus of this study as they are shallow and can cause strong ground shaking. Historically, the largest of these events to occur in British Columbia and Washington range from magnitude 6.5–7.3 and have occurred most recently in 1872, 1918 and 1946 (Rogers, 1998). Characteristics of these events and how they pertain to this study are discussed in more detail below.

1.3 Motivation

The crust in southwest British Columbia is known to experience large earthquakes over varying time intervals. The largest known crustal earthquake occurred in 1946 near Courtney on Vancouver Island, M_S 7.3. It caused chimneys and building fronts to collapse, structural damage, slumping and landslides (Rogers and Hasegawa, 1978). There was only one fatality from drowning when a boat capsized due to a wave triggered by the event (Hodgson, 1946). If the same event were to occur today, taking into consideration the increased population and infrastructure, we have to ask: would the outcome be similar?

At first glance, earthquakes in the crust seem to occur randomly and do not show much correlation to surface faults, nor are lineations apparent in the seismicity patterns. However, an in-depth study of seismicity in the Georgia Strait showed lineations and

identified an active structure (Cassidy *et al.*, 2000). One of the aims for this project is to find more structures that are potentially active and could represent a hazard to the population centres in southwest British Columbia.

To determine the cause of faulting in the crust, we must understand the present day regional stress field. A number of indicators can be used to determine various components of the crustal stress tensor: hydraulic fracturing, borehole breakouts (Zoback and Zoback, 2002), fault slip data, the orientation of igneous dykes and inversion of earthquake focal mechanisms. The regional stresses are important to understand the fault mechanics as well as what causes faulting and triggering of aftershocks. Stress and faulting are related through Anderson's theory of faulting (Anderson, 1951) and Byerlee's Law (Byerlee, 1978). Stress and faulting relations are important for several reasons: determining the dominant stress regime and what tectonic forces influence it, determining the type of faulting, and understanding the general strength of faults.

The World Stress Map project (Zoback, 1992) is the repository for all forms of stress data from around the world, providing information on the quantity and quality of stress measurements. Stress orientations from the inversion of a group of focal mechanisms is considered high quality data (A or B quality), while single focal mechanisms (C–E) or composite focal mechanisms are poor quality (D–E). Investigating southwest British Columbia using the World Stress Map shows no formal stress inversions and only a few single focal mechanisms. There have been studies of focal mechanisms and stress in the crust but they have mostly considered larger (M>4.5) events (Rogers, 1979; Ristau *et al.*, 2007) of which there are too few over the large region to carry out a stress inversion. Mulder (1995) determined focal mechanisms for earthquakes down to magnitude 3 from 1975–1991 and inverted them for stress. The stress

results from these studies suggest a north-south maximum compressive stress direction with a mixture of faulting styles, but only contributed individual focal mechanisms to the World Stress Map. In the absence of data from drilling, we must rely of inverting focal mechanisms to determine the stress orientation and regime. A more thorough investigation consisting of stress inversions over smaller areas can investigate spatial variations in crustal stress as might be expected in such a complex region, as well as ensuring the assumption of homogeneous stress is satisfied.

Recent studies on crustal anisotropy have focused on using anisotropy as a monitoring tool for temporal changes in stress (Gerst and Savage, 2004; Crampin *et al.*, 2008; Savage *et al.*, 2010). There have been observations of changes in shear-wave splitting parameters associated with dyke intrusions near active volcanoes and with moderate to large earthquakes. Previous studies of anisotropy from Cassidy and Bostock (1996) and Currie *et al.* (2004) suggest that crustal anisotropy in the northern Cascadia subduction zone is associated with stress; however, there was not enough data available to investigate temporal variations and the network was not dense enough to identify small scale spatial variations. With the introduction of more 3-component broadband seismometers to the Canadian National Seismic Network sufficient data are now available to investigate possible temporal variations and determine the source of spatial variations.

1.4 Outline of Thesis

This thesis is based on three papers written to address each of the questions discussed in section 1.1. Details in the methodologies used are presented in each paper.

1. The first paper investigates where large earthquakes might occur by attempting to identify active structures in the crust by precisely relocating earthquakes relative to each other. The paper focuses on two specific regions that are close to large communities and important infrastructure in British Columbia.

2. The second paper seeks to understand the regional stress field in southwest British Columbia. To do so, the focal mechanism catalogue is updated with the addition of ∼600 new focal mechanisms. A Bayesian method is applied to the inversion problem which allowed focal mechanism uncertainties to be included. The stress results are compared with strain calculations, performed by Stephane Mazzotti specifically for this study, to help interpret spatial variations in the stress.

3. The third paper seeks to better constrain the source of anisotropy in the crust and determine whether it could be used to monitor temporal stress variations. Long records of observations are required to determine "normal" results and what represents meaningful variations related to changes in stress. We determine the source of anisotropy and the average shear-wave splitting parameters at ∼30 stations and take a closer look at the two stations with the longest observation history in an attempt to identify temporal variations.

Each of the following three chapters is written as a stand-alone paper with its own introduction, data, methods, results and conclusion sections. The final chapter summarises the results of each paper and relates them to the overall objective of this thesis.

Chapter 2

Identifying Active Structures from Earthquake Relocations

This paper applies double-difference earthquake relocation techniques to investigate sources of seismicity in southwest British Columbia, Canada, and the San Juan Islands, Washington. The study area is a complex region of deformation and has the potential for large earthquakes in the North America crust. Double-difference earthquake relocation techniques are applied to identify "hidden" active structures that may pose a hazard to nearby population and infrastructure. We present evidence for previously unrecognized active structures using precise relative earthquake relocations obtained using both catalogue and waveform cross-correlation data. Results have significantly reduced errors over routine catalogue locations and show lineations in areas of clustered seismicity. In southwest British Columbia these lineations or streaks appear to be hidden structures that do not disrupt near-surface sediments; however, in the San Juan Islands the identified lineation could be related to recently mapped surface expressions of faults identified from seismic reflection and multibeam

bathymetry surveys. We use a variety of velocity models for the relocations and find that inappropriate models lead to artifacts at layer boundaries and increased vertical errors.

2.1 Introduction

Southwest British Columbia and northern Washington are located in northern Cascadia where the Juan de Fuca plate is subducting beneath the North American plate. Previous studies have shown this to be a complex region of deformation located above a bend in the subducting plate (Clowes *et al.*, 1987; Ramachandran *et al.*, 2004; Ristau *et al.*, 2007) (Figure 2.1). This is also a region of complex crustal structure as the crust is composed of terranes of accreted island arcs (Monger *et al.*, 1982). There are also many mapped surface faults, some of which mark the boundaries between terranes (Figure 2.2).

The Cascadia subduction zone in southwest British Columbia and Washington experiences three types of earthquakes: megathrust earthquakes at the subduction interface, deep earthquakes in the subducting slab and shallow earthquakes from faults in the overlying crust. These shallow crustal earthquakes, with recorded magnitudes of up to 7.3, pose significant hazard to major population centres in the area such as Vancouver, Victoria and Seattle. The largest known crustal earthquake (M_S 7.3) occurred in 1946 near Courtney on Vancouver Island, and caused chimneys and building fronts to collapse, structural damage, slumping and landslides (Rogers and Hasegawa, 1978).

This study seeks to identify and map unknown active structures that might have

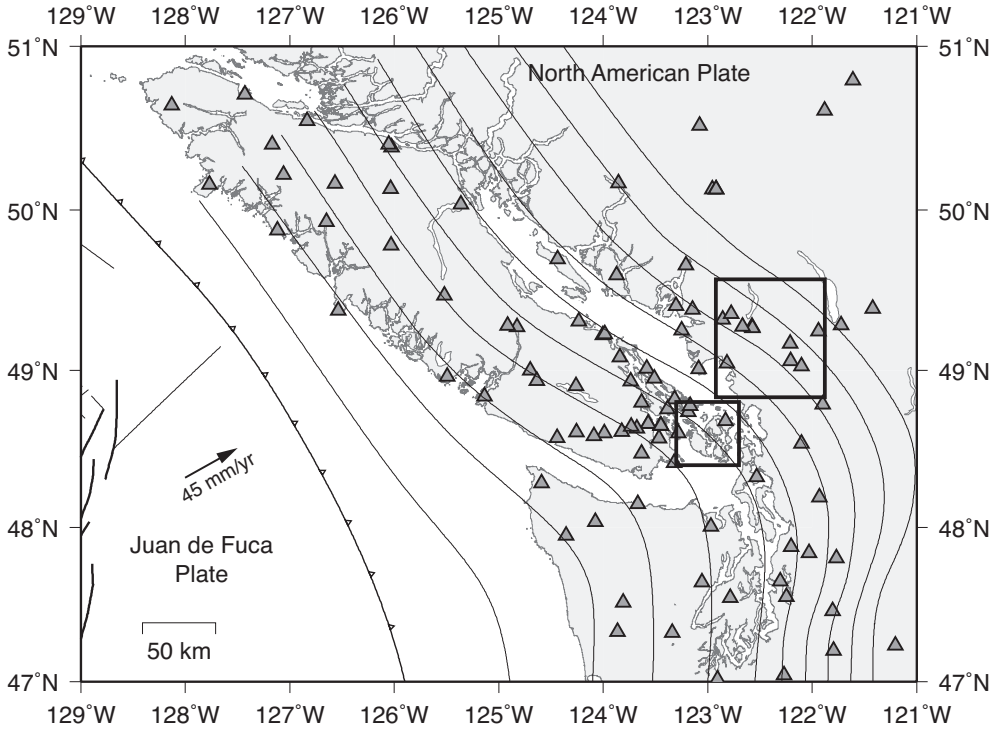

Figure 2.1: Southwest British Columbia and northwest Washington State. The Fraser River Valley (upper) and San Juan Islands (lower) study regions are outlined by boxes. Stations (triangles) include stations from the Canadian National Seismic Network (CNSN), POLARIS and the Pacific Northwest Seismic Network (PNSN). The approximate location of the Cascadia subduction zone plate boundary and depth contours of the Juan de Fuca plate (McCrory, 2004) are shown.

the potential to cause large crustal earthquakes near urban centres. We chose two regions to investigate in detail (outlined in Figures 2.1 and 2.2). The first is the Fraser Valley in southwest British Columbia (box 1, Figure 2.2), which was chosen because of the potential risk to infrastructure, such as dams, and its close proximity to greater Vancouver (∼20 km). The second is the San Juan Islands (box 2, Figure 2.2) because of its high seismicity and proximity to Vancouver (80 km) and Victoria (30 km).

The vast majority of the seismicity in southwest British Columbia does not relate to surface fault expressions (Figure 2.2); hence, it is necessary to use methods that

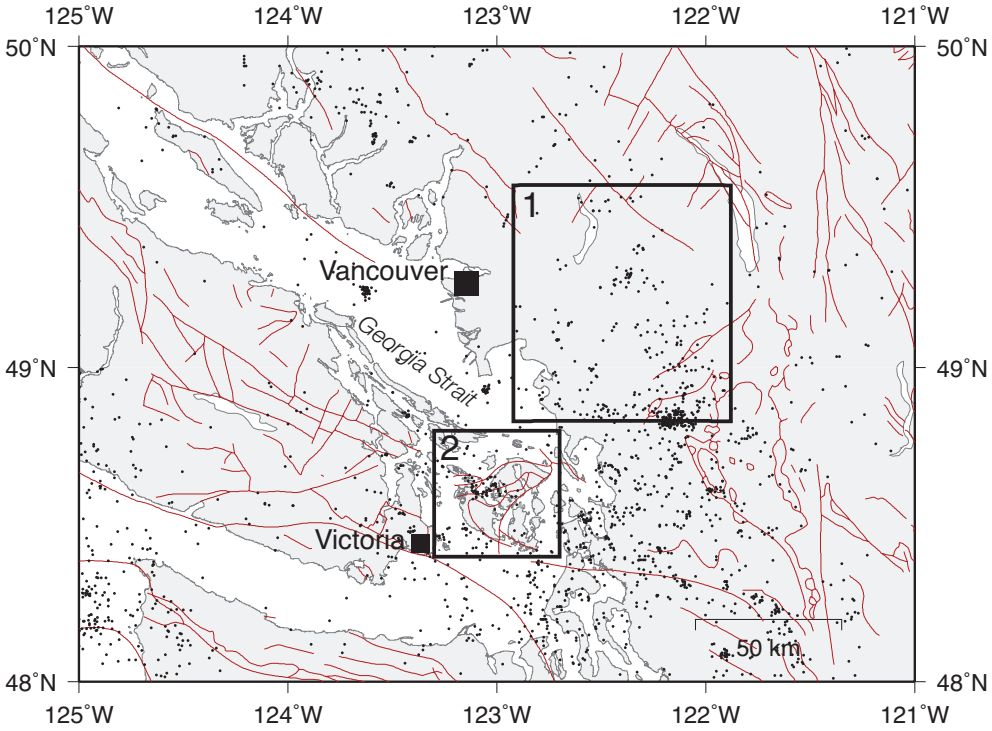

Figure 2.2: CNSN catalogue seismicity from 1970–2011, M>1.5 (dots) and mapped faults (red lines) (Journeay, 1995) in southwest British Columbia and northwest Washington state.

identify "hidden" structures. We use the double difference technique for earthquake relocation to search for evidence of unmapped active structures at depth. This precise method for relocating earthquakes relative to one another uses differences in the travel times for closely spaced events. It illuminates the extent of structures with high seismicity, and relates this to the area of possible rupture during an earthquake. This will potentially help identify regions and communities that may be affected by earthquakes on these structures.

The double-difference technique has been used in this region by Cassidy *et al.* (2000) to investigate a sequence of events in the Georgia Strait related to a magnitude 4.6 mainshock. They were able to identify a lineation from the aftershock sequence and relate it to the source mechanism of the main event to determine the fault on which

the earthquake sequence occured. In a similar manner, we seek to determine new active structures from areas of "background" seismicity.

2.2 Double-Difference Relocation

The method used here for relocating earthquake hypocentres is a double-difference algorithm known as `hypoDD` (Waldhauser and Ellsworth, 2000) which solves for event hypocentres and origin times using differential travel-time data from catalogue phase picks and/or waveform cross-correlations. It does so by minimizing the residuals between the observed and theoretical travel-times (double-differences) for pairs of earthquakes by adjusting the vector difference between the hypocentres. The relocated hypocentres are determined by solving the double-difference equation for all hypocentral pairs at all stations. A benefit of this method is that it considers the difference between closely space events and therefore reduces the error from unmodelled velocity variations between the station and the event pair.

Relocating events with `hypoDD` results in precise relative locations and reduces error between events. This may illuminate faults if events are located on the same structure. Results from both synthetic- and real-data studies show that relative errors are reduced by a factor of $\sim$2 using catalogue arrival times alone, and reduced by a further factor of $\sim$5–10 if cross-correlation data are also used (Waldhauser and Ellsworth, 2000; Hauksson and Shearer, 2005).

There are two options to solve the inversion problem depending on the size on the dataset. The preferred option is to use weighted least squares inversion by applying singular value decomposition (SVD) as this approach quantifies errors in the solution.

However, SVD is only applicable to small sets of data (<100 events) because it is computationally intensive. The other option, applicable to larger data sets, is the conjugate gradients method (LSQR, Paige and Saunders, (1982b; 1982a)), which does not resolve the errors in the solution. In this case, Waldhauser and Ellsworth (2000) suggest performing a separate analysis on a subset of the data using the SVD or statistical resampling techniques to estimate the uncertainties.

The LSQR approach is used to relocate earthquakes in this study due to the large datasets, therefore we must evaluate errors using another method. For both regions in this study we relocated a subset of events using the SVD mode of `hypoDD` for reliable error estimates. Throughout the results discussion we report all errors in location as the standard error (2σ).

2.2.1 Catalogue Arrival Times

To apply double-difference relocation to catalogue arrival times requires pre-processing of data to calculate the differential travel-times for event pairs. We use the program `ph2dt` (Waldhauser, 2001) to find event pairs by determining a specified number of closely-spaced neighbours within a set region that are linked with common stations and phase arrival data. For the data in this study, we use a maximum event-to-station distance of 500 km, maximum separation between event pairs of 10 km, and a minimum number of 8 links per event pair. We allow for a different maximum number of neighbours depending on the size of the region and the density of seismicity (maximum 15 neighbours for large regions and 10 for small regions).

Further data selection is carried out within `hypoDD`, which divides events into clusters of related events. This process often reduces the number of events to be relocated

as some events may not be strongly related to any other events. Clusters of well-connected events are defined when a group of events is not linked or weakly linked with any other group. The double-difference algorithm is then applied separately to each cluster. When using only catalogue data, two sets of five iterations were performed on each cluster. The first set weights the data based on the a priori weighting from the catalogue, and weights P-wave arrivals higher than S-waves. The a priori weight is defined by the uncertainty in the pick as provided by the analyst (if that information is unavailable we assume a pick uncertainty of 0.1 s). The pick uncertainty is then translated to a weight; e.g., an uncertainty of 0–0.1 s has a weight of 1. The second iteration down-weights event pairs that have large separations and differential times with high residuals. The parameters for this second iteration vary depending on the density of the data. If the LSQR method is used then we also define a damping factor to prevent the solution from becoming unstable. Sometimes events are discarded from the relocation during the process due to either being located above the surface or not being linked with any other events.

2.2.2 Waveform Cross Correlation

Waveform cross-correlation is used on the San Juan Island events to obtain very accurate arrival times and therefore differential arrival times for use in `hypoDD`. Waveforms from two closely spaced events are cross-correlated by shifting one waveform past the other in small time increments. The correlation function is the normalized correlation coefficient at each time shift and describes how well the waveforms are correlated: 1 is perfect correlation, 0 is no correlation and -1 is perfect anti-correlation (waveforms are identical with a polarity reversal). The lag or time shift between two waveforms at maximum correlation indicates the difference in their travel-times.

When processing events we save information for pairs of waveforms where the maximum correlation coefficient $\geq$0.7 and the lag is $<$0.2 s. Figure 2.3 shows waveforms for P and S arrivals from events located near the San Juan Islands and recorded at station PGC that meet these criteria. Cross-correlation information is incorporated into `hypoDD` by using the precise differential arrival times weighted according to the cross-correlation coefficient (squared coherency to include negative correlations).

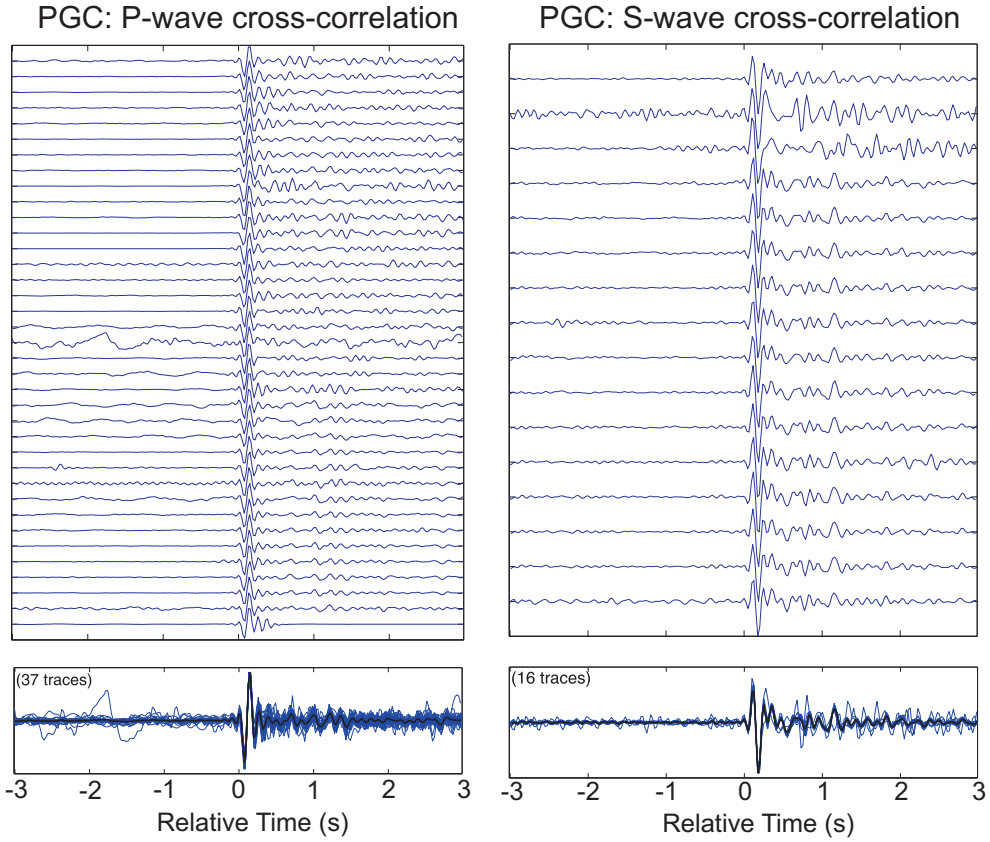

Figure 2.3: Example of cross-correlated waveforms recorded at station PGC. Each trace represents a P-wave (left) or S-wave (right) arrival for a different earthquake in the San Juan Island region. Stacked arrivals that have been corrected for lag are shown for each phase (black trace, bottom). Note only highly correlated waveforms (correlation coefficient $>$ 0.7) are shown and used for double-difference relocation.

Cross-correlation information is limited because waveforms are not available for every phase at each station-event pair; therefore, we use a combination of catalogue and cross-correlation data. When using a combination of data we performed four sets of

five iterations. The first two sets are weighted so that the catalogue information is strongly weighted: 1 for catalogue P-wave, 0.5 for catalogue S-wave and 0.01 for cross-correlated phases. The second two are weighted so the cross-correlation information is strongly weighted: 1 for cross-correlated P-waves, 0.5 for cross-correlated S-waves, 0.01 for catalogue P-waves, and 0.005 for catalogue S-waves. This allows the large scale features to be resolved by the catalogue data and small scale features to be resolved by the cross-correlated data (Waldhauser and Ellsworth, 2000; Waldhauser, 2001).

2.3 Data

As discussed earlier, two regions are chosen to investigate based on their relatively high rates of seismicity and proximity to urban centres: the Fraser Valley and the San Juan Islands (Figures 2.1 and 2.2). The Fraser Valley and San Juan Islands datasets consist of 611 and 300 events respectively. In both datasets the earthquakes were recorded from 1992–2006 and range in magnitude from 0–3. This time period is used because an upgrade in the network in southwest British Columbia was made in 1992, providing real-time continuous data from mostly 3-component broadband seismometers.

2.3.1 Networks

For maximum information from earthquakes in southwest British Columbia we consider seismic stations in Canada and the United States. In Canada, we use permanent stations from the Canadian National Seismic Network (CNSN) and arrays of

temporary stations on Vancouver Island from the Portable Observatories for Lithospheric Analysis and Research Investigating Seismicity (POLARIS) consortium. In the United States, we use stations from the Pacific Northwest Seismic Network (PNSN), operated by the University of Washington.

2.3.2 Standard Locations and Velocity Models

All initial earthquake locations come from the CNSN catalogue. Phase arrival information comes from both CNSN and University of Washington catalogues. Over the years various single-event location algorithms have been used for these events. The two main algorithms used are `LocEq` (Geological Survey of Canada in-house software) and `GENLOC`. `GENLOC` is the more modern method used and is described by Pavlis *et al.* (2004). In the San Juan Islands study region waveforms were necessary to pick S-wave arrivals from PNSN stations because only P-wave arrival information is sent to CNSN. The San Juan Island region required this information (more so than the Fraser River Valley region) because it relies on PNSN stations for >180° of azimuthal coverage. The S-wave picks were then incorporated into the database and then all events were located with `GENLOC`.

In general, the Vel03 velocity model, shown in Figure 2.4 and described by Rogers (1983), is used for catalogue locations for earthquakes in southwest British Columbia. However, the choice of velocity model is important for the earthquake locations to reduce artifacts due to sharp velocity contrasts at layer boundaries. Michelini and Lomax (2004) investigates the effect of choosing an incorrect velocity model when relocating events with `hypoDD`. Their study uses synthetic data from a known velocity model and earthquake locations and varies the model and station geometry when

relocating the events. In comparing the relocations with the known locations, they found that some velocity models distorted the configuration of the events. They also observed that an incorrect velocity model in conjunction with certain source-receiver geometries can result in artifacts that appear as lineations. We investigate the effect of the velocity model on earthquake locations by considering alternative models specific to each region.

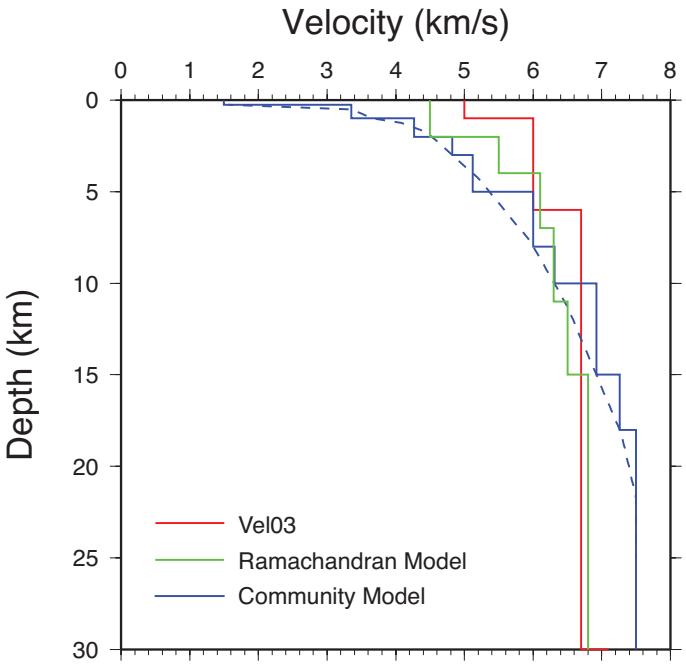

Figure 2.4: P-wave velocity models used for earthquake relocations in southwest British Columbia and the San Juan Islands. The original model for southwest British Columbia is in red (aka Vel03). The Ramachandran model (Ramachandran, 2005) shown in green is used for the San Juan Islands. The layered Community model used for the streak of seismicity in the Fraser Valley shown in blue is based on a gradational model by Molnar (2011) (smooth dashed blue line).

2.4 Results

2.4.1 Fraser Valley, British Columbia

The Fraser Valley region is just east of Vancouver and straddles the Canada/US border (Figure 2.2, box 1). Catalogue locations appear scattered with a few small clusters (Figure 2.5). There are some surface expressions of faults, but little is known about when they last ruptured in southwest British Columbia. Studies of faults in northern Washington have involved LiDAR to identify Holocene fault scarps and trenching to determine the ages of fault ruptures (Barnett, 2007). Older, unmapped faults may exist, but could be covered by the sediments of the Fraser River delta.

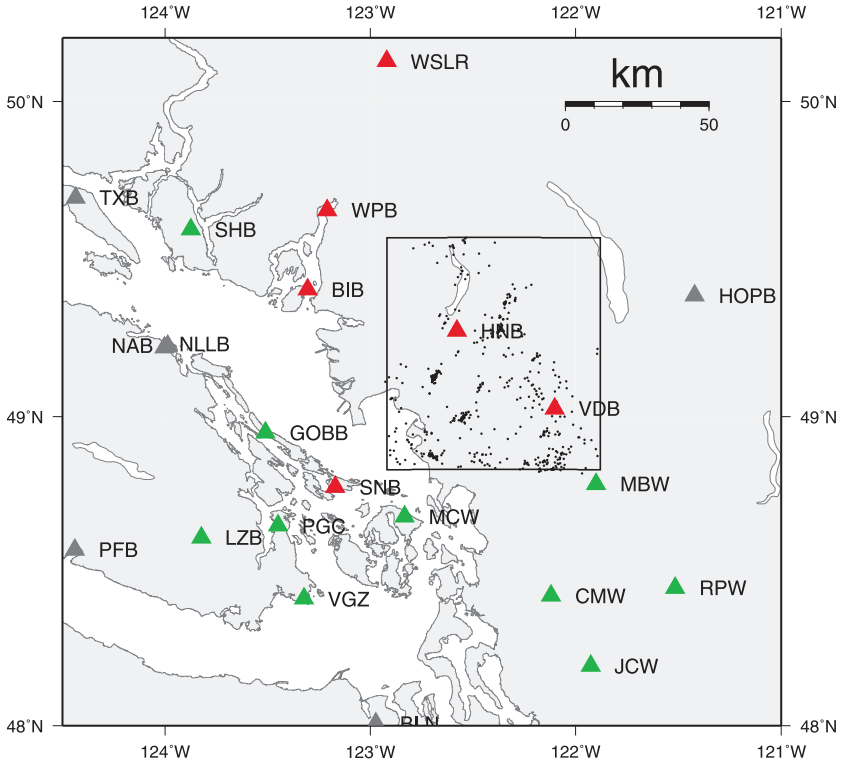

Figure 2.5: Seismicity for the Fraser River Valley in southwest British Columbia, 1992–2006. Hypocentres (black dots) determined using `hypoDD`. Stations are coloured according to their contribution: red indicates a large number of phases used (>100), green is moderate (20–100) and grey is small (<20).

Initially ∼600 earthquakes over a 1° by 1° square (large box, Figure 2.5) were relocated with `hypoDD` using the LSQR method. Events were small with M_L <3. Detailed analysis was carried out on a subset of events using the SVD method to estimate uncertainties (small box, Figure 2.6). Catalogue locations were used as starting estimates and the velocity model was the standard 1-D model Vel03 (Figure 2.4). A total of 67,275 differential arrival times were used from both P- and S-waves observed at ∼70 stations. We down-weight event pairs with separation distances >5 km and with residuals of more than 5 times the standard deviation. A damping factor of 80 is applied to the solution.

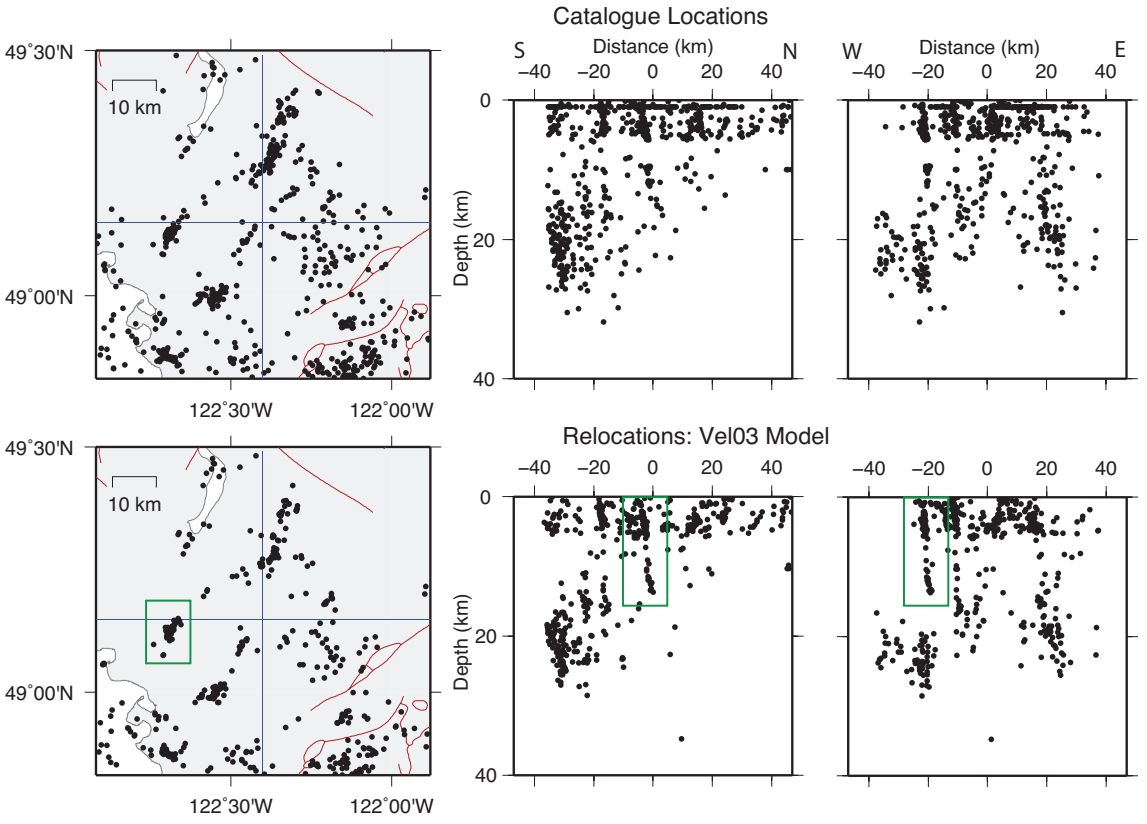

Figure 2.6: Double-difference relocations for the Fraser Valley region shown in Figure 2.5. The upper row shows standard catalogue locations and the bottom row shows events relocated using `hypoDD`. Uncertainties are not shown because the LSQR method was used. Blue lines indicate the profiles of the cross-sections, where zero is the point that the profiles cross. Green box is the subset selected for more detailed analysis. The red lines indicate mapped surface faults.

The relocated hypocentres show improved clustering, with several of the clusters becoming more focused (Figure 2.6). Error estimates are not shown for these results as they are not meaningful when `hypoDD` is used in LSQR mode. The apparent concentration of seismicity in the top 6 km could be due to a jump in the velocity model from 6 kms^{-1} to 6.7 kms^{-1}. The depth extent of the seismicity appears to shallow to the north and there is a large cluster of seismicity ∼20 km deep ∼40 km south and ∼ 20 km east (see cross-sections Figure 2.6). We can identify at least two lineations that dip to the northeast and extend from the surface to ∼15 km depth. The lineations do not appear to extend along strike and could be described as streaks of seismicity.

Figure 2.7 shows the subset of 83 events belonging to the seismicity streak outlined by the green box in Figure 2.6. These events are relocated using `hypoDD` with SVD using catalogue differential arrival times. The events are well observed with 3673 differential P-wave times and 4068 differential S-wave times. The subset of events was relocated with both the standard Vel03 velocity model and a more detailed velocity model from Molnar (2011). This model, which we refer to as the Community model, includes low-velocity near-surface layers related to the Fraser River delta sediments. The initial locations show two clusters that appear to be offset from each other in depth. The relocation processing also identifies two distinct clusters and relocates events within each cluster separately. Initial weighting parameters used in the first set of iterations are the same as discussed in section 2.2; however, in the second set we down-weight events separated by >8 km and arrival data with residuals >5 times the standard deviation. We compare the relocation results from using the two different velocity models (Figure 2.7). Our goal was to determine if the two clusters of seismicity are separated or if the gap between clusters is an artifact of the velocity model. Comparing results from relocations with the two velocity models in Figure 2.7

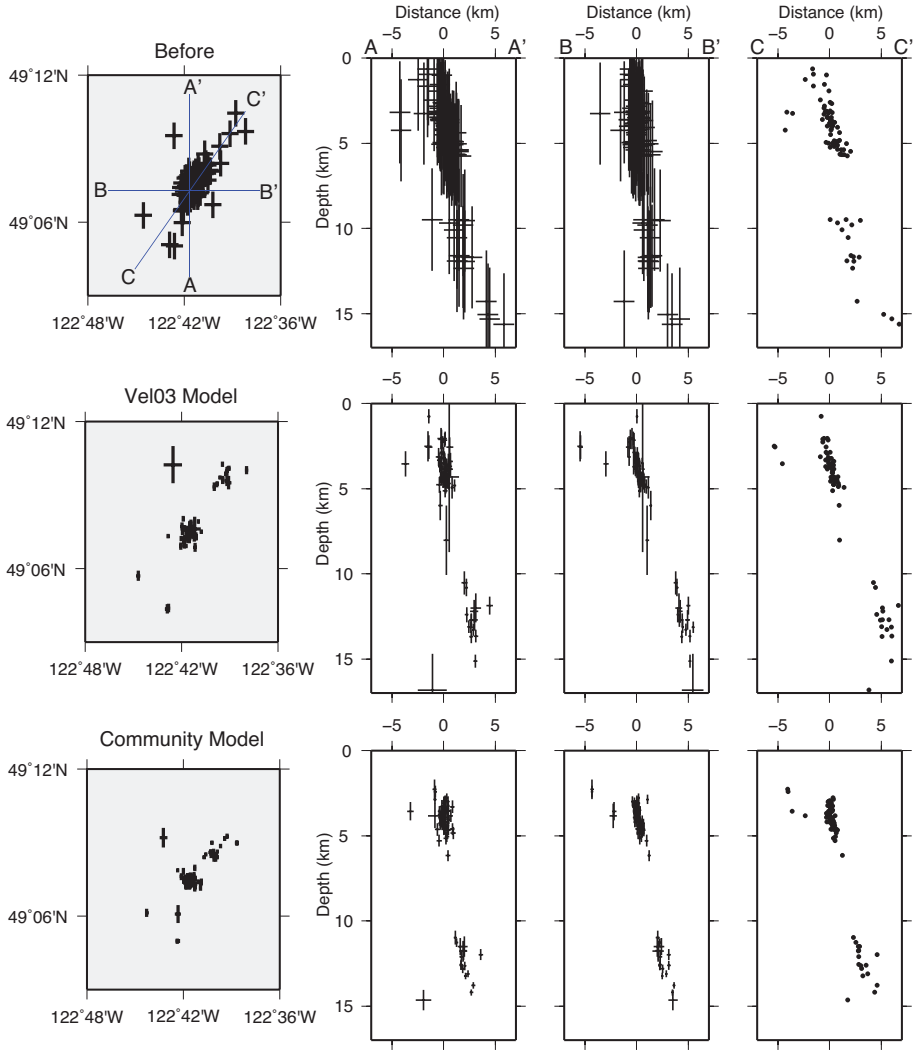

Figure 2.7: Double-difference relocations of a cluster of 84 events (green box, Figure 2.6). Locations and estimated uncertainties of earthquakes computed using a standard catalogue routine (upper) and those computed using `hypoDD` with the Vel03 (middle) and Community (lower) velocity models. The origin of the cross-section axes is the point where the profiles intersect. Precise relocation resolves two clusters on a 45°NE dipping structure.

(second and third rows) the two clusters remain separated; therefore, either there is a gap in seismicity along a single structure or the seismicity occurs clustered on separate structures. Further, Figure 2.7 shows that using a more representative velocity model significantly reduced location error particularly for events with large vertical errors. We also tested the dependence of the relocations on the starting model by giving each

event the same starting location (approximately the centre of the streak). We found that the dimensions of the streak were not dependent on the starting model, however the size of the gap between the two clusters was reduced from ∼5 km to ∼2 km with different initial locations. This suggests care is needed when interpreting small gaps in seismicity and that the dependence on the starting model is a source of error not included in the standard uncertainty estimates.

This small dataset can be used to evaluate errors in relocating events because SVD was applied. Figure 2.7 shows a general estimate of the error in the catalogue locations of ∼1 km in the horizontal and ∼2 km in the vertical. The relative mean error after relocating with catalogue data and using the Vel03 velocity model are ∼200 m (horizontal) and 540 m (vertical). Using the Community model the errors are reduced to ∼180 m (horizontal) and 340 m (vertical). These results suggest that using a more accurate velocity model which accounts for the low velocity surface layers improves the vertical location accuracy by a factor of 1.6.

2.4.2 San Juan Islands, Washington

The San Juan Islands have been an area of persistent crustal seismicity throughout the duration of earthquake monitoring in British Columbia. The largest magnitude event in the catalogue is M ∼3.0; however, magnitude 5.5–6 events occurred at unknown depths in 1920 and 1909 (pers. comm. Garry Rogers, 2008; Lamontagne *et al.*, (2008)). We relocated ∼300 earthquakes which occurred from 1992–2008 over a 20 by 20 km area. Figure 2.8 shows the location of the San Juan Islands and the combination of CNSN and PNSN stations used for earthquake relocations. These provide a reasonable azimuthal coverage of the seismicity; however, not all stations were installed

and operating during the entire study period so station coverage and event-station pairs are variable.

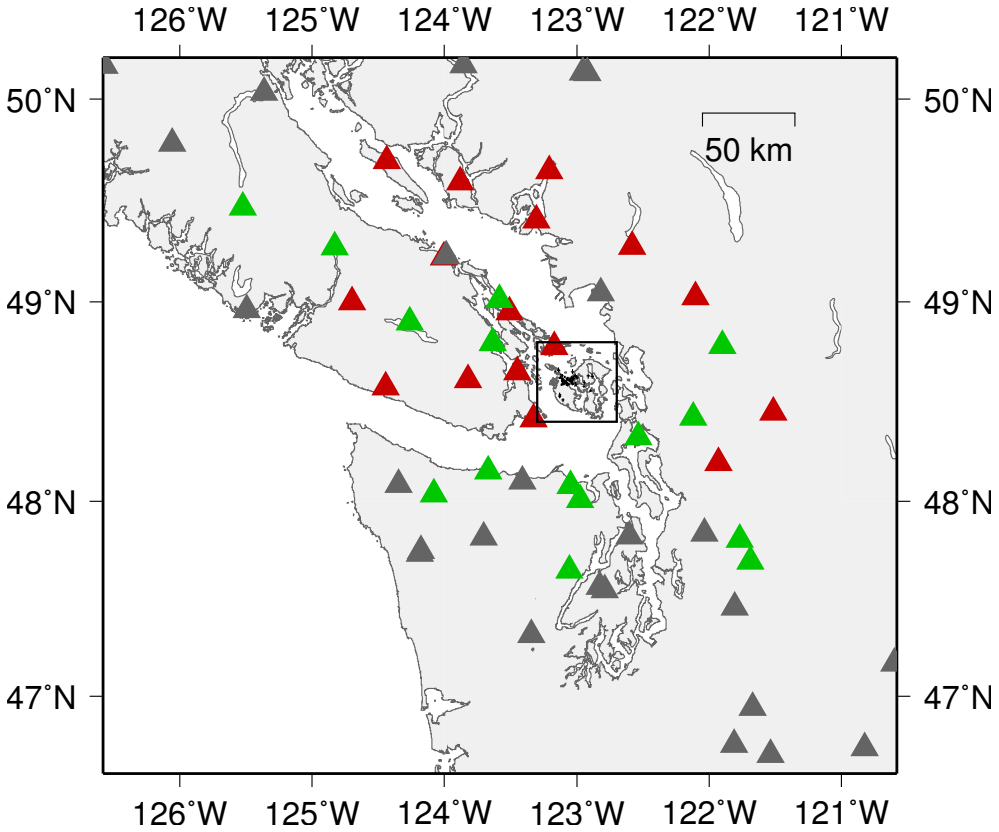

Figure 2.8: Stations used for double-difference relocation for earthquakes in the San Juan Islands (boxed region). Stations are coloured according to their contribution: red indicates a large number of phases used (>100), green is moderate (20–100), and grey is small (<20).

Before earthquakes were relocated with double-difference methods, we located each event with the single-event location program `GENLOC` (Pavlis *et al.*, 2004). The purpose of this was to produce a consistent dataset and representation of errors, making sure all starting locations were determined with the same algorithm and velocity model. We also re-picked some of the S-waves in cases where a converted phase arriving before the S-wave had been picked by mistake. The LSQR method in `hypoDD` is used for the relocation because there are over 100 events, so the error estimates are not reliable. Approximately 45,000 catalogue P and S differential travel

times were used. The first iteration used parameters described in section 2.2, while the second iteration used a damping parameter of 80, down-weighted events with separation distances of >10 km, and down-weighted arrival times with residuals over 6 times the standard deviation.

After the events were relocated the majority of the seismicity lie in two clusters that appear to be parallel to each out in the east-west B-B' cross-section in Figure 2.9. The majority of the seismicity lies between 10–25 km deep.

While simple velocity models may be satisfactory for preliminary earthquake locations, more care is needed to interpret seismicity and relate it to structure. Relocations for data from the San Juan Islands using Vel03 model were found to cause artifacts with many events separated into layers due to the large jumps in the velocity model (Figure 2.4). The model can be improved by increasing the number of layers, thereby decreasing the thickness of each layer and the velocity contrast between layers. We constructed a finer velocity model based on the results from a tomographic study by Ramachandran *et al.* (2005) (Figure 2.4). Figure 2.9 shows relocation results using the two different velocity models. With the Ramachandran model (third row of Figure 2.9) the earthquake hypocentres do not locate preferentially within certain layers but appear distributed across layer boundaries.

We also cross-correlated waveforms in the San Juan Islands to get precise differential arrival times for relocation, using 7308 P-wave and 4385 S-wave arrival pairs observed at 30 stations. However, many of these stations were not deployed for the duration of the study and contribute only a small number of cross-correlation observations suitable for use in `hypoDD`. The closest stations (PGC, SNB and GOBB) contributed the over 500 cross-correlated differential arrival times. In total, 5077 P-wave and 1421 S-wave differential arrival times meet the acceptance criteria after cross-correlation

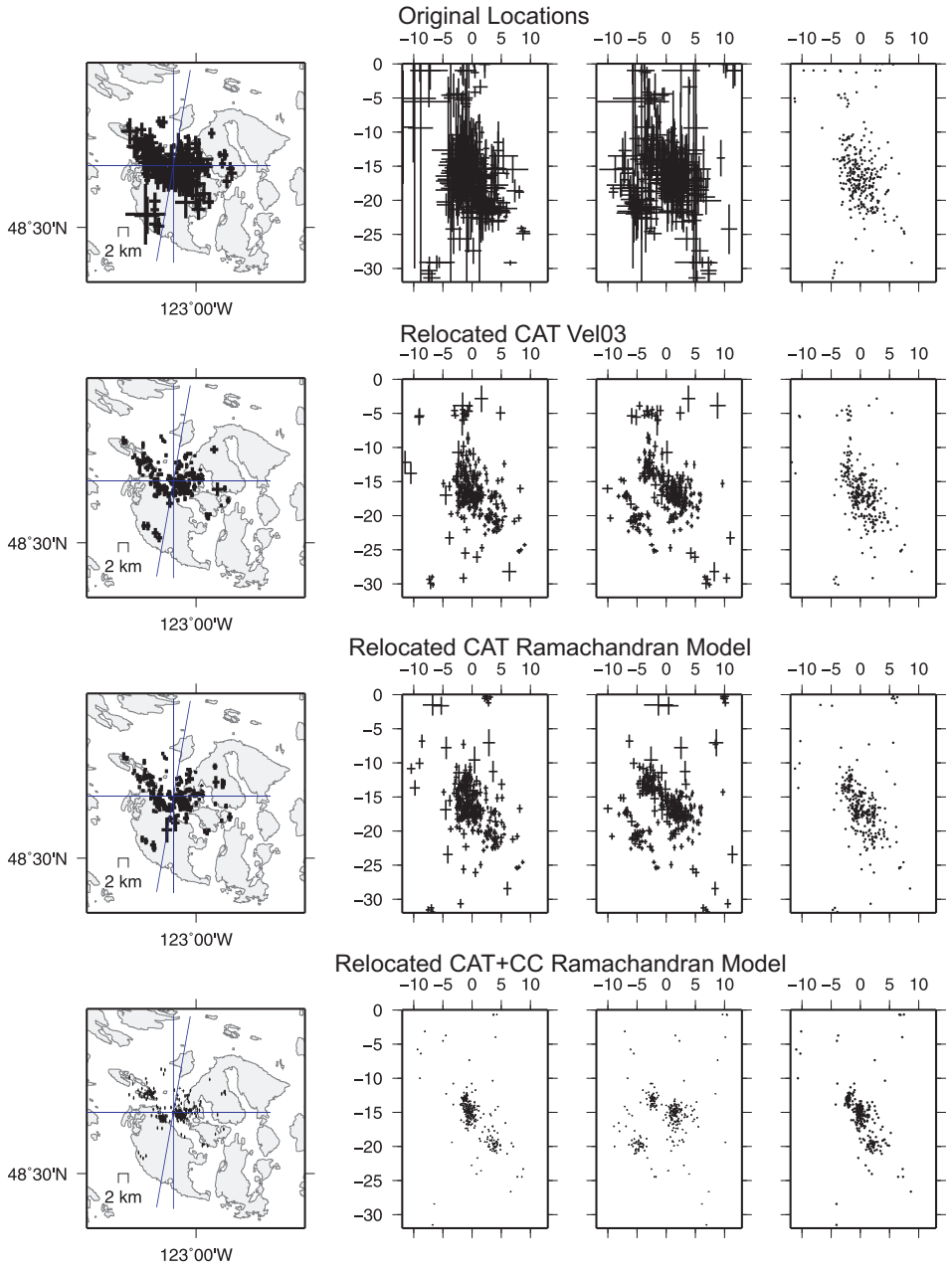

Figure 2.9: Map (left) and cross-sections (middle, right) of earthquake locations and estimated uncertainties near San Juan Islands. The first row (top) shows the original locations from the CNSN catalogue. The second row shows events relocated using `hypoDD` with the standard Vel03 velocity model and catalogue differential arrival times. The third row shows relocated events using the Ramachandran velocity model and catalogue arrival data. The fourth row (bottom) shows relocated events using the new velocity model and both catalogue and cross-correlated waveform data.

for relocating earthquakes in the San Juan Islands. The results from combining cross-correlation and catalogue data and using the Ramachandran model are shown in Figure 2.9 (bottom row). This process relocated 277 out of the original 312 events. When cross-correlation data are added the earthquakes within the dipping structures appear tightly clustered into three groups. We rotate the projection to define the plane where the groups align, assuming they all lie on the same structure. We determine a maximum alignment in depth along cross-section C-C' (Figure 2.9) suggesting this structure is dipping ∼N20°E with a plunge of 60° and strike of ∼290°. A different interpretation might have been made if only catalogue data were considered as only two groups are resolved that dip east (Figure 2.9, middle rows). The interpretation of an east-west striking structure is similar to the strike of nearby mapped faults and therefore is the preferred interpretation (discussed further in section 2.5). The clustered nature of the earthquake locations along the structure may be related to patches of slip due to heterogeneity, such as could be caused by stress concentrations due to asperities or changes in rheology (Waldhauser *et al.*, 2004).

A subset of 50 events from San Juan Island data are used to get reasonable error estimates. This subset includes both cross-correlated and catalogue differential arrival times with events selected to provide maximum information based on the following parameters: number of observations >10, magnitude $M_L \geq 1$ and the origin time after 1996 (since more waveform data were available). The original earthquake hypocentres have mean horizontal error of ∼900 m and vertical error of ∼1500 m. After relocating the events with only catalogue differential arrival times the mean errors were reduced to ∼500 m (horizontal) and ∼1100 m (vertical). When cross-correlation differential times were included the mean errors were further reduced ∼130 m (horizontal) and ∼190 m (vertical). In summary, double-difference relocation using catalogue data reduced the errors by a factor of 2 in the horizontal and 1.4 in the vertical, but

including cross-correlation data reduces the error further by a factor of 4 (horizontal) and 10 (vertical).

2.5 Related Focal Mechanisms and Fault Data

Other datasets can provide supporting information about the seismic activity of faults in an area. We compare our earthquake relocation results from the San Juan Islands with focal mechanisms and fault data from seismic reflection and multibeam bathymetry surveys. Focal mechanisms from Balfour *et al.* (2011) and Mulder (1995) are shown in Figure 2.10 along with the earthquake relocations discussed in section 2.4.2. Many of the focal mechanisms in this group have a nodal plane (potential fault plane) oriented approximately east-west, which agrees with the strike of the seismicity. Only a few focal mechanisms are directly related to the relocated seismicity because the magnitudes of the relocated events are too small to observe enough first motions to determine a focal mechanism. The few that are related have variable nodal plane orientations and sense of slip, and therefore contribute little infromation about the possible rupture plane. These focal mechanisms are a mix of strike-slip and thrust faulting which is characteristic of crustal seismicity in the larger region (Balfour *et al.*, 2011). Principle stress orientations and the stress ratio were determined from this group of focal mechanisms by Balfour *et al.* (2011). The maximum horizontal compressive stress direction ($117^\circ \pm 23^\circ$) is approximately parallel to the strike of the seismicity; however, stress results from surrounding groups of mechanisms suggest that it might be more oblique. The faulting regime supported by the focal mechanisms and stress inversion is oblique-reverse faulting.

Geological mapping of the San Juan Islands by Brandon (1989) suggest that structures

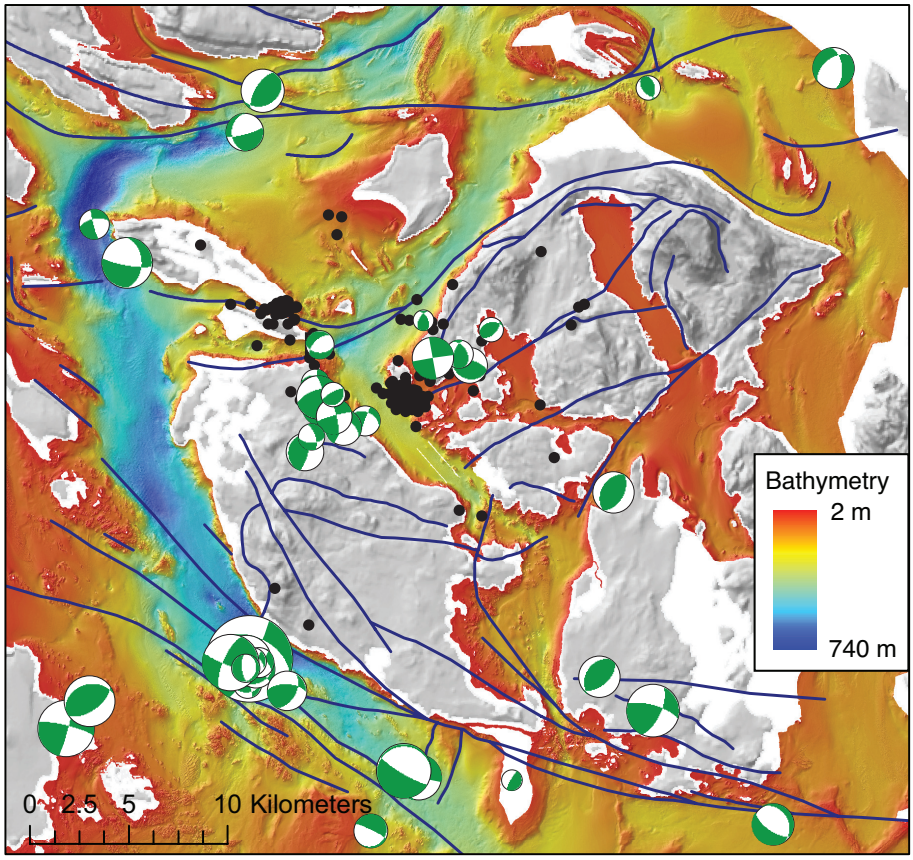

Figure 2.10: Comparison of earthquake relocations (black dots) in the San Juan Islands with focal mechanisms (Balfour, 2011), recently mapped faults (blue lines) and multibeam bathymetry data (pers. comm. Vaughn Barrie).

are related to the Late Cretaceous thrust sheets. A number of interpretations have been applied to these faults (Brandon, 1989; Maekawa and Brown, 1991) but, in general, they do not agree with the northward dipping seismicity we observe from the earthquake relocations. Recent studies involving seismic reflection and multibeam bathymetry surveys consider disturbances and structures on the seafloor which might indicate active faults (pers. comm. Vaughn Barrie). These recently-identified features are combined with detailed field mapping to update the fault map for the San Juan Island to include offshore features (Figure 2.10). Due to the lack of seismicity in the top 10 kms of the crust, and the complicated behaviour of faults near the surface, it is difficult to project the structure outlined by seismicity to the surface and associate

it with any specific fault. However, the east-west strike of the seismicity is similar to the strike of recently mapped faults both north and south of the San Juan Islands, as well as, other major faults in the region, such as the Tacoma fault (Sherrod *et al.*, 2004), Devils Mountain fault (Johnson *et al.*, 2001) and Seattle fault (Blakely *et al.*, 2002).

Less evidence is available to support recent faulting in the Fraser Valley of southwest British Columbia. Pullan *et al.* (1998) investigated the structure of the Fraser River delta using seismic reflection surveys and found only one or two instances where disturbed strata could indicate faulting. There are a few well exposed faults in this region: the Sumas Mountain Fault, Vedder Fault, Boulder Creek fault and Kendall fault scarp (Barnett, 2007). These faults are all located in the southeast of the study region and trend southwest-northeast, in the same direction as the streaks of seismicity described in section 2.4.1. While there appears to be high levels of seismicity beneath the Vedder Fault, our relocations did not reveal any structure within the seismicity. Where we observe streaks of seismicity there is little evidence of faulting near the surface. This could suggest that whatever faulting occurs beneath the delta does not disturb the overlying sediments in a well preserved manner, or that faulting occurs deep in the crust and rarely offsets near-surface sediments.

2.6 Conclusions

We relocated earthquakes in southwest British Columbia and beneath the San Juan Islands, Washington, using catalogue and waveform differential arrival times. These precise relative earthquake locations help illuminate seismically active structures and relate them to recently mapped surface faults. Historically, magnitude 6–7 earth-

quakes occur in the North American crust in this region, but it is difficult to determine the structures on which these events occurred and where they may occur in the future.

We used various velocity models for our relocations and observed that more detailed models reduced the vertical relocation errors and removed artifacts caused by large velocity contrasts at layer boundaries. A subset of data from each region was selected to relocate via SVD to quantify the relocation errors. On average, errors in catalogue locations are 1000 m in the horizontal and 2000 m in the vertical. Double-difference relocation using catalogue data reduces errors by at least a factor of 1.4; if both cross-correlation and catalogue data are used errors are reduced to ∼100 m in the horizontal and ∼200 m in the vertical.

This study identifies an active structure beneath the San Juan Islands that strikes ∼290° and dips northward (N20°E) at an angle of 60°. The seismicity is concentrated between 10–20 km depth and extends 10–15 km along strike. The east-west strike of the structure is similar to those of recently-mapped surface faults; however, no shallow seismicity (<10 km) has been observed so it cannot be associated with a specific fault. Some focal mechanism nodal planes also support an east-west strike fault with a steep dip. The focal mechanisms and stress inversion results suggest an oblique-reverse faulting regime. This structure may also coincide with the location of a magnitude 6 earthquake in 1909 and magnitude 5.5 in 1920, although the location and depth of these events are not well known. The inclusion of waveform cross-correlation data was vital for the correct interpretation of this data, as without it the structure could be interpreted as two east-dipping faults.

Seismicity in the Fraser Valley of British Columbia is less well defined but contains several narrow streaks of seismicity extending from the surface to ∼20 km depth.

Similar streaks have been observed near the San Andreas fault and attributed to changes in rheology or stress concentrations between locked and creeping portions of the fault (Waldhauser *et al.*, 2004).

This study has shown that precise earthquake relocations can provide insight into structures that are "hidden" and seismicity that does not correlate with surface faulting. The observed seismicity cluster might be associated with different patches of fault slip, and with the incorporation of more historical events and continued monitoring, this approach could illuminate the full extent of the structure.

Chapter 3

Mapping Crustal Stress and Strain in Southwest British Columbia

This paper investigates the orientation and sources of stress in the forearc of the Cascadia subduction zone in southwest British Columbia, using Bayesian inversion results from focal mechanism data and comparing results with GPS derived short-term strain rates. The subduction margin in this region includes a change in orientation from N–S in Washington State to NW–SE in British Columbia. Over 1000 focal mechanisms from North American crustal earthquakes have been calculated to identify the dominant style of faulting and ∼600 were inverted to estimate the principal stress orientations and the stress ratio. Our results indicate the maximum horizontal compressive stress orientation changes with distance to the trench, from approximately margin-normal along the coast to approximately margin-parallel 100–150 km inland from the coast. Comparing stress orientations with GPS data, we relate the margin-normal stress direction to subduction-related strain rates due to the locked interface between the North America and Juan de Fuca plates just west of Vancouver

Island. Further from the margin the plates are coupled less strongly and the margin-parallel maximum horizontal compressive stress in the North American Plate relates to the northward push of the Oregon Block, which is also observed in the horizontal shortening direction of the residual strain rates, after the subduction component is removed.

3.1 Introduction

Southwest British Columbia is located above the Cascadia subduction zone, where the young Juan de Fuca plate subducts beneath the North American Plate at a rate of ∼40 mm/yr [DeMets *et al.*, (1990); (1994)] as shown in Figure 3.1. Crustal seismicity is concentrated in the Puget Sound and southern Vancouver Island regions. In many areas, hypocentre depths span the entire crustal thickness (∼30 km beneath Vancouver); however, they shallow to the east of Vancouver in the Coast Mountains to <15 km and along the west coast of Vancouver Island (Figure 3.1). The largest known crustal earthquake in the region (M_s 7.3) occurred in 1946 on Vancouver Island (Figure 3.1).

The majority of research on the Cascadia subduction zone has focused on subduction earthquakes that rupture the interface between the plates and could cause widespread damage along the coast of British Columbia, Washington, Oregon and Northern California (Hyndman *et al.*, 1996). However, fewer studies have been carried out to understand faulting in the North American crust in British Columbia that can produce large, crustal earthquakes up to M 7.3. Southwest British Columbia represents a unique region of the Cascadia subduction zone due to the change in the strike of the margin. In addition, there are variations in the style of faulting in the crust

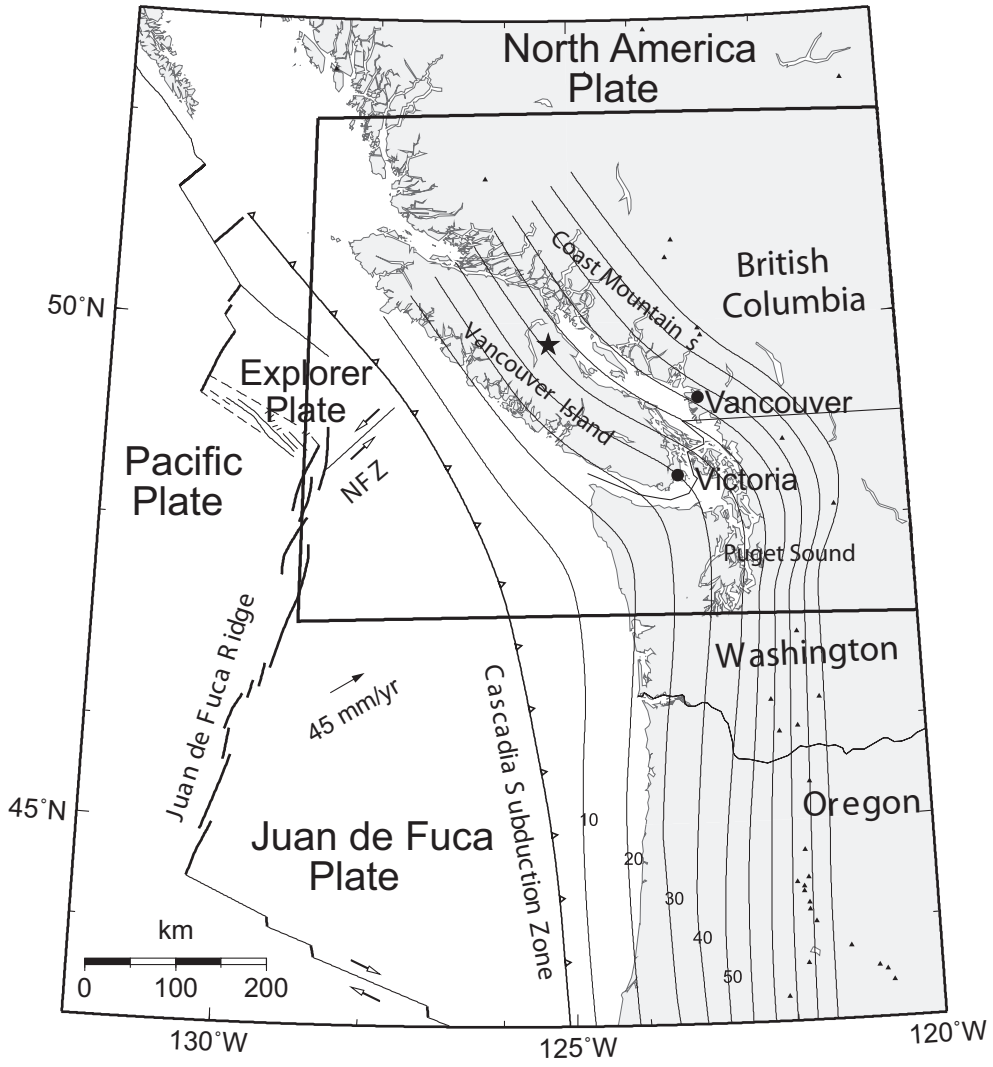

Figure 3.1: Northern Cascadia subduction zone. Contours show depth to the top of the subducting slab in kilometres (McCrory, 2004). Area outlined by a box is the region considered in this study. The star shows the approximate location of the M 7.3 1946 Vancouver Island earthquake.

and complex seismicity patterns that do not appear to align with surface faulting features. To understand the faulting in the region, and the seismic hazard posed on the surrounding populations, it is necessary to better understand the forces driving faulting.

3.1.1 Previous Studies

To date, relatively few focal mechanisms have been determined for earthquakes in British Columbia. Focal mechanisms have been calculated for specific significant earthquakes (mainshock and aftershocks) [Cassidy *et al.*, (2000); Rogers and Hasegawa, (1978)] or regions of interest such as within the subducting Juan de Fuca plate [Wada *et al.*, (2010); Bolton, (2003)]. Only a few studies have looked at focal mechanisms over decadal times scales and have included small crustal earthquakes (M<3). Mulder (1995) determined focal mechanisms for 111 crustal earthquakes as small as magnitude 1.0 from 1975–1991 (Figure 3.2, blue). Ristau *et al.* (2007) set up an automated method for determining regional moment tensor solutions for moderate sized earthquakes (M≥4) and the Pacific Geoscience Centre has a catalogue of these back to 1995 (Figure 3.2, red). Focal mechanisms for smaller events from 1992–2001 have been determined by various analysts but have not been reviewed and graded for quality.

Formal stress inversions have proved difficult with seemingly unstable results due to the sparse focal mechanism data set. Mulder (1995) investigated stress in the region by considering composite P- and T-axes plots and inverting focal mechanisms for stress using the Focal Mechanism Stress Inversion package by Gephart and Forsyth (1984) and Gephart (1990). The inversion provided good first-order estimates of the trend/plunge of the principle stress orientations (maximum $S_1 = 10/173°$, intermediate $S_2 = 06/082°$ and minimum $S_3 = 78/322°$); however, the approach assumes the stress is homogeneous over the entire region. This assumption is a crude approximation due to plate coupling along the subduction interface and changes in margin strike through this region. Mulder (1995) mentions variations in the orientation of the P- and T-axes with distance from the margin that alludes to this; however, no formal

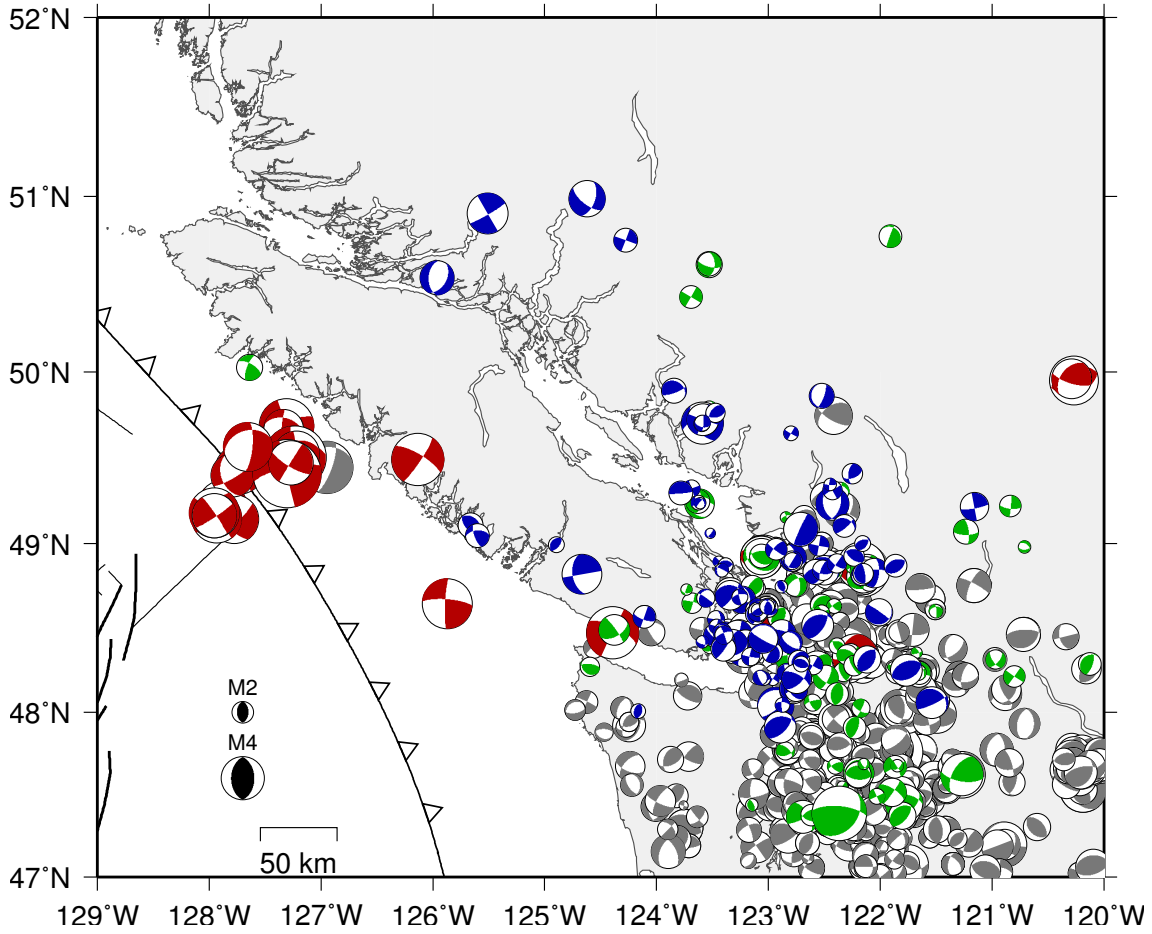

Figure 3.2: Source mechanisms of crustal earthquakes in the study area from previous studies: moment tensor solutions from Ristau (2007) in red, focal mechanisms from 1975–1991 from Mulder (1995) in blue, other CNSN focal mechanisms from 1992–2002 in green, PNSN focal mechanisms in grey. Source mechanisms are scaled according to magnitude.

inversions were performed on subsets of the data because of the lack of focal mechanisms along the west coast of Vancouver Island (Figure 3.2). Ristau *et al.* (2007) used moment tensor solutions to invert for stress but obtained unstable results for Vancouver Island, probably due to the smaller number of crustal events with M>4 and variation in the stress field over the region which was assumed homogeneous in the inversion.

These studies led to the computation of numerical models to explain the origin of margin-parallel stresses in the forearc of the Cascadia subduction zone. Stresses in the forearc are explained by Wang (1996), Wang and Jiangheng (1999) and Wang (2000) as being related to the balance between the subduction coupling force (strength of the subduction fault) and the gravitational force from the continental margin topography. Wang and Jiangheng (1999) suggest that Cascadia has a low stress forearc because the margin-normal compression from subduction does not seem to exceed the vertical stress from topography due to weak coupling along the subduction fault.

Studies of crustal seismicity in the Cascadia forearc have tried to determine the validity of these models by investigating stress and strain. Currie *et al.* (2001) related the fast direction of crustal anisotropy to margin-parallel compression stress by comparing their shear-wave splitting results to the maximum compressive stress direction determined from earthquake focal mechanisms and borehole stress studies across Cascadia. Lewis *et al.* (2003) investigated variations in strain from both earthquake focal mechanism inversions and geodetic observations along the Cascadia forearc from southern Oregon to northern Washington. They suggest that strain determined from focal mechanisms reflected the nonrecoverable component of deformation related to the rotation of the Oregon coast block defined by McCaffrey *et al.* (2000).

In this study we create a new Canadian National Seismic Network (CNSN) focal mechanism database by: (1) computing focal mechanisms from first motion observations of 550 small events (M 1–4) in the North American crust from 2002–2009; (2) reviewing mechanisms determined from 1992–2001 for consistent quality control to incorporate them with appropriate uncertainties into the database; and (3) combining previously determined focal mechanisms from 1975–1991 by Mulder (1995) with the new solutions from (1) and (2) to complete the database. With the completed

database, we perform stress inversions on spatial subsets of the data to investigate variation in stress direction and examine whether stress within the region is homogeneous.

3.2 Focal Mechanism Determination

The source mechanism of an earthquake is commonly described by a focal mechanism or moment tensor. Focal mechanisms are determined using the polarity of the direct P-wave and/or the SV/P amplitude ratio and the take-off angle of the ray from the source. Moment tensor solutions require more complex computation involving waveform inversion techniques.

The data coverage of the focal sphere is dependent on the station geometry, and poor coverage can result in poorly defined focal mechanisms with multiple solutions that fit the observations. Uncertainties in estimated focal mechanism parameters are often poorly defined, but are frequently described in terms of the range of solutions that fit all P-wave observations. It is often difficult to differentiate between the fault plane and the auxiliary plane unless independent information is available, such as a surface break of a fault. Polarity reversals are another common problem and were corrected for at two CNSN stations in British Columbia.

In this study, the FPFIT method from Reasenberg and Oppenheimer (1985) is used to compute focal mechanisms. This inversion uses a two-stage grid search for the solution that minimizes the misfit with observed P-wave first motions. The grid searches involve an initial coarse grid over the entire range of solution parameters (10° increments) followed by a smaller grid (1° increments) to refine the solution.

The method includes two weighting functions. An observational weighting is based on one or more of the P-wave pick uncertainty, signal-to-noise ratio, or event-to-station distance. We choose to use the event-to-station distance to define the pick uncertainty as the signal-to-noise information is not always available. The other weighting function is related to how close an observation is to a nodal plane. If the source model is correct, the P-wave radiation is minimum at the nodal planes and it is therefore difficult to correctly pick first motion here. Hence, observations near modelled nodal planes are automatically down weighted within FPFIT. The inversion also attempts to formally estimate the uncertainty in the solution. These uncertainties are taken into consideration for the final grading of the focal mechanism where a quality grade from 1-5 is given to be consistent with focal mechanisms determined in previous studies. The grading of the solution is described in Mulder (1995) where 1 is excellent and 5 is very poor. When grading solutions, several factors are considered: solution uncertainty from the inversion, alternative solutions, and mispicked first motions.

3.2.1 Focal Mechanism Results

In this study, before stress inversions were performed, an updated focal mechanism database is required. As discussed previously, the database was complete from 1975–1991 for all events with M>1 and from 1975–2007 for events with M>4. To complete the database, focal mechanisms determined between 1992–2001 were reviewed and assigned quality grades. We attempted to determine focal mechanisms for all M>1 crustal events from 2002–2009 that have more than six first motion measurements.

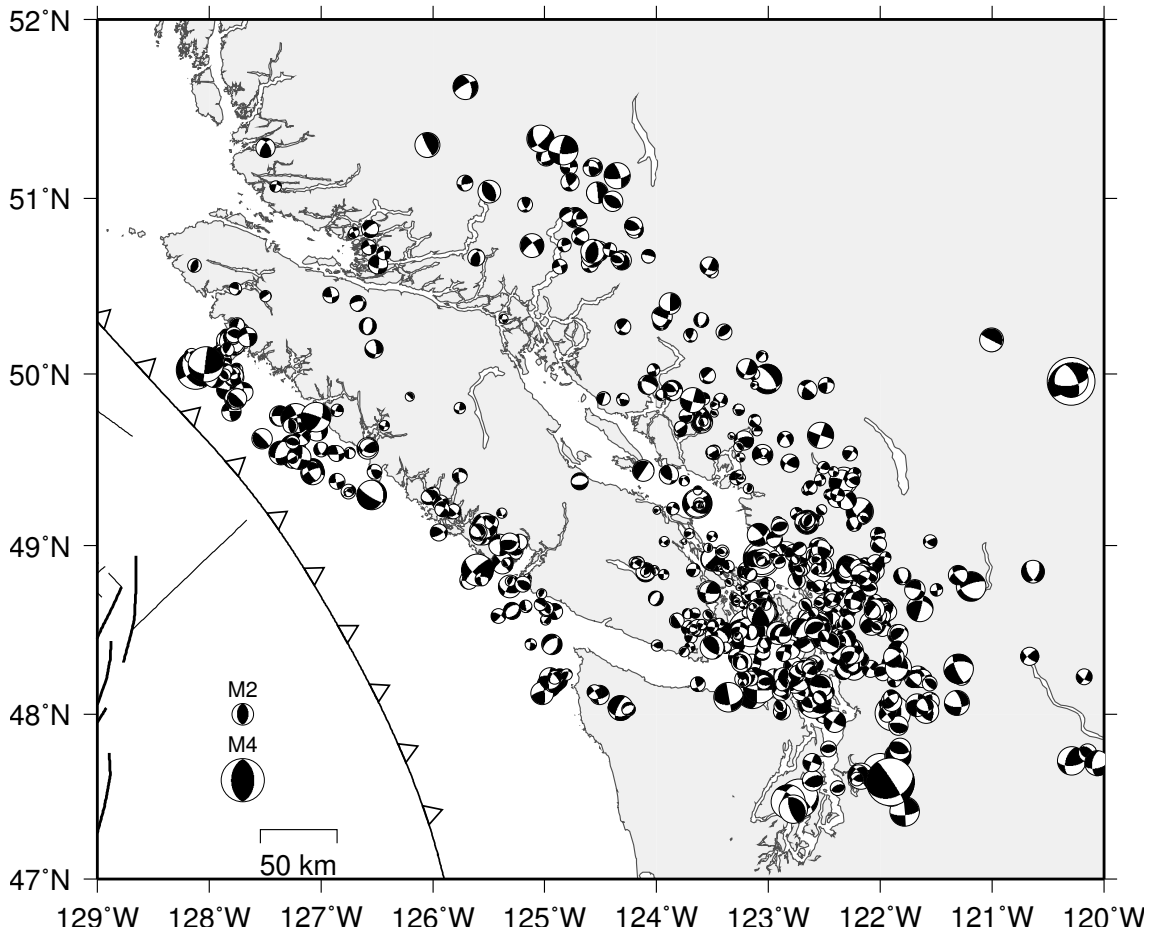

Figure 3.3: Focal mechanisms of crustal earthquakes determined in this study using FPFIT (black).

A total of 550 new focal mechanisms for crustal earthquakes in southwest British Columbia were calculated (Figure 3.3), increasing the database to 939 events. Ternary diagrams show focal mechanism information (P, T and B axes) in Figure 3.4 (Frohlich, 1992) and determine the dominant style of faulting based on definitions developed for the World Stress Map Project by Zoback (1992). There is a great deal of variability in the faulting styles (regardless of focal mechanism quality), but significantly fewer normal-faulting events: only 10–14% of the focal mechanisms are considered normal-faulting, while strike-slip faulting and thrust-faulting occur 30% and 27–33% of the time respectively, and 23% are considered undefined (Figure 3.4).

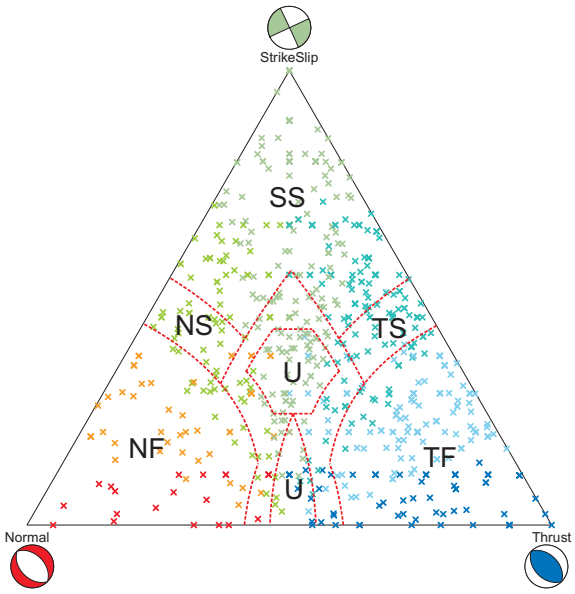

Figure 3.4: Ternary plot of focal mechanism data. Each point is plotted based on the plunge of the P, T and B axes of the mechanism Frohlich (1992). The colors represent the rake of the focal mechanism: red is pure normal, blue is pure thrust and green is pure strike-slip. The dashed lines divide the triangle into faulting styles based on definitions by Zoback (1992): NF is normal faulting, NS is normal and strike-slip, SS is strike-slip, TS is thrust and strike-slip, TF is thrust faulting and U is undefined.

Faulting style is important for probabilistic hazard analysis as it can help by: 1) defining seismic source zones using small earthquakes; and 2) determining the appropriate attenuation relationship in a given region for moderate to large events (M>4) [Convertito and Herrero, (2004); Bozorgnia *et al.*, (2010)]. In general, the focal mechanisms in Figure 3.5 show highly variable faulting styles between closely spaced events, making it difficult to choose a style of faulting for a hazard model. However, there are some exceptions. The Coast Mountains region north of Vancouver experiences dominantly strike-slip faulting with no pure-normal or pure-thrust faulting events, and southern Puget Sound experiences dominantly thrust faulting with few normal faulting events.

The variation in faulting indicates a complex style of deformation, possibly including old reactivated faults and conjugate faults. It appears that faulting is more likely to

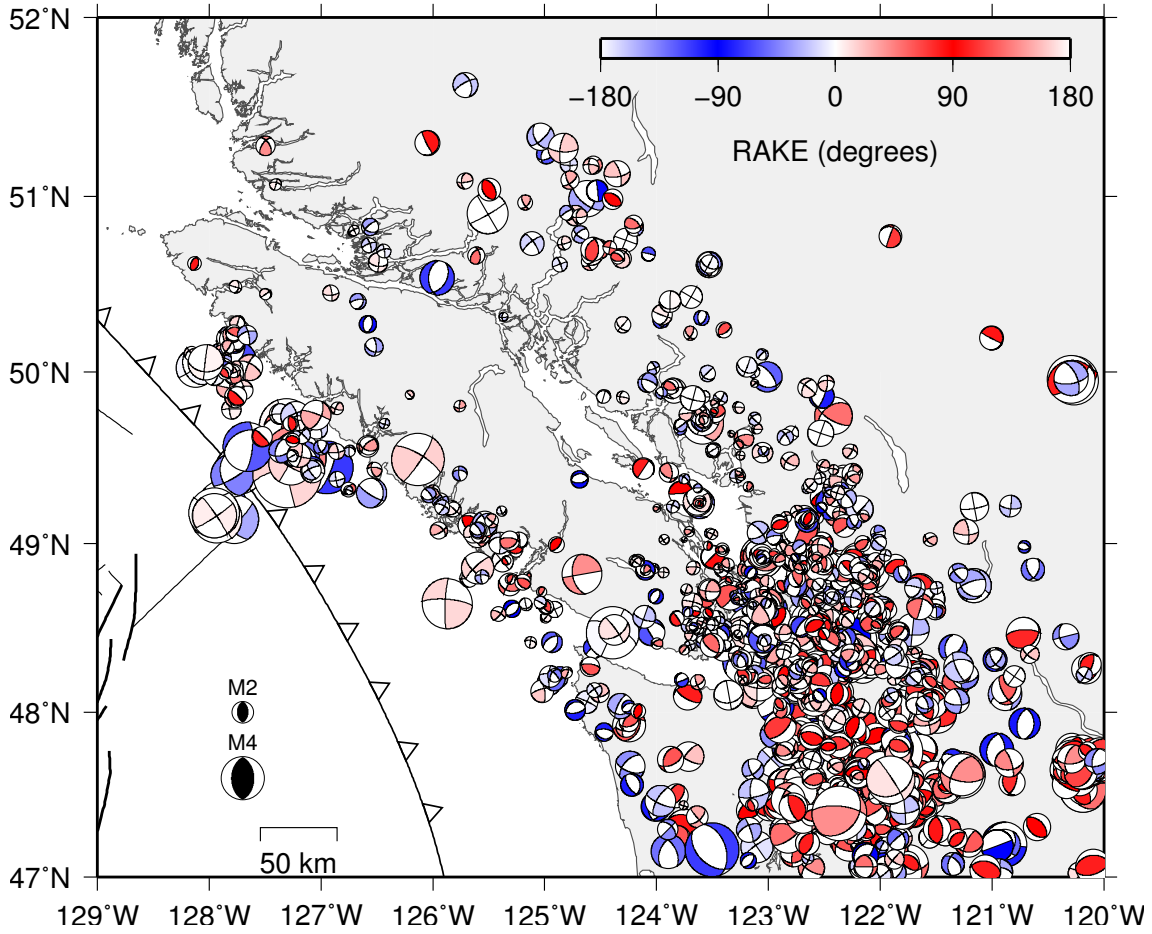

Figure 3.5: Updated focal mechanisms database for earthquakes in the North American crust colored according to rake: red indicates pure thrust faulting, blue pure normal faulting and white is strike-slip faulting.

occur on numerous smaller faults over a large area rather than a more narrow "San Andreas" type fault system. The dominant mix of strike-slip and thrust faulting suggests that the intermediate and least compressive stresses may be of similar magnitude, which is in agreement with previous studies [Wang and Jiangheng, (1999); Wang, (2000)].

3.3 Stress Inversion

To determined the in-situ stress, we invert focal mechanisms for the four stress parameters: the orientations of the three principal stress axes (maximum S_1, intermediate S_2 and minimum S_3 compressive stress) and the stress ratio (R).

McKenzie (1969) demonstrated that a single focal mechanism puts little constraint on the stress tensor, as all that can be determined is that the axis of maximum compressive stress lies somewhere in the dilatational quadrant. Wallace (1951) and Bott (1959) hypothesized that slip on a fault occurs in the direction of maximum shear stress, which depends on both the orientation of the fault plane in the stress field and the relative magnitude of the principal stresses. From this and the additional assumption that all motion on faults in a discrete volume of crust are caused by the same stress tensor, it is possible to invert a group of fault slip data or fault plane solutions for the principal stress directions and stress ratio. Lund (2000) explains that it is necessary to have at least four focal mechanisms to determine stress, however in this study we have found that more than 10 are required to provide a stable result.

As focal mechanism data only deal with the direction of slip at the fault plane, the inversion does not constrain the magnitude of the principal stresses but yields the stress ratio, R, which describes the shape of the stress ellipsoid,

$$R = (S_2 - S_3)/(S_1 - S_3). \tag{3.1}$$

There have been many approaches to the stress inversion problem, including deterministic linear approaches [Michael, (1984); (1987)], grid searches [Gephart and Forsyth,

(1984); Gephart, (1990); Abers and Gephart, (2001)], and a probabilistic Bayesian approach (Arnold and Townend, 2007). This study is based on the Bayesian approach.

3.3.1 Bayesian Method

The benefits of using the Bayesian approach by Arnold and Townend (2007) is that prior knowledge of the stress tensor can be incorporated into the inversion and observational errors in the focal mechanism data may also be included. Each focal mechanism is described by a strike, dip, rake and precision (τ). The precision is a measure of the average uncertainty in the strike, dip and rake of the focal mechanism, e.g., if the error in the mechanism is low ($< 10^{\circ}$) the precision is high ($\tau = 20$), and is based on the Matrix-Fisher distribution. Similar to Arnold and Townend (2007), we do not include a previously determined estimate of the stress tensor orientation in the prior but assume its orientation is uniformly distributed. This can be done due to the reflectional symmetry of the stress tensor, which restricts the ranges of the Euler angles that transform the focal mechanism orientation to the orientation of the principal stress axes.

As previously discussed, the focal mechanisms in the database are from multiple sources and not all sources include a complete description of the focal mechanism uncertainties. To address this, a quality grade was assigned to each mechanism (Arnold and Townend, 2007) which was then converted into an uncertainty based on Table 3.1.

To observe spatial variations, the data were divided into subsets based on location. We chose to use a K-means clustering algorithm (MacQueen, 1967) to divide the data

Quality Grade	Uncertainty
1	5°
2	10°
3	20°
4	30°
5	not used

Table 3.1: Conversion between quality grades for focal mechanisms defined by Mulder (1995) and uncertainties in the strike, dip and rake, for input into the Bayesian stress inversion.

based on latitude and longitude, with an average of 20 focal mechanisms per cluster. The clustering does not include depth because few focal mechanisms are located in the uppermost 5 km of the crust, where stress is likely to change the most, so we assume stress remains constant throughout the thickness of the crust. The clustering algorithm determined 34 clusters, however three of these had too few events (<4) for a stable inversion.

3.3.2 Stress Results

Thirty-one groups of focal mechanisms were inverted for stress. The Bayesian inversion algorithm samples the posterior probability density (PPD) and computes marginal distributions, and the mode, mean and maximum a posteriori (MAP) estimation for each of the seven model variables (trend and plunge of the three principal stress axes and the stress ratio). An example of the output is shown in Figure 3.6. The inversion also calculates the maximum horizontal compressive stress direction (S_{Hmax}) formulated by Lund and Townend (2007), after Lund (2000). SHmax is plotted for each group on a map of the region in Figure 3.7 (red arrows). The 95% confidence region of S_{Hmax} for each group is shown in Figure 3.8. Groups 18, 23 and 27 have large asymmetric confidence regions because the majority of the focal

mechanisms in these groups have low grades (3–4) and fewer focal mechanisms were used in the inversion (7–12).

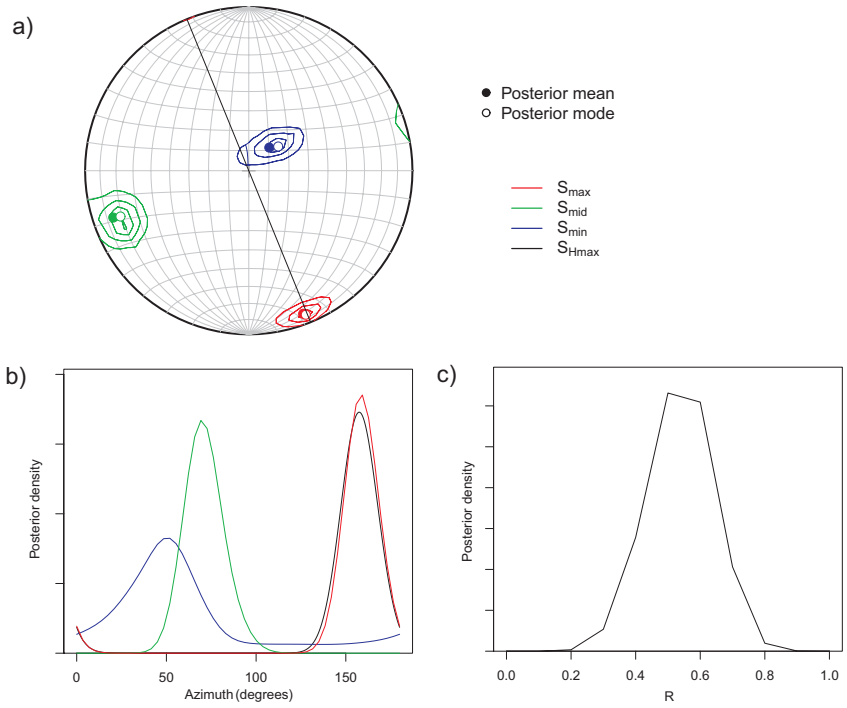

Figure 3.6: Example output of Bayesian stress inversion for group 1 in Figure 3.7. (a) PPD contours for the three principle stresses and S_{Hmax} in a stereographic projection. The open and closed circles represent the posterior mode and mean respectively. (b) Marginal PPDs for the stresses and S_{Hmax} as a function of azimuth. (c) Marginal PPD of the stress ratio.

The results in Figure 3.7 show two distinct sets of stress orientations. One set is composed of results with northeast-southwest orientation located on the west coast of Vancouver Island. The other set is composed of results located further inland, with stresses rotating from north-south in Washington to northwest-southeast further north. The S_1, S_2 and S_3 axes from the stress inversions for each group are plotted on a ternary diagram in Figure 3.9. The results range from strike-slip to thrust faulting regimes regardless of the S_{Hmax} direction. Although there are normal faulting focal mechanisms in the database, the stress results are not consistent with a normal faulting regime.

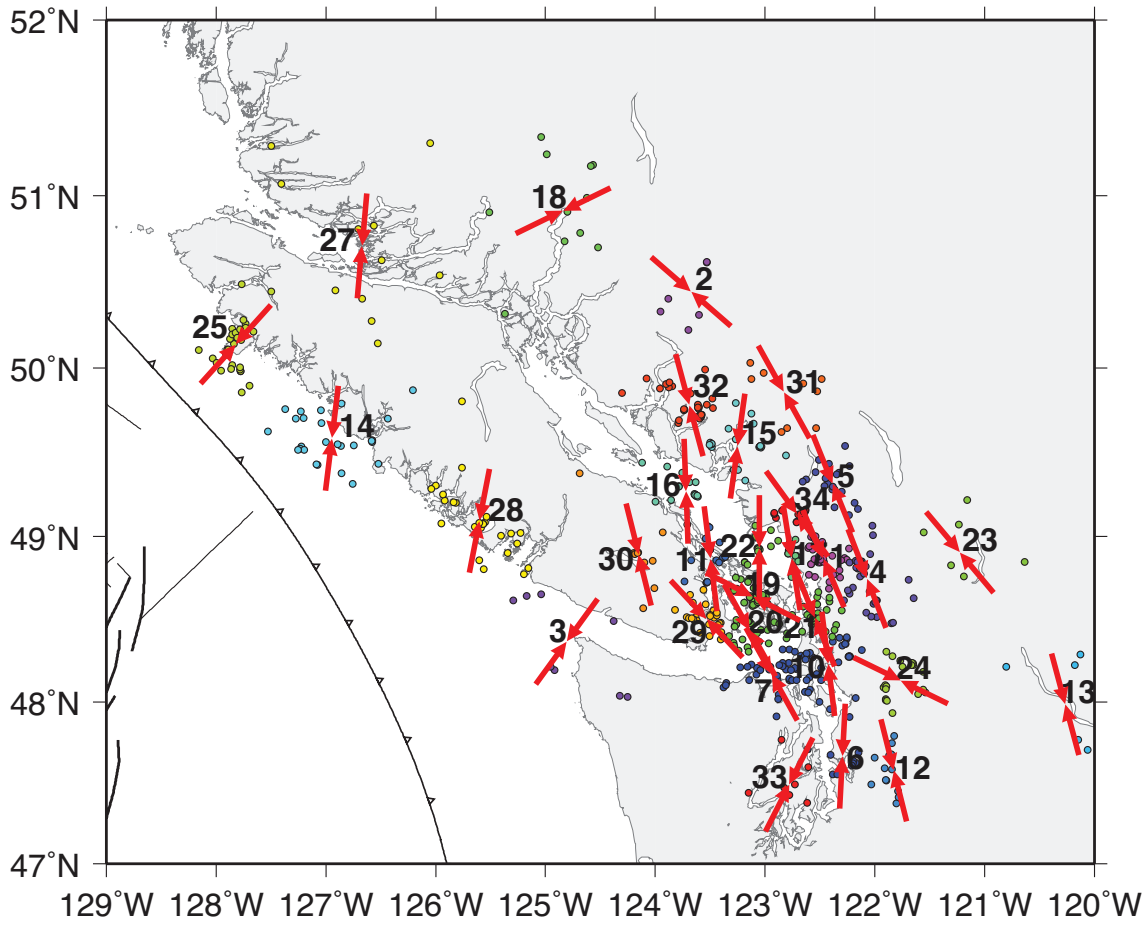

Figure 3.7: Stress inversion results. Maximum horizontal compressive stress is shown by the red arrows plotted at the centre of each group. Locations of earthquakes are colored according to their cluster.

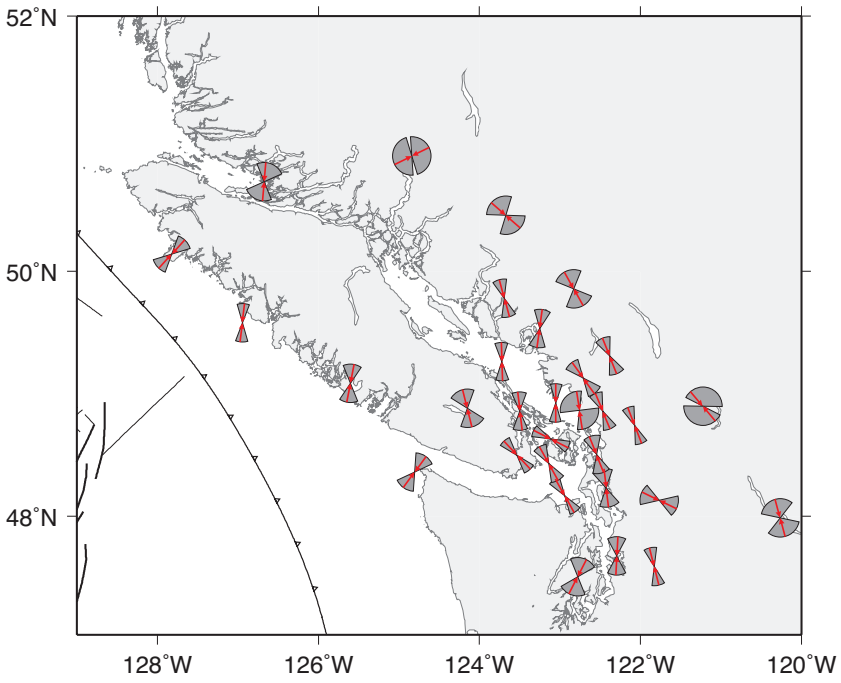

Figure 3.8: Maximum horizontal compressive stress directions plotted with wedges that show the 95% confidence of the result.

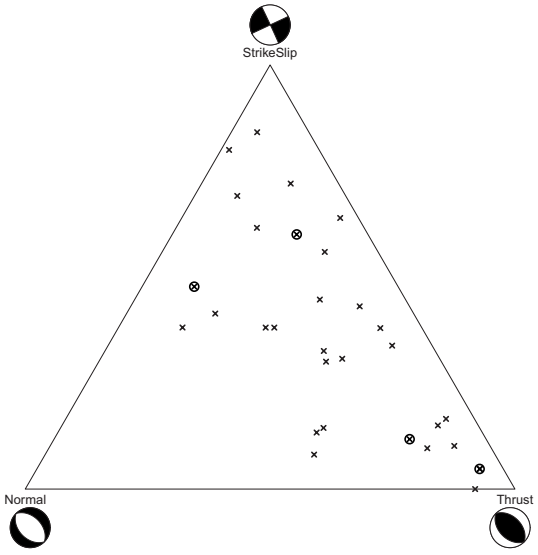

Figure 3.9: Ternary plot of stress results. Each point is plotted based on the plunge of the S_1, S_2 and S_3 axes of the mechanism. The crosses with circles are those groups along the west coast of Vancouver Island and the crosses are the groups further inland. Note that these results fit within the distribution of the other groups even though their S_{Hmax} orientations differ.

3.4 Comparison with GPS Strain Rates

To help identify the reason for the change in stress direction with distance from the margin, the S_{Hmax} results are compared with the direction of maximum horizontal shortening (e_{Hmax}) from Global Positioning System (GPS) strain data. A compilation of GPS data in southwest British Columbia and northwest Washington is used to derive crustal strain rate directions. As a first step, we derive horizontal GPS velocities using an updated version of the analysis described in Mazzotti *et al.* (2003). The horizontal GPS velocities include results from about 40 permanent stations from 1996–2008 (including Western Canada Deformation Array, Pacific Northwest Geodetic Array and Plate Boundary Observatory stations) and 60 campaign stations from 1992–1999, concentrated around Vancouver Island. The velocities from campaign data have a reduced weight in the calculations due to the lower quality of some data. The velocities, shown in Figure 3.10, are aligned to the International Terrestrial Reference Frame ITRF2000 and rotated relative to stable North America (Altamimi *et al.*, 2002) .

To a first order, the horizontal GPS velocities mainly reflect the strain loading of the Cascadia forearc by the locked Cascadia subduction fault [e.g., McCaffrey *et al.*, (2000), Mazzotti *et al.*, (2003), McCaffrey *et al.*, (2007)]. This deformation is mostly elastic and will be recovered during the next Cascadia megathrust earthquake. The GPS velocities also contain smaller, secondary signals such as the margin-parallel shortening of the forearc that drives deformation and seismicity in the Puget Sound region [e.g.,Mazzotti *et al.*, (2002)]. To separate these two components (subduction-loading and forearc tectonics), we define two sets of GPS velocities: an original (uncorrected) set and a residual set corrected for the elastic interseismic loading from Cascadia subduction. The residual set is derived by removing model-based predicted

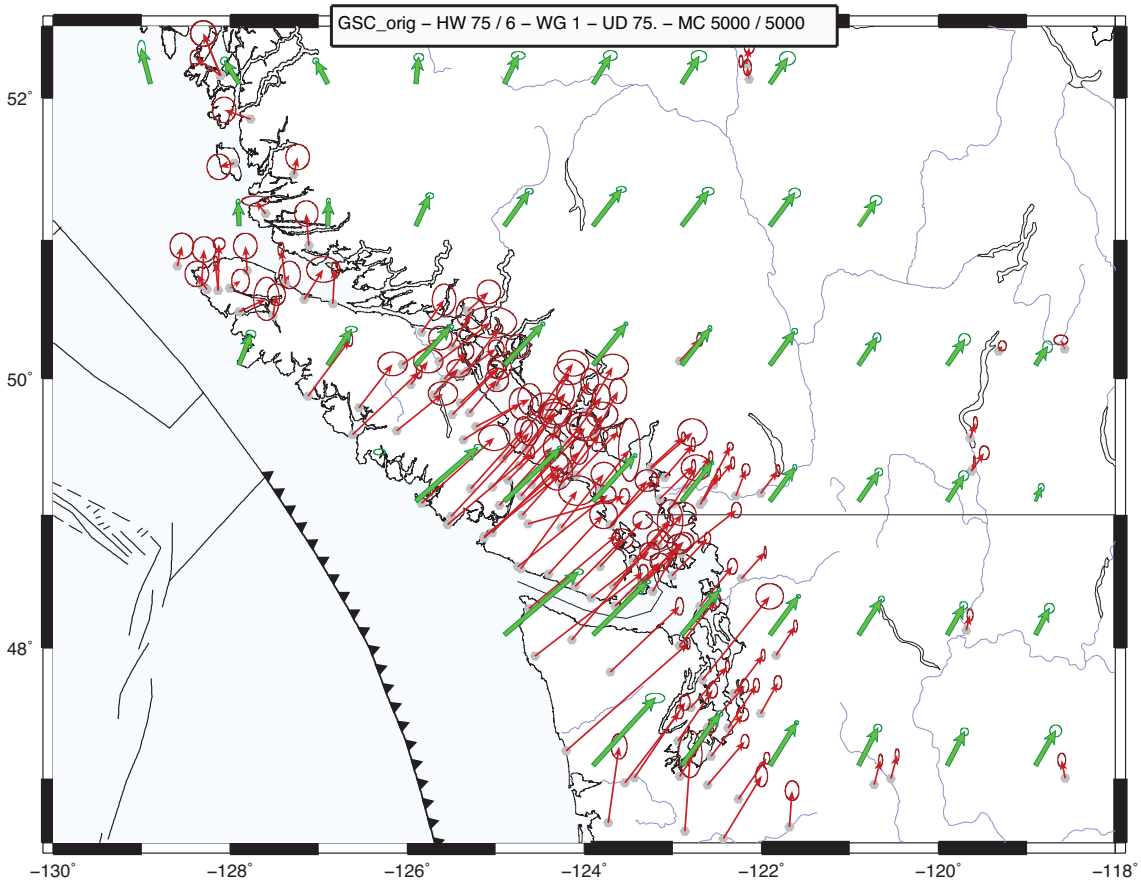

Figure 3.10: Observed GPS velocity field (red arrows with error ellipses) and smoothed velocities (green arrows with error ellipses) used to derive strain rates in Figure 3.11a.

velocities from the original GPS velocities. The predicted velocities are based on a 3-D elastic model of interseismic locking of the Cascadia subduction fault (Wang *et al.*, 2003).

To calculate the direction of strain rates from horizontal GPS velocities, we used an updated version of the velocity and strain rate smoothing method described in Mazzotti *et al.* (2001) consists of running a smoothing window on a grid to calculate interpolated horizontal velocity and strain rate tensor at each grid point from the GPS velocities. At each grid point, a Gaussian weighting function with an adaptive half-width and its spatial derivative were used to calculate the interpolated velocity

and strain rate. The Gaussian half-width is defined based on the density of nearby GPS sites and a prescribed minimum wavelength (here 75 km). The half-width varies between 75–100 km for the Vancouver Island–Puget Sound region, and increased to 100–200 km for the central and eastern British Columbia and Washington.

At each grid point, the direction of maximum horizontal shortening rate was defined by the direction of the smallest of the two strain rate principal axes (extension positive convention). In the very few cases where the strain rate tensors are pure extension, this direction actually represents that of minimum horizontal extension. The standard errors on the strain rate tensor components, including the principal axis directions, are based on a numerical simulation that accounts for: (1) the standard error on the input GPS velocities; (2) the coherence of the GPS velocities used to derive the strain rate tensor; and (3) the density of GPS sites near the grid point.

We compared e_{Hmax} to the S_{Hmax} directions from focal mechanism inversion in Figure 3.11, as they are expected to be similar based on Hooke's law. The results of the two GPS strain calculations (original and residual) and their standard errors are shown in this figure. The uncertainties illustrate the poorly resolved results in residual strain rates where the orientation changes from northwest to northeast near the Coast Mountains. We investigated the effect of the amount of locking in the subduction model on the residual strain rate directions by considering a range of models with varied amounts of locking from 0–100%. We show the results of residual strain rates from removing models with 75% and 100% locking in Figures 3.11b and 3.11c respectively. Models with less than 75% locking are very similar to the observed GPS strain rates (Figure 3.11a) and are therefore not included. The main effect the locking model has on the residual strain rate directions is how far inland the e_{Hmax} directions changes from margin perpendicular to margin parallel, i.e. the higher the locking in

the model the further from the margin this change in direction occurs.

The results in Figure 3.11 show similar S_{Hmax} and e_{Hmax} orientations along the west coast of Vancouver Island when the subduction component is included (Figure 3.11a), however they differ further inland from the margin. The residual strain rates shows similar directions for S_{Hmax} and e_{Hmax} further from the coast near Victoria and Vancouver, and different directions along the coast (Figure 3.11c). This agrees with studies by Wang (2000) which suggest stress is strongly influenced by subduction loading near the coast where the overriding plate is coupled with the subducting plate, while further inland, where they are less strongly coupled, stress is related to the residual strain due to the northwards push of the Oregon Block. Wells and Simpson (2001) and McCaffrey *et al.* (2007) identified the Oregon Block from GPS velocities and describe it as rotating clockwise, with a northward motion along the coast of southern Washington and Oregon.

3.5 Implications for Understanding Tectonics

The tectonics of southwest British Columbia are complicated by the locked Cascadia subduction zone, the bend in the subducting plate, the change in strike of the margin and the northward push of the Oregon Block. The stress results reflect the dominant strain accumulation which changes across the region. Near the margin, along the west coast of Vancouver Island, earthquakes in the upper plate are caused by the strain build-up due to the convergence of the North American and Juan de Fuca plates. This is due to the locked interface between the plates and the transfer of stress to the upper plate causing it to deform by shortening and uplift. The deformation was recognized and is well documented as part of the great earthquake cycle proposed

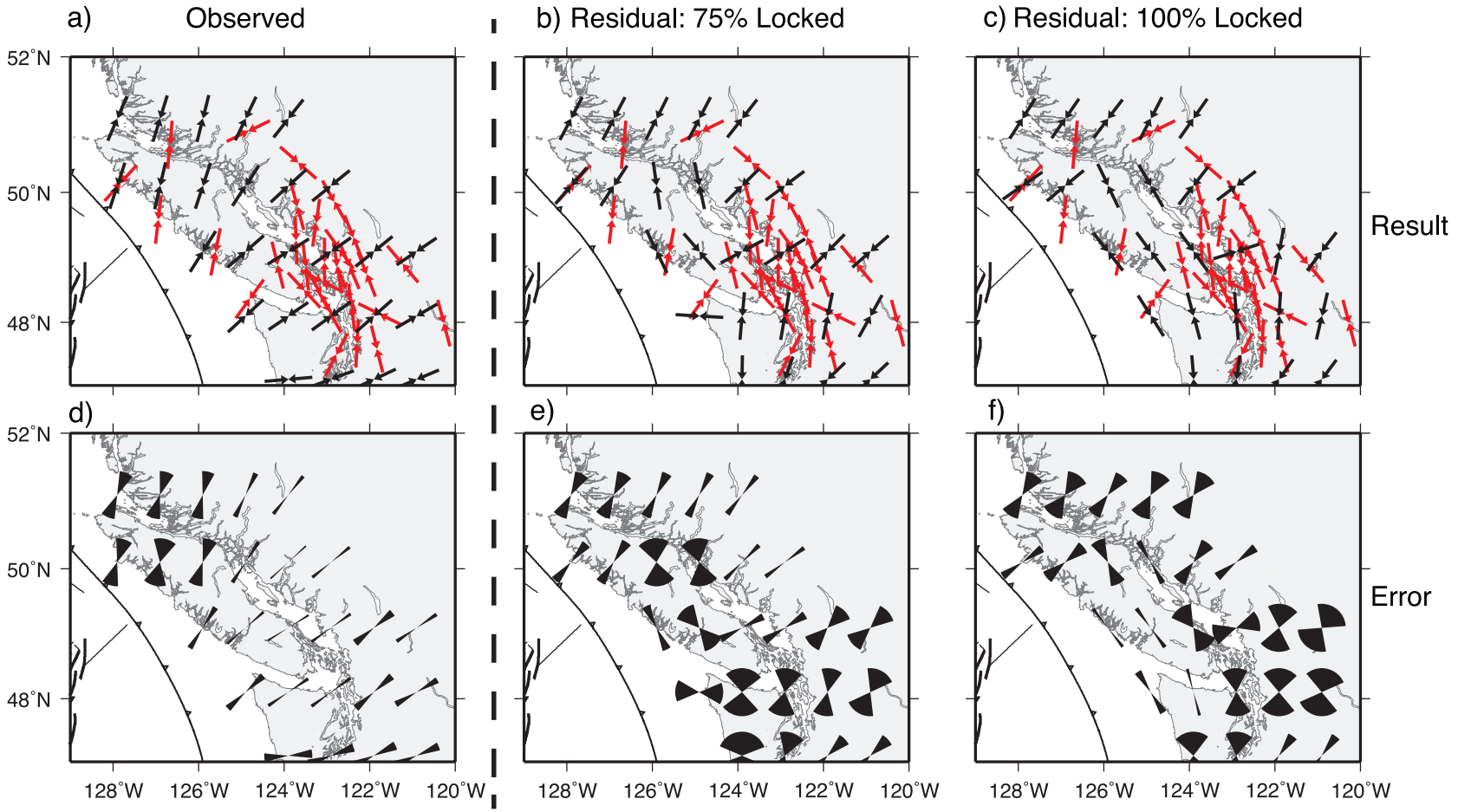

Figure 3.11: Comparison of S_{Hmax} (red arrows) with the e_{Hmax} direction from GPS strain rates (black arrows). GPS strain was calculated as the observed (a and d) and the residual (b, c, e and f), where the residual has the modelled subduction component removed. Two subduction models are shown with different amounts of locking on the subduction thrust; 75% (middle, b and e) and 100% (right, c and f).The lower plots show wedges representing the standard error of the e_{Hmax} in each case.

by Atwater (1987), Rogers (1988) and Dragert *et al.* (1994). Approximately 150 km inland, the stress results reflect the residual strain. The residual strain rate reflects the permanent crustal deformation caused by the northward push of the Oregon Block. The direction of this push rotates with the strike of the subduction zone to keep it approximately margin-parallel. Results from Ramachandran *et al.* (2006) show the presence of the mantle wedge separating the two plates approximately where the stress results change orientation. This implies that the change in orientation could be related to the lack of coupling between the plates. Figure 3.12 gives a cartoon representation of these two dominant forces. Studies investigating stress and strain at other subduction zones, such as the Nankai Trough, Japan Trench (Townend and Zoback, 2006) and the Peru-Chile Trench [Lavenu and Cembrano, (1999); Wang *et al.*, (2007)], also suggest that stress in the forearc reflects the residual deformation rather than that due to the subduction-earthquake cycle.

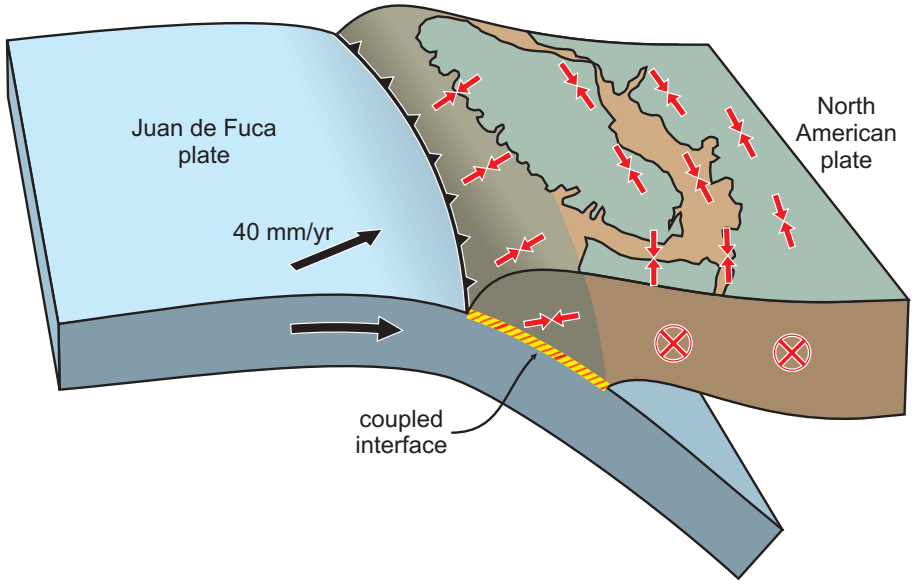

Figure 3.12: Cartoon representation of the dominant stress orientations (red arrows) in southwest British Columbia. The red crosses in circles represent motion into the page due to the northward push of the Oregon Block, which changes the stress orientation.

The faulting regime across the whole region is varied and does not reflect a single dominant style. Instead, there is a range of faulting styles which predominately include oblique thrust and strike slip faults. The variety in faulting styles may be due to: (1) the reactivation of old faults in an already highly fractured crust, and (2) similar magnitudes for the intermediate and least compressive stress. British Columbia is made up of five large accreted terranes with a northwest-southeast orientation. These terranes have a long history of deformation before accretion and are complicated internally by a mix of volcanic and metamorphic compositions. Faulting preferentially occurs on optimally oriented structures according to Anderson's theory of faulting (Anderson, 1951) and the Mohr-Coulomb failure criterion (Byerlee, 1978); however, existing structures that are not optimally oriented may also rupture if there are high pore fluid pressures and/or low friction strength. The variety of structures, including terrane boundaries, provide zones of weakness where these conditions may occur.

3.6 Conclusions

The computation of ∼600 focal mechanisms for crustal earthquakes in southwest British Columbia indicates a complex region of deformation with a range of faulting styles. Further analysis of the data shows that approximately equal amounts of 30% of faulting is strike-slip, thrust or some combination thereof, which only 10% of faulting is normal. Stress inversion results also show the stress regime favours strike-slip and thrust faulting.

Stress inversions for groups of focal mechanisms across the region reveal a change in S_{Hmax} with distance from the subduction margin. Groups close to the margin show

S_{Hmax} directions similar to e_{Hmax} likely due to the coupled plate interface of the underlying subduction zone as determined from earlier studies. Further inland from the margin the stress is related to the residual strain from the northward push of the Oregon Block. This change in stress reflects the change from a coupled interface to weakly coupled plates separated by a mantle wedge.

Chapter 4

Crustal Anisotropy in the Forarc of the Cascadia subduction zone, British Columbia

This paper aims to identify sources and variations of crustal anisotropy from shear-wave splitting measurements in the forearc of the northern Cascadia Subduction Zone of southwest British Columbia. Over 20 permanent stations and 15 temporary stations were available for shear-wave splitting analysis on ∼4500 event-station pairs for local crustal earthquakes. Results from shear-wave splitting show spatial variations in fast directions, with margin-parallel fast directions at most stations and margin-perpendicular fast directions at stations in the northeast of the region. Crustal anisotropy is often attributed to stress and has been interpreted as the fast direction being related to the orientation of the maximum horizontal compressive stress. However, studies have also shown anisotropy can be complicated by crustal structure. Southwest British Columbia is a complex region of crustal deformation and

some of the stations are located near large ancient faults. To use seismic anisotropy as a stress indicator requires identifying which stations are influenced by stress and which by structure. We determine the source of anisotropy at each station by comparing fast directions from shear-wave splitting results to the maximum horizontal compressive stress orientation determined from earthquake focal mechanism inversion. Most stations show agreement between the fast direction and the maximum horizontal compressive stress. These stations are further analyzed for temporal variations to lay groundwork for monitoring temporal changes in the stress over extended time periods. Determining the sources of variability in anisotropy can lead to a better understanding of the crustal structure and stress, and in the future may be used as a monitoring and mapping tool.

4.1 Introduction

4.1.1 Tectonics

The study region (Figure 4.1) includes the northern Cascadia Subduction Zone where the Juan de Fuca plate subducts at $\sim$40 mmyr^{-1} beneath the North American Plate (DeMets *et al.*, 1990; DeMets *et al.*, 1994). The region is made up of metamorphic and igneous terranes that have been accreted onto the North American Continent as the Juan de Fuca Plate subducts (Clowes *et al.*, 1987). Large faults, such as the San Juan Fault, mark boundaries between the terranes (Figure 4.2). This complex region of crustal structure can make investigating sources of crustal anisotropy difficult as anisotropy may reflect heterogeneity in the structure as well as the stress field.

There are two main plate driving forces that affect the stress and related deformation

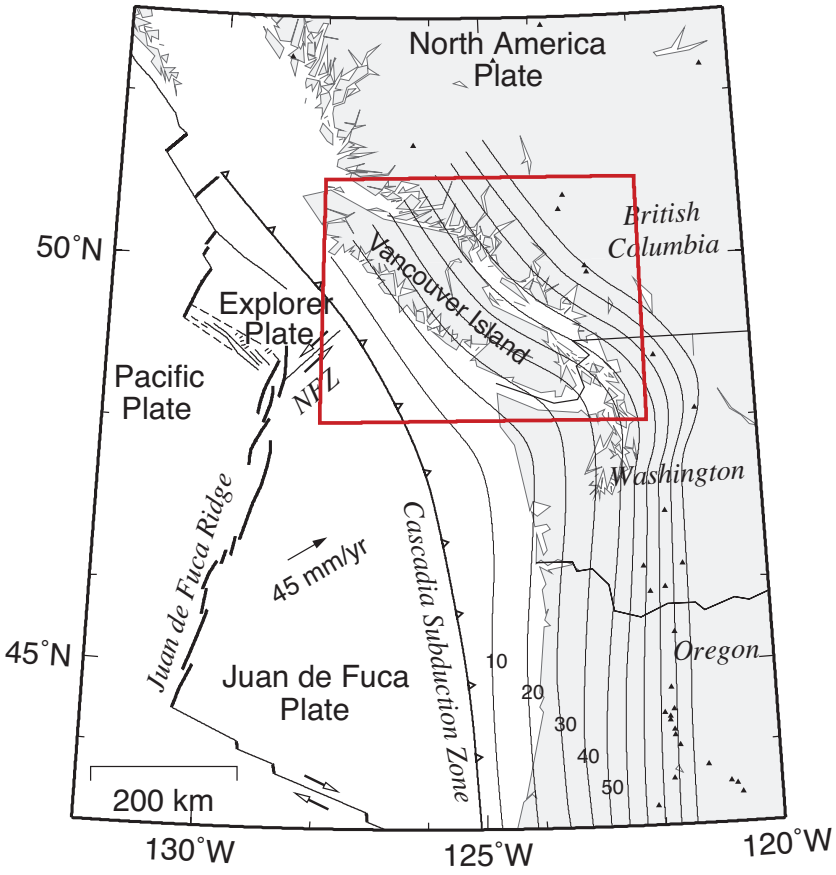

Figure 4.1: Northern Cascadia Subduction Zone. Contours show depth to the top of the subducting slab in kilometres (McCrory, 2004). Area outlined by the box is the region considered in this study.

of the crust in this region: 1) the ∼E–W compression due to the subduction of the Juan de Fuca Plate and 2) the northward push of the west coast of the United States due to the clockwise rotation of the Oregon block (McCaffrey *et al.*, 2000). Balfour *et al.* (2011) determined crustal stress from focal mechanism data and showed that earthquakes along the coast of Vancouver Island are the result of the short-term SW–NE stress accumulation from the compression related to the megathrust earthquake cycle, while earthquakes further inland from the coast are the result of the long-term northward push of the Oregon block.

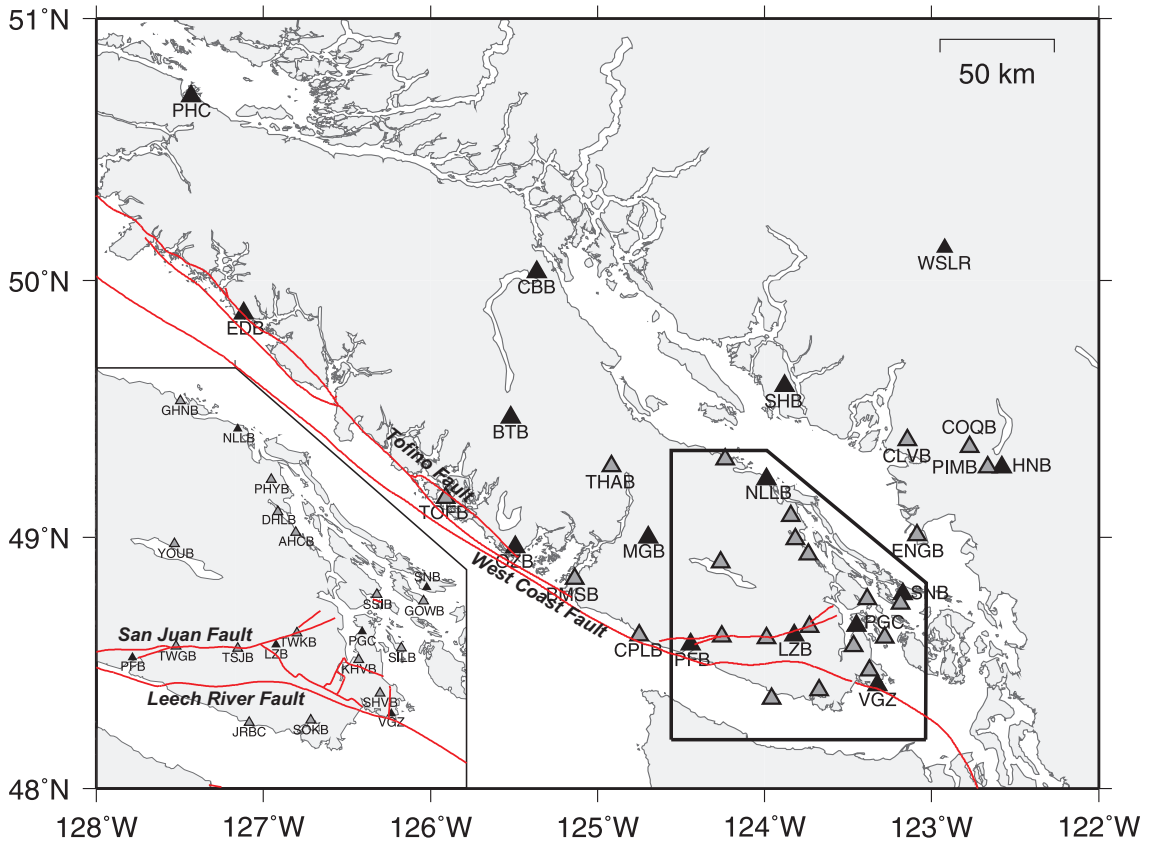

Figure 4.2: Station locations (triangles) and names used for this study. Stations in black are part of CNSN and those in grey are from temporary deployments.

4.1.2 Measuring Anisotropy

Anisotropy refers to a property of a medium that differs depending on orientation. Seismic anisotropy occurs when the wave velocity varies depending on the direction of propagation. Hexagonal anisotropy is a common form of anisotropy which occurs when a medium has only one axis of symmetry and the velocity varies depending on propagation direction. There are several mechanisms for hexagonal anisotropy in the crust, including: thin layers of alternating fast and slow material, small aligned cracks (Figure 4.3) and aligned minerals.

An S-wave is made up of two quasi-shear waves. In an isotropic medium these two

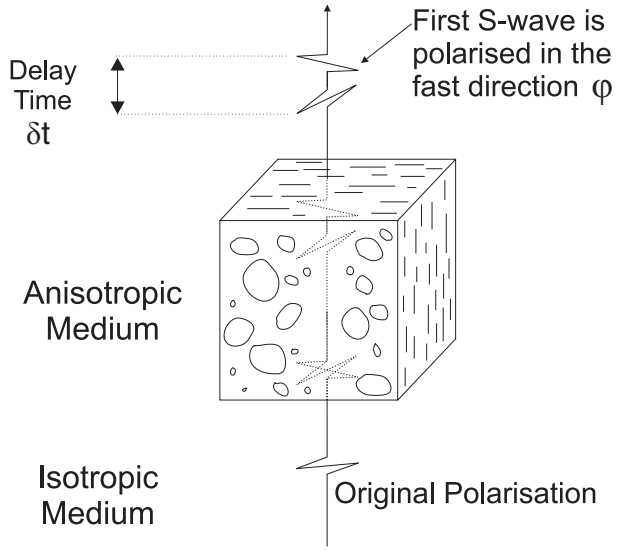

Figure 4.3: Illustration of shear-wave splitting through an anisotropic medium with a horizontal axis of symmetry. As a shear-wave enters an anisotropic medium it is split into two orthogonal components that travel at different velocities.

waves have the same velocity so arrive at the same time and appear as one pulse; however, in an anisotropic medium their velocity depends on their polarisation and propagation direction. If the S-wave is propagating in any direction other than along the axis of symmetry, then the S-wave component polarised parallel to the fast direction will travel faster than the orthogonal component. This phenomena is known as shear-wave splitting and it can be related to the anisotropy of the medium through which it travelled by measuring two parameters. Figure 4.3 shows the two parameters: (1) the polarisation of the fast shear-wave (fast direction, ϕ) and (2) the time difference between the fast and slow components of the shear-wave (delay time, δt).

4.1.3 Causes of Crustal Anisotropy

The cause of anisotropy in the crystalline crust is often difficult to identify due to complex structures. Mineral alignment such as foliation in schist and shearing in

fault zones is one possible cause for anisotropy (Balfour *et al.*, 2005; Boness and Zoback, 2006). Okaya *et al.* (1995) investigated anisotropy of the Haast Schist near the Alpine Fault zone, New Zealand, and found that at elevated pressures S-waves propagating parallel to the foliation travelled $\sim$1 kms^{-1} faster than waves propagating perpendicular to the foliation. This suggests that schist may contribute significantly to crustal anisotropy. Evidence from other metamorphic belts in Alaska, California and Vermont support this hypothesis (Godfrey *et al.*, 2000). Crustal anisotropy has also been linked with stress through the preferential alignment of fluid-filled cracks with the maximum compressive stress direction (Crampin, 1994). This hypothesis, known as extensive dilatancy anisotropy, suggests crack compliance such that only those cracks aligned with the maximum compressive stress direction will stay open, and, depending on the density of cracks, this can result in 1.5–10% differential shear-wave velocity anisotropy (Crampin, 1994). In many cases, however, distinguishing between stress-induced anisotropy and that due to mineral alignment in sheared fracture zones is difficult, especially if the direction of maximum compressive stress is subparallel to the plane of the fractures. Babuska and Cara (1991) suggest that the cause of anisotropy in the crust may vary with depth. In the upper crystalline crust, anisotropy may be due to micro-cracking and is stress related but in the lower crust anisotropy may be due to mineral alignment from sheared and metamorphosed rocks. Careful analysis of variations with depth of both fast direction and delay time can help resolve the location, source and extent of anisotropy in the crust.

4.1.4 Previous Studies

Previous studies of crustal anisotropy in British Columbia have shown that the majority of fast direction results from shear-wave splitting measurements follow the strike

of the subduction margin. Cassidy and Bostock (1996) measure S-wave splitting at station PGC near Sidney on Vancouver Island and show for shallow local earthquakes the fast direction is 293±27° with an average delay time of 0.2 seconds. They suggest from delay time results that seismic anisotropy is comparatively stronger in the upper 20 km of the crust compared with the lower crust. Currie *et al.* (2004) analyzed 16 more stations over the length of the Cascadia Subduction Zone, including British Columbia, Washington and Oregon. They suggest that crustal anisotropy is stress related as results in Oregon are in agreement with focal mechanism and borehole stress studies. However, at the time of their study there were very few stress results to compare with the fast directions in British Columbia where the fast direction appears to rotate towards the northwest.

4.2 Shear-wave Splitting

We use the Teanby *et al.*'s (2004) automated method that utilizes the Silver and Chan (1991) approach to analyze shear-waves for splitting. This method automatically defines many time windows around the shear-wave pick and then performs the Silver and Chan (1991) analysis on each window. The results are collated and clustering analysis is performed to determine the best result. The clustering analysis chooses the best cluster based on the overall cluster variance, which includes both the variance of the data within the cluster (i.e., cluster tightness), and the individual data variance. The chosen solution is the measurement with the lowest variance in the best cluster. The benefit of this approach is that it reduces the uncertainty in the stability of the result based on picking the shear-wave window.

Figure 4.4 illustrates the steps in the shear-wave splitting analysis. Each measurement

is manually checked and assigned a quality based on the following criteria:

(1). The energy on the component orthogonal to the incoming polarization direction that has been corrected for splitting is minimized (Figure 4.4b).

(2). The fast and slow waveforms are similar and correlated after correcting for splitting (Figure 4.4c,d).

(3). Particle motion is elliptical before and linear after the correction (Figure 4.4e,f).

(4). The error surface has a unique and well-defined solution, as unstable events often exhibit multiple lows (Figure 4.4g).

(5). The window plot exhibits a plateau containing many points with small error bars, with one point on the plateau corresponding to the final solution (Figure 4.4i).

There are several cases where shear-wave splitting will not occur. The first is if there is no anisotropy present. The second is when the incoming polarisation of the S-wave is parallel to either the fast or slow direction of anisotropy. The third is if the wave is propagating along the axis of symmetry. In the case where no splitting is measured there are two prominent fast directions with no resolvable delay time and the result is referred to a null.

Each event is given one of six grades, A, B, C, NULLA (where there is no defined delay time and there are two fast directions at 90° from each other), NULLB (when the delay times are not defined and there is one fast direction) and unusable (when there is no stable solution). An A quality result is one that fits all of the above criteria, while a B measurement fits a majority of the criteria and a C quality measurement does the same but is considerably more noisy.

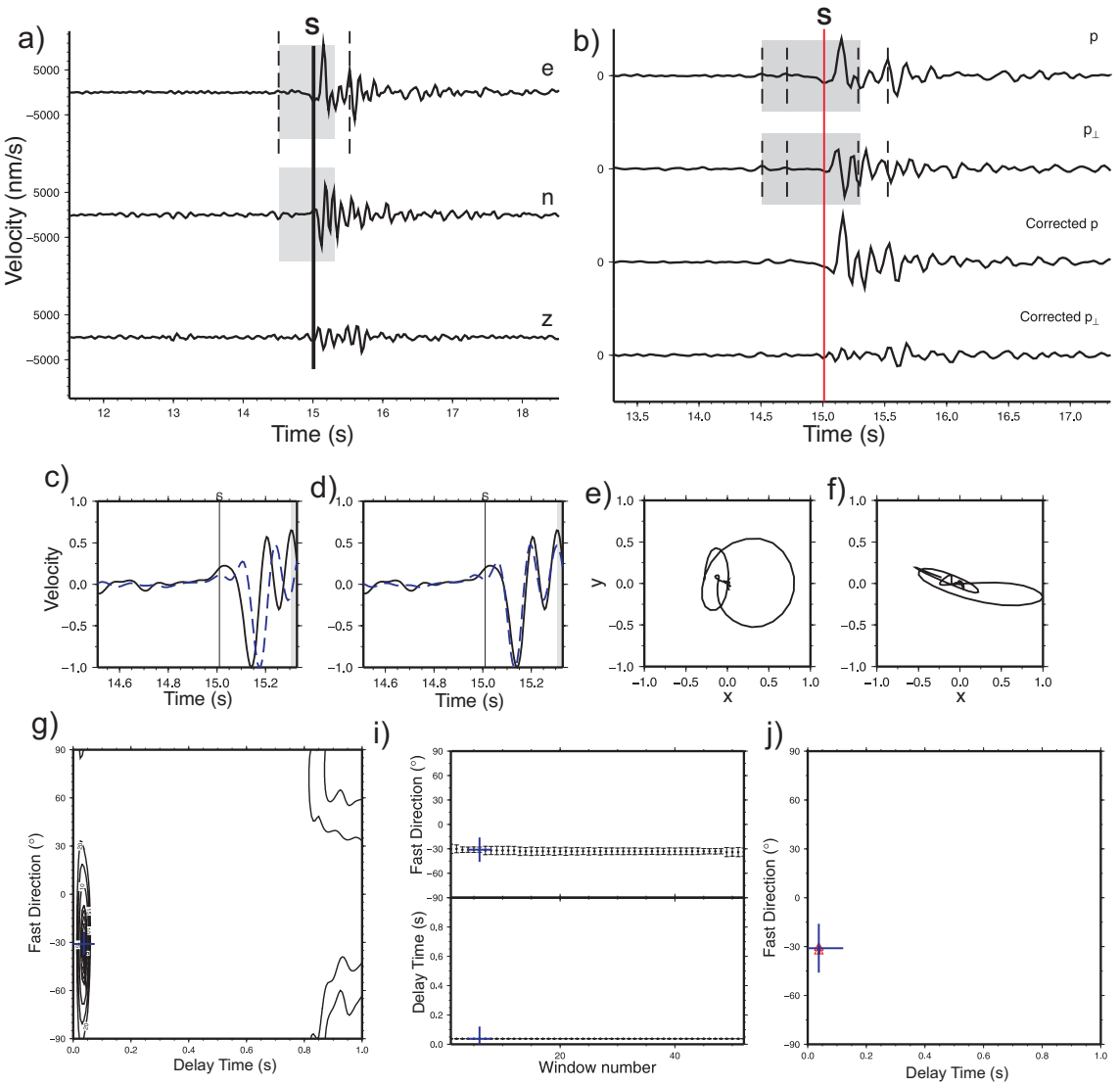

Figure 4.4: Diagnostic plots of shear-wave splitting analysis from an A quality measurement. In (a) S is the picked shear-wave arrival and the dashed lines indicate the start and finish of the window in which the analysis was performed. The original east (e), north (n), and vertical (z) components in (a) are rotated into components parallel (p) and perpendicular to the source polarisation and corrected for splitting, as shown in (b). The fast (solid) and slow (dashed) component of the shear-wave before and after splitting are shown in (c) and (d) along with the associated particle motion in (e) and (f). The error surface is shown in (g), where the closest contour to the solution is the 95% confidence region. The final two plots show results from all the windows in which shear-wave splitting analysis was performed: (i) show the individual solution and associated uncertainty for each window and (j) shows the clusters (triangles) of the solutions. The best solution is indicated by a cross in both plots.

4.2.1 Data

Earthquake recordings are selected for shear-wave splitting using three important criteria. The first criterion is hypocentre depth; since the objective is study crustal anisotropy it is important consider earthquakes whose rays travel mostly through the crust. For this study we initially look at earthquakes with depths <50 km, but expand this to include earthquakes located in the uppermost subducting plate if the shear-wave splitting results are similar to those from crustal earthquakes or if there are few suitable crustal earthquakes to analyze (Figure 4.5). The second criterion is the S-wave window, which is defined to include incidence angles $< 45^{\circ}$ to avoid scatter and converted phases (Nuttli, 1961; Evans, 1984). The third criterion is signal-to-noise ratio, to remove any poor quality data.

Stations on Vancouver Island and Southwest British Columbia that were used to investigate anisotropy are from the Canadian National Seismic Network (CNSN) and a temporary array of POLARIS stations (Figure 4.2). These stations span a range of time periods from several months to more than a decade and are all three-component broadband seismometers. Earthquake locations were obtained from the CNSN catalogue along with the initial shear-wave picks. To maintain consistency all S-wave picks were reviewed before shear-wave splitting analysis.

4.3 Results

Shear-waves from ∼4500 event-station pairs were analyzed for shear-wave splitting; from these ∼1100 gave good results, ∼1800 produced nulls and ∼1500 were unusable. We are able to define the fast direction of crustal anisotropy beneath 30 stations.

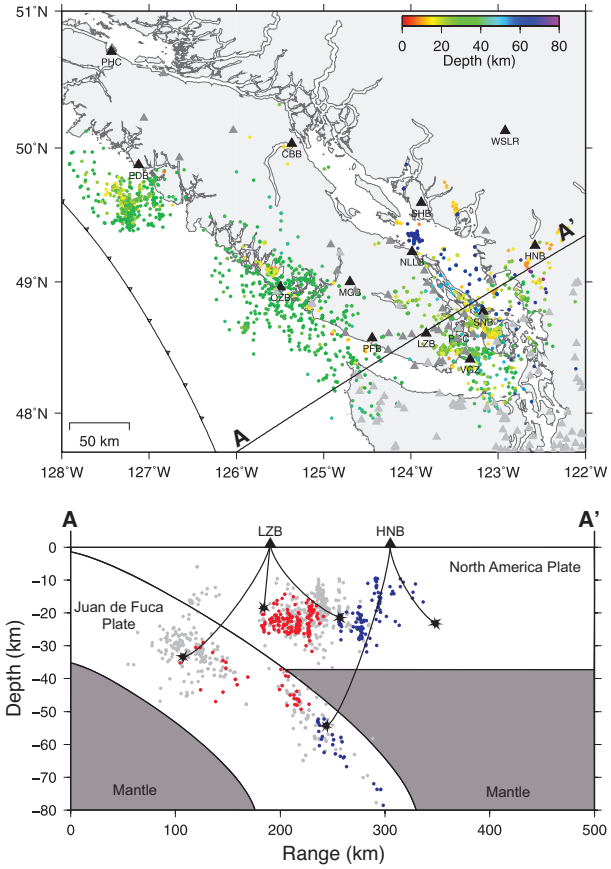

Figure 4.5: Map and cross-section of earthquakes used for shear-wave splitting analysis at labelled stations. In the cross-section, red and blue earthquakes were recorded at stations LZB and HNB respectively. Grey circles on the cross-section indicate earthquakes used for shear-wave splitting at other stations labelled on the map.

4.3.1 Spatial Variation in Fast Direction

Fast direction results and statistics from each station are shown in Figure 4.6 as rose diagrams. Fast directions observed at stations on southern Vancouver Island and along the west coast are oriented NW–SE, parallel to the strike of the subduction margin. Within this group of stations a few (JRBC, SOKB and TSJB) show more E–W orientations similar to the strike of the faults in the region (Figure 4.6). Stations further east and north indicate fast directions that are oriented NE–SW, almost perpendicular to the first group.

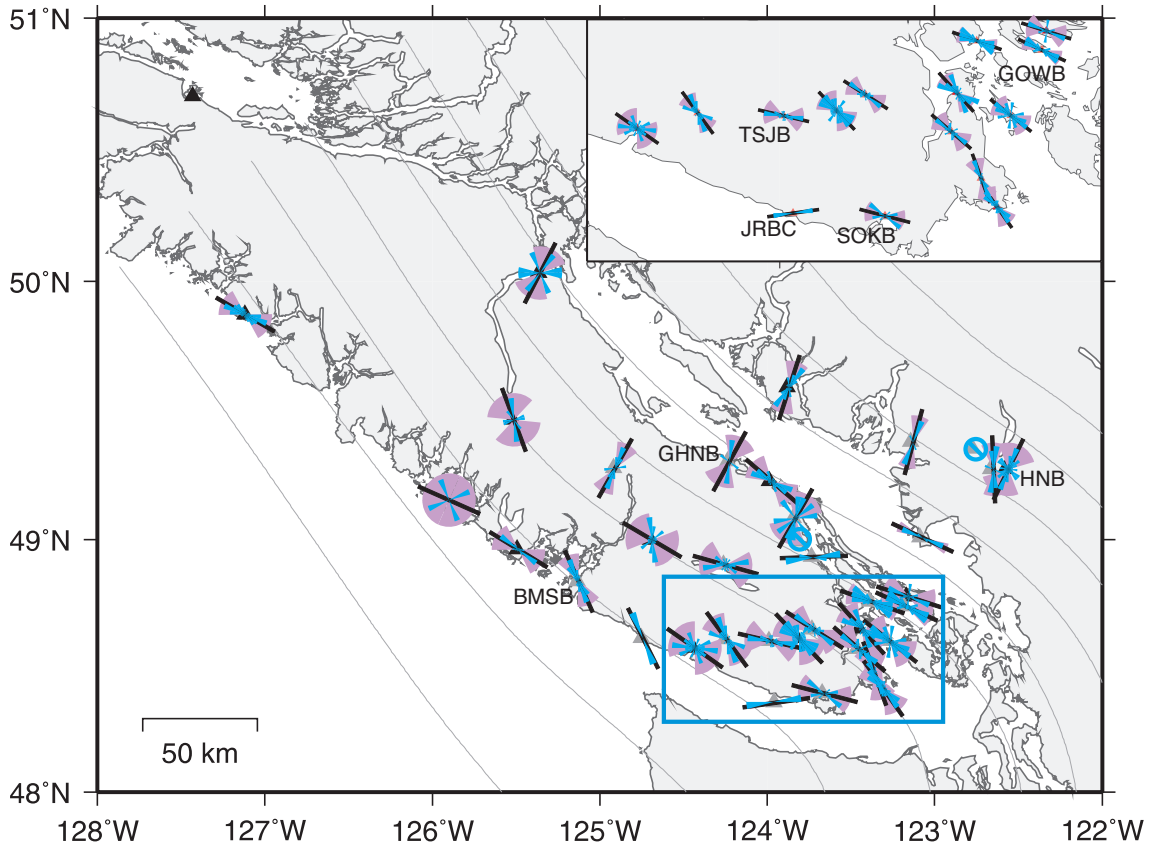

Figure 4.6: Shear-wave splitting results from local S phases. The fast directions determined from events recorded at each station are represented as rose diagrams shown in blue. Black lines indicate the mean fast direction, with standard deviation indicated by the purple wedges. The inset is a zoom of the results observed at southern Vancouver Island stations, as outlined by the box.

Fast direction results with back-azimuth and incidence angle are plotted to identify variations (example in Figure 4.7). This is important as we included events with take-off angles up to 45°. Results between 35–45° should be used with caution as the shear-wave may be affected by the free surface (Nuttli, 1961; Evans, 1984) or be the result of a combination of transverse isotropy and azimuthal anisotropy (Paulssen, 2004). Although many stations show some variation in the fast direction, there appears to be no systematic variation with back-azimuth or incidence angle.

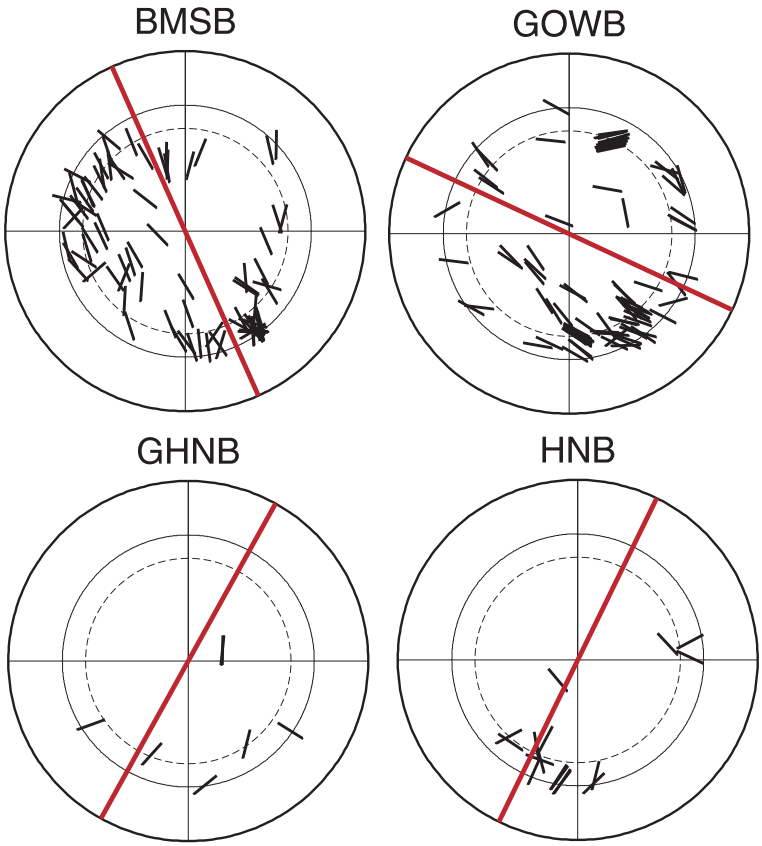

Figure 4.7: Circle plots of fast direction with back-azimuth and incidence angle. The red lines are the mean fast direction. The inner solid circle shows the extent of the shear-wave window used (45°) and the dashed circle shows the 35° window. These stations were chosen as an example of the two dominant fast directions: NW–SE fast directions along the coast and southern Vancouver Island (upper plots) and NE–SW further inland (lower plots).

4.3.2 Depth Variation in Delay Times

Shear-wave splitting delay times range from 0.05 to 0.4 s, with an mean of 0.1±0.07 s over all stations. Figure 4.8 (top) shows variations of delay time with depth. Overall, delay times show significant scatter with no obvious increase with depth, which suggests the anisotropy measured from shear-wave splitting is in the upper crust. Normalised delay times (Figure 4.8, bottom) plotted with depth show the highest normalised delay times in the top 10-20 km. These observations are in agreement

with results from Cassidy and Bostock (1996) who suggest anisotropy is strongest in the upper 20 km of the crust.

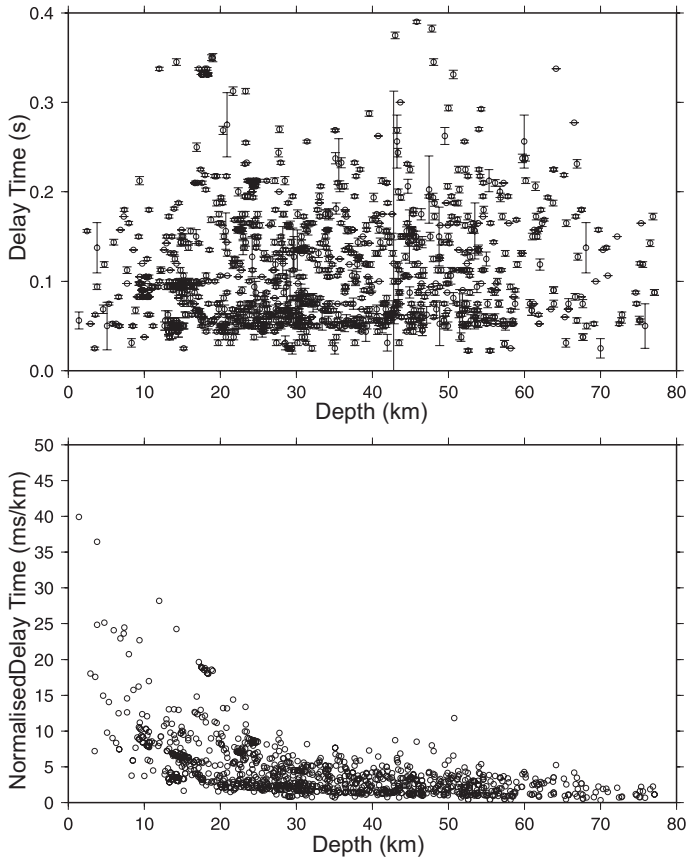

Figure 4.8: Delay time with the 2σ error (top) and normalised delay time (bottom) results with depth. Normalised delay times are computed by dividing the delay time (ms) by the depth (km). They show that normalised delay times are large at shallow depths.

Beneath some stations, earthquakes located in the top of the Juan de Fuca Plate were analyzed. Comparison of the shear-wave splitting results from these events with the shallower events show little difference in delay times. Therefore, we can assume that anisotropy in the crust must be a strong influence and either there is little anisotropy in the upper part of the subducting plate and mantle wedge or crustal anisotropy is far stronger and dominates shear-wave splitting. There are some exceptions: stations SHB, HNB, PGC and SHVB (Figure 4.2) show a small increase in delay time between

the crust and slab events of ∼0.05 s. These stations are located in the eastern part of the study area and have 10–40 km of mantle wedge between the two plates, which may influence the delay times (discussed in more detail, below).

4.4 Discussion

Interpretation of the source of anisotropy and causes of variation in shear-wave splitting parameters is complex and often debated, as described by Crampin and Peacock (2008). Southwest British Columbia is no exception; however, we attempt to determine which stations show stress-related anisotropy. In the future these stations could be candidates for monitoring variations in stress that may be related to large earthquakes or slow-slip events.

4.4.1 Comparison with Stress

We use stress results from Balfour *et al.* (2011) to compare with fast directions from shear-wave splitting. The stress results were determined by performing Bayesian inversion on each of 34 groups of focal mechanisms (∼600 individual focal mechanisms) to calculate three principal stress directions, stress ratio and the maximum horizontal compressive stress direction (S_{Hmax}). S_{Hmax} directions vary over the region as shown in Figure 4.9. Along the coastline of Vancouver Island, nearest to the subduction margin, S_{Hmax} is margin perpendicular due to the compression from the locked plate interface. Over the rest of the region, S_{Hmax} is margin parallel, likely due to the northward push of the Oregon block (McCaffrey *et al.*, 2000) and a weakly coupled subduction fault resulting in a low-stress forearc (Wang, 1996).

Figure 4.9 compares the S_{Hmax} directions with the fast direction of anisotropy. There is agreement between S_{Hmax} and the fast direction at most stations located in the southern part of Vancouver Island and on the mainland of British Columbia near Vancouver. We interpret these stations as having stress-related anisotropy due to fluid-filled microcracks. The rest of the stations are more complicated and show a disagreement between S_{Hmax} and the fast direction. This does not rule out stress-related anisotropy but suggests there is either a more complicated relationship with the stress or an influence from structures, such as rock fabrics.

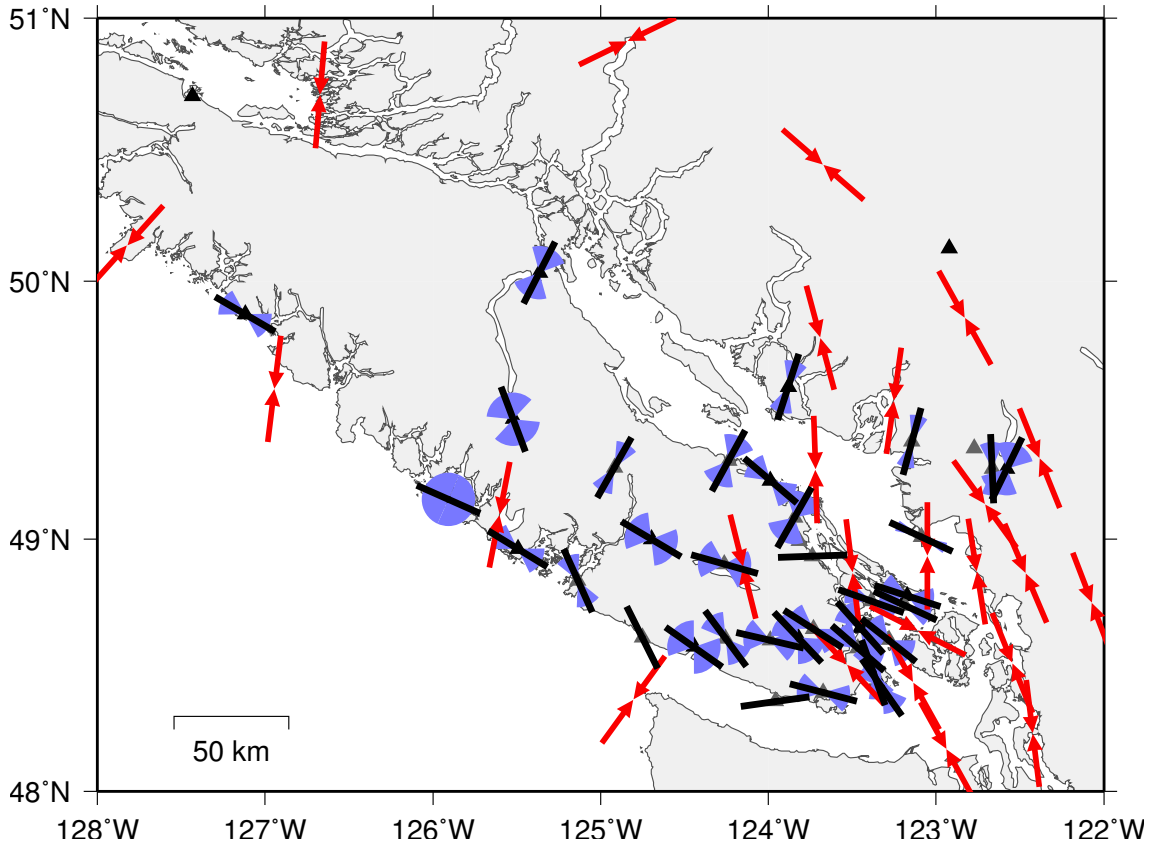

Figure 4.9: Comparison of fast direction results and S_{Hmax} directions (red arrows) from focal mechanism inversion (Balfour, 2011). The black lines and light blue wedges show the mean and standard deviation respectively in the fast direction observed at each station.

There are several interpretations that may explain the discrepancies between fast

direction and S_{Hmax} for this study region:

(1). The fast direction is related to crustal structure, such as rock fabrics formed by metamorphism or fractures and shearing during faulting.

(2). The fast direction is related to anisotropy in the subducting slab or mantle wedge.

(3). The fast direction is related to the transient stress due to the locked subduction but is influenced by high pore fluid pressures that results in a 90° flip in fast directions.

(4). The fast direction reflects the non-recoverable margin-parallel deformation due to a low-stress forearc and the northern push of the Oregon Block.

We will address each of these interpretations to determine what is the most likely source of anisotropy at each of the stations where the fast direction if differs from the S_{Hmax} direction. We divided the region into three groups based on the dominant fast direction and whether the fast direction agrees with the stress (Figure 4.10).

Mainland and Southern Island Stations

The Mainland and Southern Island group of stations (Figure 4.10) has been discussed in section 4.4.1 and represents the relatively simple case where the fast direction of anisotropy is similar to the S_{Hmax} direction and can be explained by extensive dilatancy anisotropy as defined by Crampin (1994).

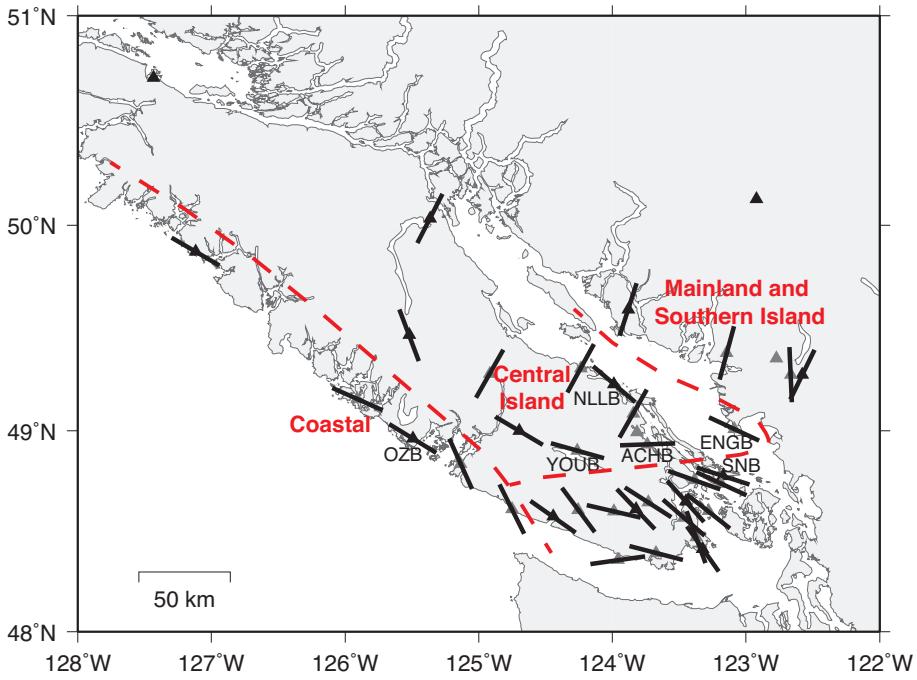

Figure 4.10: Regions discussed in the interpretation of the source of anisotropy. Stations specifically mentioned in the text are labelled.

Coastal Stations

The Coastal group (Figure 4.10) is characterized by fast directions rotated ~80° relative to the S_{Hmax} direction. All four of the interpretations listed above could be applied this group; however some are supported more strongly than others. The first interpretation we consider is that anisotropy is related to crustal structure. Crustal structure of the subduction zone beneath Vancouver Island has been investigated through studies of seismic reflection and refraction profiles during the LITHOPROBE project (Clowes *et al.*, 1987). One of the main features identified from this project which could influence anisotropy is the E-layer. This layer is located just above the subducting Juan de Fuca Plate and has been interpreted in several ways, including: (1) as a layer of imbricated sediment cover (Clowes *et al.*, 1987), (2) as a shear zone in the lower crust (Calvert and Clowes, 1990), and (3) as the top of the Juan de Fuca

crust (Nicholson *et al.*, 2005). Clowes *et al.* (1987) suggest the sediment grain of this layer dips to the NE, parallel to the plate motion, which is almost perpendicular to the fast directions observed in this study and therefore cannot explain the margin-parallel fast directions. Another influence on the fast direction could be the Tofino Fault or West Coast Fault, which are located just offshore of the west coast of Vancouver Island (Figure 4.2). These are thrust faults that strike NW approximately parallel to the fast direction observed at coastal stations. There is little evidence that these thrust faults have a significant component of strike-slip motion (Clowes *et al.*, 1987), hence they are unlikely to cause the NW fast directions we observe.

The second interpretation is that the observed anisotropy is from the subducting slab and not the crust. Many of the earthquakes used for shear-wave splitting analysis for stations along the coast are located in the top of the subducting slab and therefore a small portion (up to 10 km) of the ray path is through the slab. Wada *et al.* (2010) investigated intraslab stresses in the Juan de Fuca slab and found that the slab beneath Vancouver Island is under slab-normal compression with the least compressive stress being down the dip of the slab and suggesting slab-pull related forces. If we consider these stresses in the horizontal, then the least compressive stress is margin perpendicular and the intermediate compressive stress (the maximum horizontal compressive stress) is margin parallel, which would be in agreement with our observations and related to stress in the subducting slab. However, at station OZB, $\sim$100 shear-wave splitting results from earthquakes in the crust have the same margin-parallel fast direction as observed for events in the slab (Figure 4.11). From these results, we can assume there is no influence from the slab.

The third interpretation is that anisotropy is related to the transient stress, due to the locked subduction fault, but is affected by high pore fluid pressures. Zatsepin and

Crampin (1997) discuss how high pore fluid pressures may cause fast directions to become orthogonal to the S_{Hmax} direction. These 90°-flips have been observed at a fractured reservoir during fluid injection (Angerer *et al.*, 2002) and above seismically active faults (Crampin *et al.*, 2002; Padhy and Crampin, 2006). The closest estimates of pore fluid pressures are from seismic profiles offshore of the west coast Vancouver Island which image the accretionary wedge. Hyndman *et al.* (1993) estimate that pore fluid pressures reach 80% of lithostatic pressure approximately 100 km offshore. The 90°-flips observed in previously mentioned studies occur between nearby stations or over time. The coastal stations are similar to neighbouring stations and do not show any significant changes in fast direction with time, which implies that if high pore fluid pressures are present they would have to extend over 300 km along the coast.

The last interpretation is that anisotropy is related to the non-recoverable, long-term, margin-parallel stress that is observed over the rest of the region and not due to the transient stress from the locked subduction thrust. This interpretation implies that the stress inversions from focal mechanisms and the shear-wave splitting observations are measuring different sources of stress. The stress orientation is determined by inverting a group of focal mechanisms and is a measure of the in-situ stress for that volume. For example, the focal mechanisms inverted for the stress result closest to OZB are all located between 10-20 km depth and on average ∼8 km above the plate interface. Therefore, the stress in the crust between 10-20 km is influenced by the locked subduction interface. The majority of the crustal earthquakes we use for shear-wave splitting analysis at OZB also originate at 10–20 km depth; however, shear-wave splitting is a measure of anisotropy along the path between the source and station and reflects the entire travel path, not just the source region at depth. We suggest that the stress from the locked subduction thrust decays towards the surface,

especially if the plates are only weakly coupled as suggested by (Wang, 1996). In the upper 10 km, the stress from the locked subduction thrust is almost negligible and the margin-parallel stress dominates. This interpretation requires the main source of anisotropy to be in the upper 10 km of the crust as is often observed (Kaneshima *et al.*, 1988).

Central Stations

Most of these stations do not agree with the observed stress (Balfour *et al.*, 2011) and are not located along the coast. Stress results at stations ACHB, ENGB, NLLB and YOUB differ considerably from the S_{Hmax} direction and the fast direction observed at nearby stations (Figures 4.9 and 4.10). Station ACHB has an E-W fast direction but has only three observations. More observations are need to determine whether these reflect the actual anisotropy or if they are outliers. At station NLLB the fast direction differs by $\sim$80° from the two neighbouring stations. Considering the depth distribution of events used for shear-wave splitting at the three stations we note that the majority of events used at NLLB are in the top of the slab between 50–70 km depth, while at neighbouring stations (GHNB, PHYB) the events are mostly in the crust. The fast direction observed at NLLB appears to be strongly influenced by the portion of the path ($\sim$40%) that travels through the top of the slab and mantle wedge. This interpretation can also be applied to YOUB as shear-wave splitting on slab earthquakes produces fast directions margin-parallel and the crustal earthquakes are more variable with some results parallel to S_{Hmax}. Station ENGB has a $\sim$70° discrepancy between the fast direction and S_{Hmax}. This station differs from others as it is located on the Fraser River Delta with $\sim$800 m of soft sediment (Britton *et al.*, 1995). ENGB also has the most consistent shear-wave splitting parameters,

with only 12° standard deviation of the fast direction. We believe that the thick sediment cover may influence the fast direction of shear-wave splitting. It seems unlikely that the fast direction is related to a 90°-flip due to high pore fluid pressures as fluid pressures on the Delta may be influenced by tides and seasonal variations (Ricketts, 1998). If the fast direction is influenced by changes in pore fluid pressures we would expect to see changes in fast direction or delay time with time (Angerer *et al.*, 2002; Crampin *et al.*, 2002).

4.4.2 Temporal Variations

Temporal variations in both fast direction and delay time have been observed in shear-wave splitting results from areas undergoing stress changes. Gerst and Savage (2004) observed changes in fast directions before and after an eruption on Mt Ruapehu, New Zealand, in 1995 and attributed this to a change in stress due to injection of magma into a dyke beneath the volcano. Variations in time delays have been observed by Crampin *et al.* (2008) before and after $M_L > 5$ earthquakes due to changes in crack aspect-ratios of fluid-filled microcracks from perturbations in stress.

Earthquakes and Swarms at OZB

We look at temporal variations in delay time and fast direction at station OZB, which has one of the longest records of shear-wave splitting results. There was also a M_L 5 earthquake ∼40 km from the station which may have induced changes in crustal stress. Before analyzing the results we separate them into two groups based on bands described by Crampin and Peacock (2008). Bands are based on the angle between the propagation direction of the incoming wave and the crack plane. Results are consid-

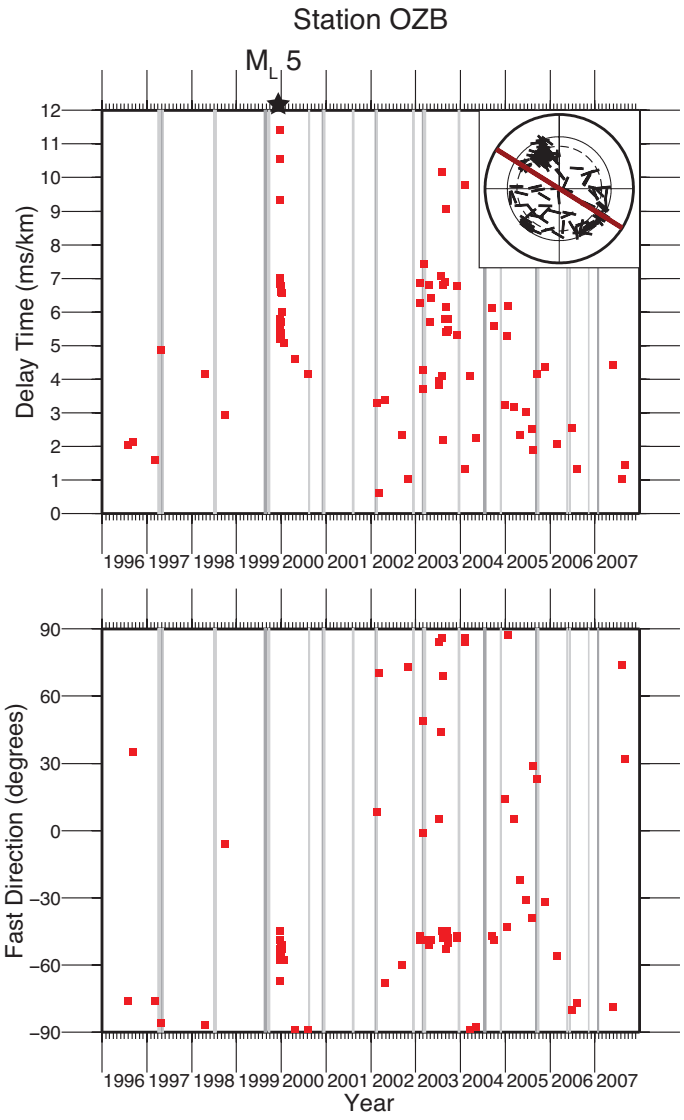

Figure 4.11: Variations in normalised delay time (top) and fast direction (bottom) from results in band 1 observed at station OZB. Delay times from band 1 events are sensitive to changes in crack aspect-ratios and are more likely to be influenced by temporal changes in stress. The spike in delay times in band 1 are associated with aftershocks of a M_L 5 event within 50 km of the station. Dark and light grey stripes show southern- and mid-Vancouver Island ETS events respectively.

ered to be within band 1 if the difference between their propagation direction and the crack plane is <15°, otherwise, the result is between 15° and 45° and within band 2. Crampin and Peacock (2008) suggests that delay times from results within band 1 are sensitive to the crack aspect ratio and could be less than the "background" average

delay time before a large earthquake, when there is increased stress, or may increase just after due to stress release. They also describe that band 2 is more sensitive to crack density and is less likely to be affected by stress changes from earthquakes. We assume stress-related anisotropy and therefore the crack plane is parallel to the S_{Hmax} direction. We use S_{Hmax} directions which were previously calculated from inverting focal mechanism data. Figure 4.11 shows delay times normalized with depth for results within band 1 at station OZB. Although the results appear quite scattered with time there is a distinct peak during early 2000. The peak is related to the aftershocks of a M_L 5 earthquake on December 25th, 1999, and show an increase in delay time after the event in agreement with observations from Crampin *et al.* (2008). Unfortunately, the closest result in time prior to the earthquake was over a year earlier and therefore we can not determine if there was a decrease in delay time before the event. The other time window with delay times above 9 ms/km is during a period of increased activity that occurred during August and September of 2003. It is possible this increase could also be due to a change in crack ratio associated with stress release from both the largest event and subsequent events, however in this case the main event was only M_L 2.5.

Episodic Tremor and Slip

We also look for variations in splitting parameters that may be associated with episodic tremor and slip (ETS) events at stations OZB and SNB. At OZB (Figure 4.11), there is no obvious systematic variation of delay time or fast direction with ETS events. However, it could be argued that there is a decrease in delay time before and an increase in delay time after the 1997, 1999 and late 2002/2003 events. At SNB (Figure 4.12), some fast direction results are rotated $\sim$90° to the average fast

direction ($-72\pm35°$). These rotated fast direction observations appear to occur near periods of ETS or around the time of earthquakes $M_L > 3$. Station OZB is on the western edge and SNB is on the eastern edge of the region where ETS occurs and may respond differently to associated stress changes. Observations at more stations before, during and after ETS events are needed to determine whether these events cause a change in shear-wave splitting parameters.

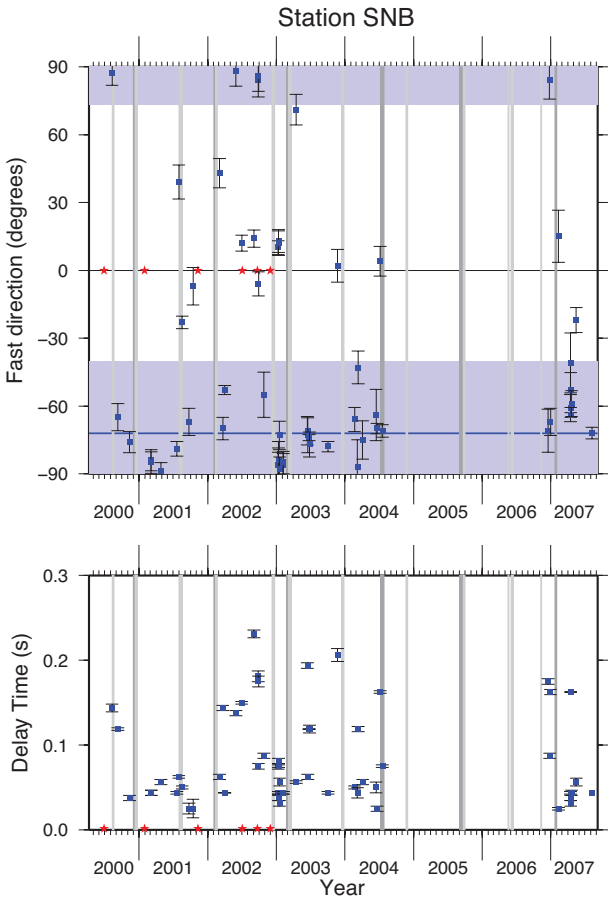

Figure 4.12: Variations in fast direction (bottom) and normalised delay time (top) from results in band 1 observed at station SNB. Bands are defined and explained by Crampin (2008a). Delay times from band 1 events are sensitive to changes in crack aspect-ratios and are more likely to pick up temporal changes in stress. The stars indicate when earthquakes over magnitude 3 occur. Dark and light bands show southern- and mid-Vancouver Island ETS events respectively.

4.5 Conclusions

We analyze ∼4500 event-station pairs for shear-wave splitting above local earthquakes to determine the anisotropy in the crust. The fast direction from the majority of stations align with the S_{Hmax} direction and have small delay times of 0.1±0.07 seconds. The similarity between fast direction and S_{Hmax} implies that anisotropy its caused by stress-aligned fluid-filled microcracks, in agreement with other studies of crustal anisotropy. Along the west coast of Vancouver Island the S_{Hmax} direction changes to margin-perpendicular due to the influence of the locked subduction interface but we do not observe a similar change in the fast directions. We attribute this discrepancy to the two sets of observations sampling different regions in the crust. The focal mechanisms used in the stress inversion sample a region of the crust at 10–20 km depth which is likely influenced by the subduction thrust. The shear-wave splitting measures anisotropy of the uppermost 10 km and may reflect the long-term margin-parallel stress due to the low-stress forearc and the rotation of the Oregon Block.

Most stations have some scatter in fast direction with time but show little systematic variation. We observe some evidence for delay time variation at station OZB associated with a M_L 5 earthquake and possible changes at station SNB associated with ETS, although more data are needed for conclusive results.

Chapter 5

Summary

The objective of this thesis is to gain a better understanding of the processes that result in earthquakes in the North American crust of the northern Cascadia Subduction Zone. Three questions were designed to address the objective: Where can large earthquakes occur? What forces influence faulting? And can we monitor these forces using crustal anisotropy? We answer these questions by combining several different aspects of seismology, including: seismicity patterns, focal mechanism determination and stress inversions, and crustal anisotropy from shear-wave splitting. Below is a summary of what was learned from exploring each of these questions and how the findings contribute to a better understanding of faulting in the crust.

5.1 Where do large earthquakes occur?

Historical records show that British Columbia experiences large crustal earthquakes up to magnitude 7.3 in the North American crust, but it is difficult to determine on

what structures these events occurred and where they might occur next. We used precise earthquake relocation methods to identify structures and determine whether earthquakes occur on faults that can be traced on the surface or if they occur on "hidden" structures within the crust. We relocated earthquakes beneath the Fraser River Valley, British Columbia, and the San Juan Islands, Washington, using catalogue and waveform differential arrival times. Relocated earthquakes illuminated an active structure beneath the San Juan Islands and streaks of seismicity in the Fraser River Valley.

The San Juan Island structure strikes ∼290° and dips northward at an angle of ∼60°. Many focal mechanism nodal planes also support an east-west striking fault with a steep dip. This fault strike is similar to other faults in the region, such as the Devils Mountain and Tacoma Faults in Washington State (Johnson *et al.*, 2001; Sherrod *et al.*, 2004) and the Georgia Strait structure in British Columbia (Cassidy *et al.*, 2000). Seismicity is concentrated between 10–20 km depth and extends ∼10–15 km along strike. The strike of structure is similar recently mapped surface faults north and south of the San Juna Islands. The age of these mapped faults is difficult to determine from multibeam bathymetry and seismic reflection data due to the dynamic environment of the ocean floor and lack of sediment cover (personal. comm. Vaughn Barrie). There is also a lack of shallow seismicity (<10 km) along the structure, which might suggest that the upper 10 km of the fault is locked or creeping. If this portion of the fault ruptured (assuming a rupture area of 100 km^2 and a slip of 1 m) it would result in an earthquake of similar magnitude to those that occurred in 1909 (M 6.0) and 1920 (M 5.5). An earthquake on this structure would be less hazardous if the rupture is confined to only a patch on the fault (25 km^2) similar to the patches of seismicity observed in earthquake relocations.

Seismicity in the Fraser River Valley of British Columbia is less well defined but includes several narrow streaks of seismicity that extend from the surface to ∼20 km depth. Similar streaks have been observed near the San Andreas fault and attributed to changes in rheology or stress concentrations between locked and creeping portions of the fault (Waldhauser *et al.*, 2004). The Kendall fault scarp associated with the Boulder Creek fault is the closest fault known to be active (Barnett, 2007). The relocation results fail to reveal any lineations in the seismicity that could be associated with the Boulder Creek fault, although there is high seismicity in the mid-lower crust. The strike of these surface faults are similar to the orientation of the lineations and might suggest these seismicity streaks occur along pre-existing planes of weakness similar to the surface faults but at depth in the crust. Mapping faults on the Fraser River delta is difficult due to the thick sediment cover and the dense urban environment. Seismic reflection studies have found little evidence for disrupted sediments that might indicate faulting on the Fraser River Delta. This might be due to processes within the loosely consolidated delta sediments that do not preserve features related to faulting.

We used various velocity models for our relocations and observed that more detailed models reduced the vertical errors in the relocations and removed artifacts caused by large contrasts at velocity layer boundaries. On average, errors in catalogue locations are 1000 m in the horizontal and 2000 m in the vertical; however, relocating events using catalogue data alone the error reduces by at least a factor of 2. This is improved even further if both cross-correlation and catalogue data is used, reducing the relative error to ∼100 m in the horizontal and ∼200 m in the vertical.

Earthquake relocation results show that faulting in the crust occurs on small structures and in larger clusters. Focussing on small structures we found that some may

be associated with surface expressions of faults. Seismicity on these structures tends to occur in patches, and if events over a longer period of time are studied, more patches might be found which could further constrain dimensions of the structure. The inclusion of cross-correlation data was vital to the correct interpretation of the San Juan Island structure since with catalogue data along the structure could easily be interpreted as two east-dipping faults as opposed to three clusters that align on one northward dipping structure. In the future, it would be beneficial to incorporate more cross-correlation data, especially if a specific structure is being investigated.

5.2 What forces influence faulting?

To determine what forces influence faulting we investigated the regional stress by computing ∼600 focal mechanisms for the principal stress orientations and the stress ratio. We investigated how stress varies over the region by dividing the data into 34 groups before performing the inversion. These focal mechanisms were added to the database, resulting in ∼1000 focal mechanisms for crustal earthquakes ($M_L > 1$) for the period of 1975–2009. Focal mechanisms show there are a range of faulting styles which include predominately oblique thrust and strike slip earthquakes. The variety in faulting styles may be due to: (1) the reactivation of old faults in an already highly fractured crust, and (2) similar magnitudes for the intermediate and least compressive stress.

Most stress results support a oblique thrust faulting regime where the maximum compressive stress is horizontal and the intermediate and least compressive stresses are sub-horizontal and sub-vertical respectively. We calculate the maximum horizontal compressive stress (S_{Hmax}) and use it to investigate spatial variations. Bayesian

stress inversions for groups of focal mechanisms across the region reveal a change in S_{Hmax} with distance from the subduction margin. Along the coast S_{Hmax} is almost margin perpendicular while further inland the direction changes to margin-parallel. Comparing S_{Hmax} with maximum horizontal shortening (e_{Hmax}) direction from the strain rate shows groups close to the margin have S_{Hmax} directions similar to the original e_{Hmax} from observed GPS velocities, while inland from the margin the S_{Hmax} is similar to the residual e_{Hmax} from GPS velocities with the subduction component is removed.

The stress results reflect the dominant strain accumulation which changes across the region. Near the margin, along the west coast of Vancouver Island, earthquakes in the upper plate are caused by the strain build-up due to the convergence of the North American and Juan de Fuca plates. This is due to the locked interface between the plates and the transfer of stress to the upper plate causing it to deform by shortening and uplift. Approximately 150 km inland, the stress results reflect the residual strain related to the permanent crustal deformation caused by the northward push of the Oregon block. The direction of this push rotates with the strike of the subduction zone to keep it approximately margin-parallel. The change in orientation could be caused by the lack of coupling between the plates further from the subduction margin where the mantle wedge may be separating the plates. Wang (1996), Wang and Jiangheng (1999) and Wang (2000) use numerical models to explain that dominant margin-parallel stresses at subduction zones are due to a low-stress forearc. The forearc is considered low-stress if the margin-parallel compression from the subduction does not exceed the vertical stress from topography and can occur when the plate interface is weakly coupled.

These stress results help us understand what controls faulting in the crust and support

findings from numerical models on the strength of the subduction interface. Earthquakes further from the margin and close to large population centres are driven by margin-parallel stresses. These stress results reflect the long-term permanent deformation associated with the northward push of the Oregon block. Comparing these results with those from earthquake relocations and faulting we suggest that margin-parallel compression is likely being accommodated on east-west thrust faults in northern Washington and southwest British Columbia.

5.3 Can we monitor these forces using anisotropy?

To use anisotropy as a monitoring tool, a baseline must be established where the source and the average anisotropy is know at each station. We identify sources and variations of crustal anisotropy from shear-wave splitting measurements for over 20 permanent stations and 15 temporary stations in southwest British Columbia. A semi-automated shear-wave splitting analysis was performed on ∼4500 event-station pairs for local crustal earthquakes.

Results from shear-wave splitting show spatial variations in fast directions, with margin-parallel fast directions at most stations and margin-perpendicular fast directions at stations in the northeast of the region. To use seismic anisotropy as a stress indicator requires identifying which stations are influenced by stress and which by structure. We determine the source of anisotropy at each station by comparing fast directions from shear-wave splitting results to the S_{Hmax} orientation determined from earthquake focal mechanism inversion.

The fast direction from the majority of stations align with the S_{Hmax} direction and

have small delay times of 0.1±0.07 seconds. Delay times do not increase with depth suggesting that the main influence of anisotropy resides in the upper crust. The similarity between fast direction and S_{Hmax} implies that anisotropy its caused by stress-aligned fluid-filled microcracks known as extensive dilatancy anisotropy. Along the west coast of Vancouver Island the S_{Hmax} direction changes to margin-perpendicular due to the influence of the locked subduction interface but we do not observe a similar change in the fast directions. This discrepancy can be attributed to the two sets of observations sampling different regions in the crust. The focal mechanisms used in the stress inversion sample a region of the crust at 10–20 km depth which is likely influenced by the locked subduction thrust fault. The shear-wave splitting likely measures anisotropy of the uppermost 10 km and reflects the long-term margin-parallel stress due to the low-stress forearc and the rotation of the Oregon block.

Stations with a strong correlation with S_{Hmax} and long periods of observations are further analyzed for temporal variations. Most stations have scatter in fast directions but show little systematic variation with time; however, we observe some evidence for delay time variation at station OZB associated with a M_L 5 earthquake and changes at station SNB associated with ETS and smaller (M_L 3) earthquakes. These temporal variations are not conclusive and would benefit from the collection and analysis of more data. A larger dataset is also required to reduce the standard error in the mean at stations with few observations.

The ideal scenario for investigating temporal variations in anisotropy would be to observe splitting from repeating events before, during and after, an earthquake or ETS event. A possible set of earthquakes that might be used is the San Juan Island events that were discussed in section 2.4.2. These events would also have to have a propagation direction within 15° of the orientation of S_{Hmax}. These conditions are

difficult to obtain due to the requirement for earthquakes to occur regularly with high quality recordings to perform shear-wave splitting analysis.

Shear-wave splitting results from this study have laid the groundwork for future studies on variations in anisotropy that might be related to changes in stress. A baseline for shear-wave splitting parameters has been determined at many stations in southwest British Columbia. With longer periods of observations this data could be used to further investigate temporal variations associated with earthquakes or ETS events.

5.4 Conclusions

The objective of this thesis was to gain an understanding of the processes that influence crustal faulting in the North American crust of northern Cascadia and to determine if they can be monitored. The following are important results which contribute to this understanding.

- Results from stress inversions show that S_{Hmax} is margin-parallel for most of southwest British Columbia and northern Washington, except along the west coast of Vancouver Island where S_{Hmax} is margin-perpendicular. The margin-perpendicular stress is due to the locked interface between the plates and the transfer of stress to the upper plate causing it to deform by shortening and uplift. Although the interface is locked it is only weakly coupled as suggested by the change in S_{Hmax} orientation further from the coast to margin-parallel. This margin-parallel stress is related to the northern push of the Oregon block and a low-stress forearc. If the plate interface was strongly coupled we would

expect S_{Hmax} to be margin perpendicular over most of the region.

- Results from earthquake relocations and focal mechanisms suggest that the north-south compression from the margin-parallel stress is accommodated along steeply-dipping east-west striking thrust faults. These faults have been identified in this study using earthquake relocations and in other studies using precise topography and bathymetry mapping, seismic reflection and trenching methods.

- Results from precise earthquake relocations over two regions in southwest British Columbia and northern Washington reveals seismicity that occurs on small structures or lineations. In the San Juan Islands the trend of the seismicity has a similar orientation to the strike of recently mapped faults on the surface, but in the Fraser River Valley few surface faults are mapped making it difficult to interpret the features in the seismicity. We found using the double-difference relocation method with differential catalogue and waveform cross-correlations essential for identifying hidden structures in the background seismicity. We also note the importance of using an appropriate velocity model to remove artifacts and reduce location errors.

- The compilation of new and previously determined focal mechanisms resulted in a database of ∼1000 source mechanisms for crustal earthquakes. These mechanisms showed a variety of faulting styles but were dominated thrust, strike-slip or combination thereof. This is also shown by the stress inversion results where most results related to an oblique-thrust stress regime.

The combination of different seismological methods, such as those used in this study (earthquake relocations, focal mechanisms, stress and anisotropy), have contributed to the improved understanding of processes in the crust. Earthquake relocations have

revealed where earthquakes predominately occur and combined with focal mechanisms and surface faulting information we can attribute the seismicity to accommodating the margin-parallel compression observed in the regional stress. Seismic anisotropy is related to the margin-parallel stress and has the potential to be used to monitor stress changes. Investigating changes is stress may contribute to the understanding of processes related to earthquakes (M>3) and episodic tremor and slip events.

Bibliography

Abers, G. and Gephart, J. (2001), Direct inversion of earthquake first motions for both the stress tensor and focal mechanisms and application to southern California, *Journal of Geophysical Research* **106**(B11): 26523–26540.

Altamimi, Z., Sillard, P. and Boucher, C. (2002), ITRF2000: A new release of the International Terrestrial Reference Frame for earth science applications, *Journal of Geophysical Research* **107**(B10): 2214–2232.

Anderson, E. (1951), *The dynamics of faulting and dyke formation with applications to Britain.*, Oliver and Boyd, Edinburgh.

Angerer, E., Crampin, S., Li, X.-Y. and Davis, T. (2002), Processing, modelling, and predicting time-lapse effects of over-pressured fluid injection in a fractured reservoir., *Geophysical Journal International* **149**: 267–280.

Arnold, R. and Townend, J. (2007), A Bayesian approach to estimating tectonic stress from seismological data, *Geophysical Journal International* **170**(3): 1336–1356.

Atwater, B. (1987), Evidence for great Holocene earthquakes along outer coast of Washington State, *Science* **236**: 942–944.

Atwater, T. (1970), Implications of plate tectonics for the Cenozoic tectonic evolution of western North America, *Geological Society of America Bulletin* **81**: 3513–3536.

Babuska, V. and Cara, M. (1991), *Seismic Anisotropy in the Earth*, Vol. 10, Kluwer Academic Publishers.

Balfour, N., Cassidy, J., Dosso, S. and Mazzotti, S. (2011), Mapping Crustal Stress and Strain in Southwest British Columbia, *Journal of Geophysical Research* p. 10.1029/2010JB008003.

Balfour, N., Savage, M. and Townend, J. (2005), Stress and crustal anisotropy in Marlborough, New Zealand: evidence for low fault strength and structure-controlled anisotropy, *Geophysical Journal International* **163**(3): 1073–1086.

Barnett, E. (2007), *Active faulting at the northeast margin of the greater Puget Lowland: a paleoseismic and magnetic-anomaly study of the Kendall fault scarp, Whatcom County, Northwest Washington*, Master's thesis, Humbolt State University.

Blakely, R., Wells, R., WEAVER, C. and Johnson, S. Y. (2002), Location, structure, and seismicity of the Seattle fault zone, Washington: Evidence from aeromagnetic anomalies, geologic mapping, and seismic-reflection data, *Geological Society of America Bulletin* **114**: 169–177.

Bolton, M. (2003), *Juan de Fuca Plate Seismicity at the Northern End of the Cascadia Subduction Zone*, Master's thesis, University of Victoria.

Boness, N. and Zoback, M. D. (2006), A multiscale study of the mechanisms controlling shear velocity anisotropy in the San Andreas Fault Observatory at Depth, *Geophysics* **71**(5): F131–F146.

Bott, M. (1959), The mechanics of oblique slip faulting, *Geology Magazine* pp. 109–117.

Bozorgnia, Y., Hachem, M. and Campbell, K. (2010), Ground motion prediction equation ("attenuation relationship") for inelastic response spectra, *Earthquake Spectra* **26**(1): 1–23.

Brandon, M. (1989), Geology of the San Juan-Cascade Nappes, Northwestern Cascade Range and San Juan Islands, *Washington Division of Geology and Earth Resources Information Circular* **86**.

Britton, J., Harris, J., Hunter, J. and Luternauer, J. (1995), The bedrock surface beneath the Fraser River delta in British Columbia based on seismic measurements, *Current Research 1995-E, Geological Survey of Canada* pp. 83–89.

Byerlee, J. (1978), Friction of Rocks, *Pure and Applied Geophysics* **116**: 615–626.

Calvert, A. and Clowes, R. (1990), Deep, high-amplitude reflections from a major shear zone above the subducting Juan de Fuca plate, *Geology* **18**(11): 1091.

Cassidy, J. and Bostock, M. (1996), Shearwave splitting above the subducting Juan de Fuca Plate, *Geophysical Research Letters* **23**(9): 941–944.

Cassidy, J., Rogers, G. and Waldhauser, F. (2000), Characterization of active faulting beneath the Strait of Georgia, British Columbia, *Bulletin of the Seismological Society of America* **90**(5): 1188–1199.

Clowes, R., Brandon, M., Green, A., Yorath, C., Brown, A., Kanasewich, E. and Spencer, C. (1987), LITHOPROBE-southern Vancouver Island: Cenozoic sub-

duction complex imaged by deep seismic reflections, *Canadian Journal of Earth Sciences* **24**(1): 31–51.

Convertito, V. and Herrero, A. (2004), Influence of focal mechanism in probabilistic seismic hazard analysis, *Bulletin of the Seismological Society of America* **94**(6): 2124.

Crampin, S. (1994), The fracture criticality of crustal rocks, *Geophysical Journal International* **118**: 428–438.

Crampin, S., Gao, Y. and Peacock, S. (2008), Stress-forecasting (not predicting) earthquakes: A paradigm shift?, *Geology* **36**(5): 427–430.

Crampin, S. and Peacock, S. (2008), A review of the current understanding of seismic shear-wave splitting in the Earth's crust and common fallacies in interpretation, *Wave Motion* **45**(6): 675–722.

Crampin, S., Volti, T., Chastin, S., Gudmundsson, A. and Stefánsson, R. (2002), Indication of high pore-fluid pressures in a seismically-active fault zone, *Geophysical Journal International* **151**(2): F1–F5.

Currie, C., Cassidy, J. and Hyndman, R. (2001), A regional study of shear wave splitting above the Cascadia Subduction Zone: Margin-parallel crustal stress, *Geophysical Research Letters* **28**(4): 659–662.

Currie, C., Cassidy, J., Hyndman, R. and Bostock, M. (2004), Shear wave anisotropy beneath the Cascadia subduction zone and western North American craton, *Geophysical Journal International* **157**: 341–353.

DeMets, C., Gordon, D., Argus, D. and Stein, S. (1990), Current plate motions, *Geophysics Journal International* **101**: 425–478.

DeMets, C., Gordon, R., Argus, D. and Stein, S. (1994), Effect of recent revisions to the geomagnetic reversal time scale on estimates of current plate motions, *Geophysical Research Letters* **21**(20): 2191–2194.

Dragert, H., Hyndman, R., Rogers, G. and Wang, K. (1994), Current deformation and the width of the seismogenic zone of the northern Cascadia subducted thrust, *Journal of Geophysical Research* **99**: 635–668.

Evans, R. (1984), Effects of the free surface on shear wavetrains, *Geophysical Journal of the Royal Astronomical Society* **76**: 165–172.

Frohlich, C. (1992), Triangle diagrams: ternary graphs to display similarity and diversity of earthquake focal mechanisms, *Physics of the Earth and Planetary Interiors* **75**(1-3): 193–198.

Gephart, J. (1990), Stress and the direction of slip on fault planes, *Tectonics* **9**(4): 845–858.

Gephart, J. and Forsyth, D. (1984), An improved method for determining the regional stress tensor using earthquake focal mechanism data: application to the San Fernando earthquake sequence, *Journal of Geophysical Research* **89**(B11): 9305–9320.

Gerst, A. and Savage, M. K. (2004), Seismic anisotropy beneath Ruapehu volcano: A possible eruption forecasting tool, *Science* **306**: 1543–1547.

Godfrey, N., Christensen, N. and Okaya, D. (2000), Anisotropy of schists: Contribu-

tion of crustal anisotropy to active source seismic experiments and shear wave splitting observations, *Journal of Geophysical Research* **105**(B12): 27991–28007.

Goldfinger, C., Grijalva, K., Burgmann, R., Morey, A. E., Johnson, J. E., Nelson, C. H., Gutierrez-Pastor, J., Ericsson, A., Karabanov, E., Chaytor, J. D., Patton, J. and Gracia, E. (2008), Late Holocene Rupture of the Northern San Andreas Fault and Possible Stress Linkage to the Cascadia Subduction Zone, *Bulletin of the Seismological Society of America* **98**(2): 861–889.

Hauksson, E. and Shearer, P. (2005), Southern California hypocenter relocation with waveform cross-correlation, part 1: Results using the double-difference method, *Bulletin of the Seismological Society of America* **95**(3): 896–903.

Hodgson, E. (1946), British Columbia earthquake, June 23, 1946, *Journal of the Royal Astronomical Society of Canada* **11**(8): 285–319.

Hyndman, R., Rogers, G., Dragert, D., Wang, K., Clague, J., Adams, J. and Bobrowsky, P. (1996), Giant earthquakes beneath Canda's west coast, *Geoscience Canada* **23**(2): 63–72.

Hyndman, R., Wang, K., Yuan, T. and Spence, G. (1993), Tectonic sediment thickening, fluid expulsion, and the thermal regime of subduction zone accretionary prisms: the Cascadia margin off Vancouver Island, *Journal of Geophysical Research* **98**(B12): 21865–21876.

Hyndman, R., Yorath, C., Clowes, R. and Davis, E. E. (1990), The northern Cascadia subduction zone at Vancouver Island: seismic structure and tectonic history, *Canadian Journal of Earth Science* **27**: 313–329.

Johnson, S., Dadisman, S., Mosher, D., Blakely, R. and Childs, J. R. (2001), Active tectonics of the Devils Mountain Fault and related structures, northern Puget Lowland and eastern Strait of Juan de Fuca region, Pacific Northwest, *United States Geological Survey Professional Paper* **1044-9612**: 1–45.

Journeay, J. M. and Willams, S. P. (1995), Tectonic assemblage of the Canadian Cordillera, *Geological Survey of Canada Open File* **2948**.

Kaneshima, S., Ando, M. and Kimura, S. (1988), Evidence from shear-wave splitting for the restriction of seismic anisotropy to the upper crust, *Nature* **335**: 627–629.

Lamontagne, M., Halchuk, S., Cassidy, J. and Rogers, G. (2008), Significant Canadian Earthquakes of the period 1600–2006, *Seismological Research Letters* **79**(2): 211–223.

Lavenu, A. and Cembrano, J. (1999), Compressional-and transpressional-stress pattern for Pliocene and Quaternary brittle deformation in fore arc and intra-arc zones (Andes of Central and southern Chile), *Journal of Structural Geology* **21**(12): 1669–1691.

Lewis, J., Unruh, J. and Twiss, R. (2003), Seismogenic strain and motion of the Oregon coast block, *Geology* **31**(2): 183–186.

Lund, B. (2000), *Crustal stress studies using microearthquakes and boreholes*, PhD thesis, Uppsala University.

Lund, B. and Townend, J. (2007), Calculating horizontal stress orientations with full or partial knowledge of the tectonic stress tensor, *Geophysical Journal International* **170**(3): 1338–1335.

MacQueen, J. (1967), Some methods for classification and analysis of multivariate observations, *Proceedings of the fifth Berkeley symposium on mathematical statistics and probability* **1**(281-297): 14.

Maekawa, H. and Brown, E. H. (1991), Kinematic analysis of the San Juan thrust system, Washington, *Geological Society of America Bulletin* **103**: 1007–1016.

Mazzotti, S., Dragert, H., Henton, J., Schmidt, M., Hyndman, R., James, T., Lu, Y. and Craymer, M. (2003), Current tectonics of northern Cascadia from a decade of GPS measurements, *Journal of Geophysical Research* **108**: 2554.

Mazzotti, S., Dragert, H., Hyndman, R., Miller, M. and Henton, J. (2002), GPS deformation in a region of high crustal seismicity: Northern Cascadia forearc, *Earth and Planetary Science Letters* **198**(1-2): 41–48.

Mazzotti, S., Henry, P. and Pichon, X. L. (2001), Transient and permanent deformation of central Japan estimated by GPS:: 2. Strain partitioning and arc-arc collision, *Earth and Planetary Science Letters* **184**(2): 455–469.

McCaffrey, R., Long, M., Goldfinger, C., Zwick, P., Nabelek, J., Johnson, C. and Smith, C. (2000), Rotation and plate locking at the southern Cascadia subduction zone, *Geophysical Journal International* **27**(19): 3117—3120.

McCaffrey, R., Qamar, A., King, R., Wells, R., Khazaradze, G., Williams, C., Stevens, C., Vollick, J. and Zwick, P. (2007), Fault locking, block rotation and crustal deformation in the Pacific Northwest, *Geophysical Journal International* **169**(3): 1315–1340.

McCrory, P. A., Blair, J. L., Oppenheimer, D. H. and Walter, S. R. (2004), Depth to the Juan de Fuca slab beneath the Cascadia subduction margin: A 3-D model

for sorting earthquakes, *United States Geological Survey Data Series DS-91, 1 CD-ROM.* .

McKenzie, D. (1969), The relation between fault plane solutions for earthquakes and the directions of the principal stresses, *Bulletin of the Seismological Society of America* **59**(2): 591–601.

Michael, A. (1984), Determination of stress from slip data: faults and folds, *Journal of Geophysical Research* **89**(B13): 11517–11526.

Michael, A. (1987), Use of focal mechanisms to determine stress: a control study, *Journal of Geophysical Research* **92**: 357–369.

Michelini, A. and Lomax, A. (2004), The effect of velocity structure errors on double-difference earthquake location, *Geophysical Research Letters* **31**(L09602).

Molnar, S. (2011), *Predicting earthquake ground shaking due to 1-D soil layering and 3-D basin structure in southwest British Columbia, Canada.*, PhD thesis, University of Victoria.

Monger, J., Price, R. and Tempelman-Kluit, D. (1982), Tectonic accretion and the origin of the two major metamorphic and plutonic welts in the Canadian Cordillera, *Geology* **10**(2): 70–75.

Monger, J., Souther, J. and Gabrielse, H. (1972), Evolution of the Canadian Cordillera; a plate-tectonic model, *American Journal of Science* **272**(7): 577–602.

Mulder, T. (1995), *Small earthquakes in southwestern British Columbia (1975–1991)*, Master's thesis, University of Victoria.

Nicholson, T., Bostock, M. and Cassidy, J. (2005), New constraints on subduction zone structure in northern Cascadia, *Geophysical Journal International* **161**(3): 849–859.

Nuttli, O. W. (1961), The effect of the Earth's surface on the S wave particle motion, *Bulletin of the Seismological Society of America* **51**: 237–246.

Okaya, D., Christensen, N., Stanley, D. and Stern, T. (1995), Crustal anisotropy in the vicinity of the Alpine Fault, South Island, New Zealand, *New Zealand of Geology and Geophysics* **38**: 579–583.

Padhy, S. and Crampin, S. (2006), High pore-fluid pressures at Bhuj, inferred from 90 degree flips in shear-wave polarization, *Geophysical Journal International* **164**(doi:10.1111/j.1365-246X.2006.02854): 370 – 376.

Paige, C. and Saunders, M. (1982a), Algorithm 583: LSQR: Sparse linear equations and least squares problems, *ACM Transactions on Mathematical Software (TOMS)* **8**(2): 195–209.

Paige, C. and Saunders, M. (1982b), LSQR: An algorithm for sparse linear equations and sparse least squares, *ACM Transactions on Mathematical Software (TOMS)* **8**(1): 43–71.

Paulssen, H. (2004), Crustal Anisotropy in southern California from local earthquake data, *Geophysical Research Letters* **31**(L01601): 1–4.

Pavlis, G., Vernon, F., Harvey, D. and Quinlan, D. (2004), The generalized earthquake-location (GENLOC) package: an earthquake-location library, *Computers & Geosciences* **30**(9-10): 1079–1091.

Pullan, S., Hunter, J. A., Jol, H. M., Roberts, M. C., Burns, R. A. and Harris, J. B. (1998), Seismostratigraphic investigations of the southern Fraser River delta, *in* J. J. Clague, J. L. Luternauer and D. C. Mosher (eds), *Geology and Natural Hazards of the Fraser River Delta, British Columbia*, Vol. 525, Geological Survey of Canada Bulletin, pp. 91–122.

Ramachandran, K., Dosso, S., Spence, G., Hyndman, R. and Brocher, T. (2005), Forearc structure beneath southwestern British Columbia: A three-dimensional tomographic velocity model, *Journal of Geophysical Research* **110**(B02303).

Ramachandran, K., Dosso, S., Zelt, C., Spence, G., Hyndman, R. and Brocher, T. (2004), Upper crustal structure of southwestern British Columbia from the 1998 Seismic Hazards investigation in Puget Sound, *Journal of Geophysical Research* **109**(B09303).

Ramachandran, K., Hyndman, R. and Brocher, T. (2006), Regional P-wave velocity structure of the northern Cascadia subduction zone, *Journal of Geophysical Research* **111**(B12301).

Reasenberg, P. and Oppenheimer, D. (1985), FPFIT, FPPLOT, and FPPAGE: FORTRAN computer programs for calculating and displaying fault-plane solutions, *United States Geology Survey Open File Report* **85-0739**: 85–739.

Ricketts, B. D. (1998), Groundwater flow beneath the Fraser River Delta, British Columbia; a preliminary model., *in* J. J. Clague, J. L. Luternauer and D. C. Mosher (eds), *Geology and Natural Hazards of the Fraser River Delta, British Columbia*, Vol. 525, Geological Survey of Canada Bulletin, pp. 241–255.

Riddihough, R. (1977), A model for recent plate interactions off Canada's west coast,

Canadian Journal of Earth Sciences **14**: 384—396.

Riddihough, R. (1984), Recent movements of the Juan de Fuca plate system, *Journal of Geophysical Research* **89**(B8): 6980–6994.

Ristau, J., Rogers, G. and Cassidy, J. (2007), Stress in western Canada from regional moment tensor analysis, *Canadian Journal of Earth Sciences* **44**(2): 127–148.

Rogers, G. (1979), Earthquake fault plane solutions near Vancouver Island, *Canadian Journal of Earth Science* **16**: 523–531.

Rogers, G. (1983), *Seismotectonics of British Columbia*, PhD thesis, University of British Columbia.

Rogers, G. (1988), An assessment of the megathrust earthquake potential of the Cascadia subduction zone, *Canadian Journal of Earth Sciences* **25**(6): 844–852.

Rogers, G. (1998), Earthquakes and earthquake hazard in the Vancouver area, *Geology and Natural Hazards of the Fraser River Delta, British Columbia* **525**: 17—25.

Rogers, G. and Hasegawa, H. (1978), A second look at the British Columbia earthquake of June 23, 1946, *Bulletin of the Seismological Society of America* **68**(3): 653–675.

Satake, K., Shimazaki, K., Tsuji, Y. and Ueda, K. (1996), Time and size of a giant earthquake in Cascadia inferred from Japanese tsunami records of January 1700, *Nature* **379**: 246–249.

Savage, M., Ohminato, T., Aoki, Y., Tsuji, H. and Greve, S. (2010), Stress magnitude and its temporal variation at Mt. Asama Volcano, Japan, from seismic anisotropy

and GPS, *Earth and Planetary Science Letters* .

Sherrod, B., Brocher, T., Weaver, C., Bucknam, R. C., Blakely, R., Kelsey, H. M., Nelson, A. R. and Haugerud, R. (2004), Holocene fault scarps near Tacoma, Washington, USA, *Geology* **32**: 9–12.

Silver, P. and Chan, W. (1991), Shear-wave splitting and subcontinental mantle deformation, *Journal of Geophysical Research* **96**: 16429–16454.

Teanby, N., Kendall, J.-M. and van der Baan, M. (2004), Automation of shear-wave splitting measurements using cluster analysis, *Bulletin of the Seismological Society of America* **94**(2): 453–463.

Townend, J. and Zoback, M. (2006), Stress, strain, and mountain building in central Japan, *Journal of Geophysical Research* **111**(B03411).

Wada, I., Mazzotti, S. and Wang, K. (2010), Intraslab Stresses in the Cascadia Subduction Zone from Inversion of Earthquake Focal Mechanisms, *Bulletin of the Seismological Society of America* **100**(5A).

Waldhauser, F. (2001), hypoDD - A program to compute double-difference hypocenter locations, *United States Geological Survey Open File Report* pp. 1–25.

Waldhauser, F. and Ellsworth, W. (2000), A double-difference earthquake location algorithm: method and application to the northern Hayward fault, California, *Bulletin of the Seismological Society of America* **90**(6): 1353–1368.

Waldhauser, F., Ellsworth, W., Schaff, D. and Cole, A. (2004), Streaks, multiplets, and holes: High-resolution spatio-temporal behavior of Parkfield seismicity, *Geophysical Research Letters* **31**(L18608).

Wallace, R. (1951), Geometry of shearing stress and relation to faulting, *Journal of Geology* **59**: 118–130.

Wang, K. (1996), Simplified analysis of horizontal stresses in a buttressed forearc silver at an oblique subduction zone, *Geophysical Research Letters* **23**(16): 2021–2024.

Wang, K. (2000), Stress-strain 'paradox', plate coupling, and forearc seismicity at the Cascadia and Nankai subduction zones, *Tectonophysics* **319**: 321–338.

Wang, K., Hu, Y., Bevis, M., Kendrick, E., Jr, R. S., Vargas, R. and Lauría, E. (2007), Crustal motion in the zone of the 1960 Chile earthquake: Detangling earthquake-cycle deformation and forearc-sliver translation, *Geochemistry Geophysics Geosystems* **8**(10): Q10010.

Wang, K. and Jiangheng, H. (1999), Mechanics of low-stress forearcs: Nankai and Cascadia, *Journal of Geophysical Research* **104**(B7): 15191–15205.

Wang, K., Wells, R., Mazzotti, S., Hyndman, R. and Sagiya, T. (2003), A revised dislocation model of interseismic deformation of the Cascadia subduction zone, *Journal of Geophysical Research* **108**(B1, 2026).

Wells, R. and Simpson, R. (2001), Northward migration of the Cascadia forearc in the northwestern US and implications for subduction deformation, *Earth Planets and Space* **53**(4): 275–284.

Zatsepin, S. and Crampin, S. (1997), Modelling the compliance of crustal rock-I. Response of shear-wave splitting to differential stress, *Geophysical Journal International* **129**(3): 477–494.

Zoback, M. (1992), First-and second-order patterns of stress in the lithosphere: the world stress map project, *Journal of Geophysical Research* **97**(B8): 11703–11728.

Zoback, M. D. and Zoback, M. L. (2002), Stress in the Earth's Lithosphere, *Encyclopedia of Physical Science and Technology*, Vol. 16, Academic Press.

Appendix A

Stress Inversion Results

This appendix includes summaries of the stress inversions for each cluster. Individual information on focal mechanism data can be found on the accompanying CD.

CLUST	Cluster number.
CLAT	Latitude of centre of the cluster of focal mechanisms.
CLON	of centre of the cluster of focal mechanisms.
S_{Hmax}	Maximum horizontal compressive stress direction.
95%	95% confidence limit for S_{Hmax}.
e_{Hmax}O	Maximum horizontal shortening direction from the original data.
2σO	Standard error of e_{Hmax} orig.
e_{Hmax}R	Maximum horizontal shortening direction after the modelled subduction component is removed.
2σR	Standard error of e_{Hmax} resid.

Table A.1: S_{Hmax} and e_{Hmax} values for each cluster, including 95% confidence limit for S_{Hmax} and standard error for e_{Hmax}. Clusters 8, 9 and 26 are omitted as they contained too few (<4) focal mechanisms to perform the stress inversion.

CLUST	CLAT	CLON	S_{Hmax}	95%	e_{Hmax}O	2σO	e_{Hmax}R	2σR
1	48.866	-122.457	157	41	54	1	-7	67
2	50.446	-123.673	131	105	49	1	29	50
3	48.366	-124.804	36	61	53	1	-28	3
4	48.748	-122.072	159	37	54	2	0	68
5	49.317	-122.383	158	47	54	1	48	13
6	47.666	-122.294	3	56	61	3	1	54
7	48.169	-122.939	151	36	55	1	-8	2
10	48.232	-122.424	173	61	54	2	-5	15
11	48.867	-123.496	173	44	57	1	-18	13
12	47.579	-121.828	166	39	63	3	9	3
13	47.985	-120.265	165	116	58	3	14	6
14	49.585	-126.944	7	37	13	1	-43	19
15	49.54	-123.251	8	49	55	1	42	45
16	49.271	-123.719	178	39	55	1	-22	35
17	48.872	-122.757	171	103	55	1	-10	59
18	50.915	-124.839	64	167	23	2	17	66
19	48.638	-123.11	117	23	36	1	-12	8
20	48.435	-123.137	151	42	56	1	-10	6
21	48.511	-122.546	158	52	53	1	-7	20
22	48.933	-123.052	0	35	57	1	-12	46
23	48.907	-121.224	140	154	56	2	21	12
24	48.13	-121.764	116	64	55	4	-1	71
25	50.138	-127.822	42	53	13	2	49	9
27	50.712	-126.672	5	95	12	2	38	10
28	49.095	-125.603	11	56	40	2	-38	4
29	48.504	-123.532	137	36	57	1	-15	3
30	48.892	-124.151	166	78	56	1	-38	4
31	49.859	-122.828	151	90	52	1	56	10
32	49.782	-123.69	165	28	43	1	26	68
33	47.492	-122.779	27	82	62	2	0	80
34	49.137	-122.709	144	47	54	1	1	65

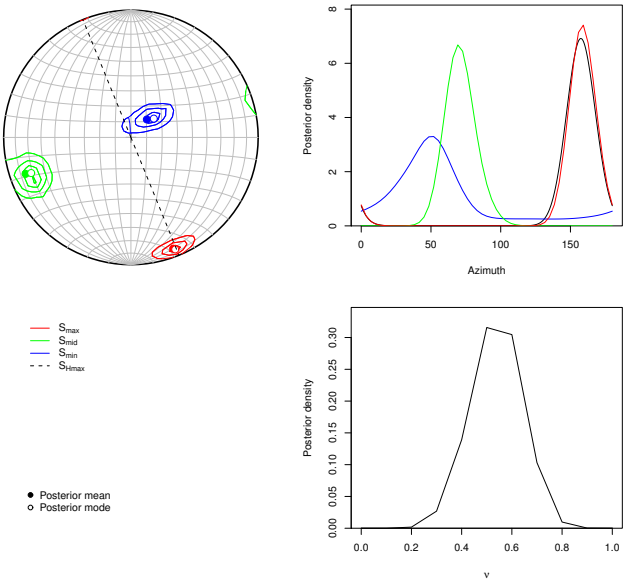

Figure A.1: Stress inversion result for cluster 1.

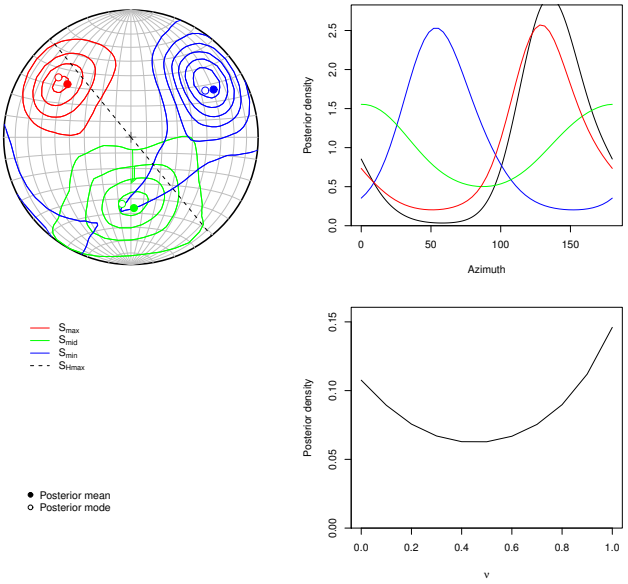

Figure A.2: Stress inversion result for cluster 2.

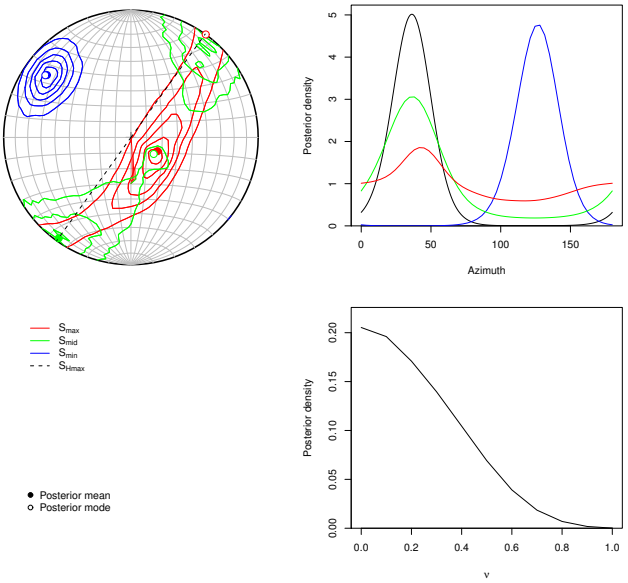

Figure A.3: Stress inversion result for cluster 3.

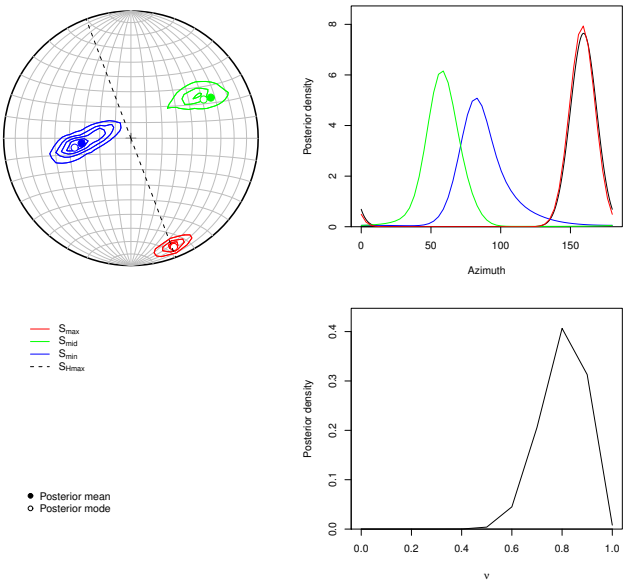

Figure A.4: Stress inversion result for cluster 4.

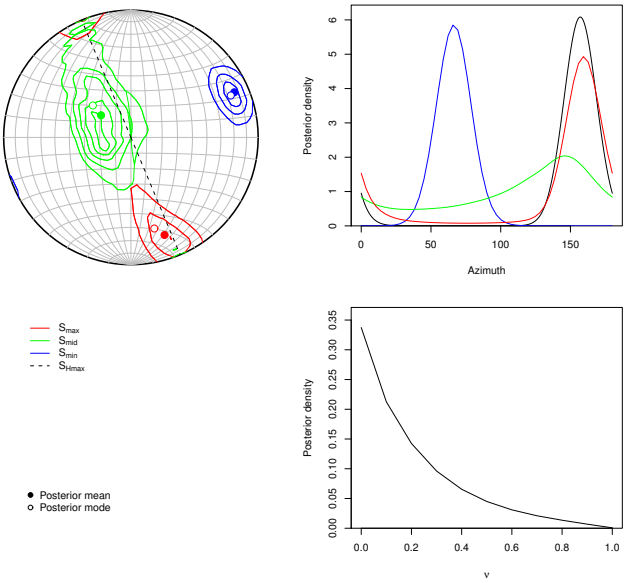

Figure A.5: Stress inversion result for cluster 5.

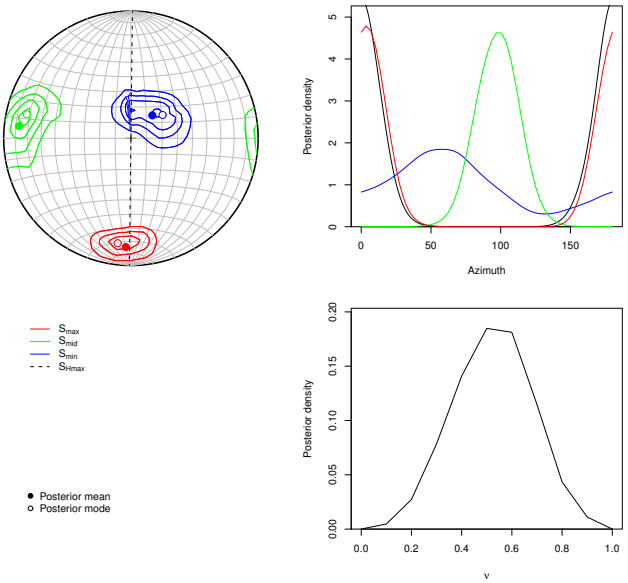

Figure A.6: Stress inversion result for cluster 6.

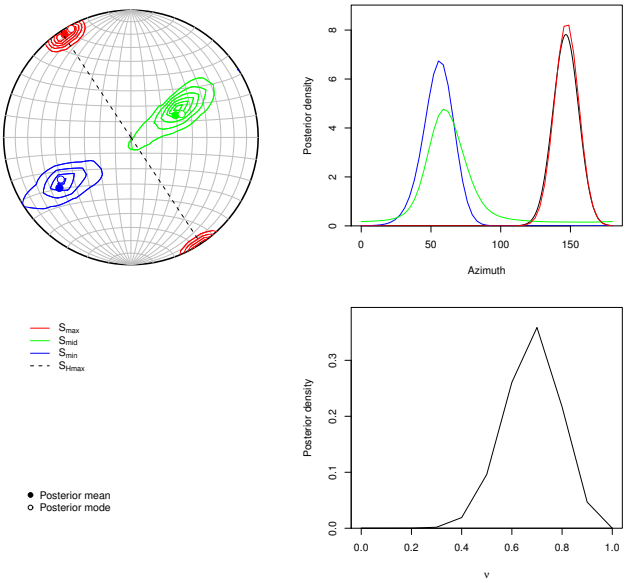

Figure A.7: Stress inversion result for cluster 7.

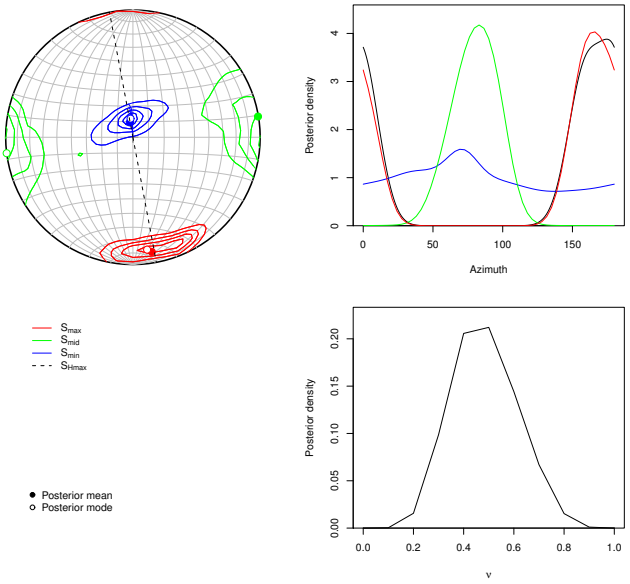

Figure A.8: Stress inversion result for cluster 10.

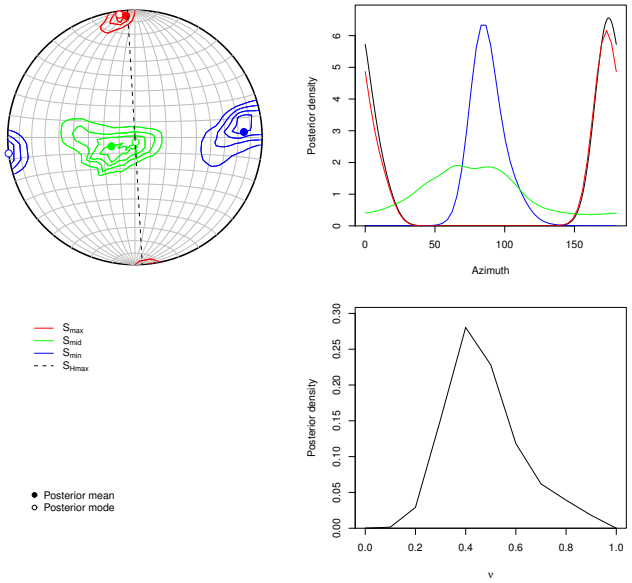

Figure A.9: Stress inversion result for cluster 11.

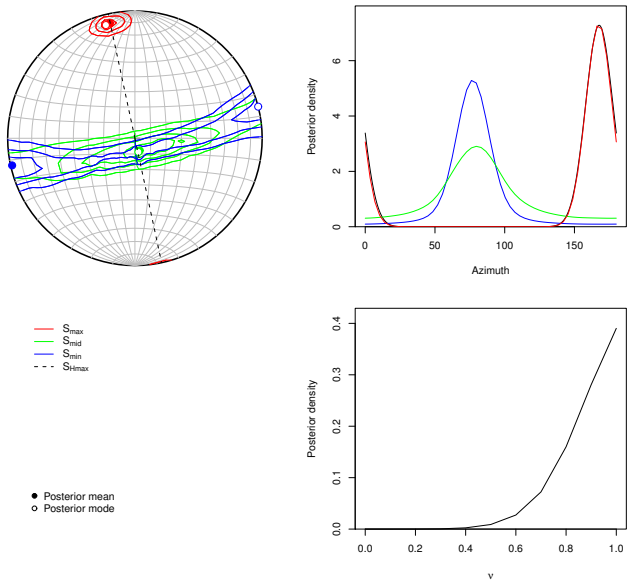

Figure A.10: Stress inversion result for cluster 12.

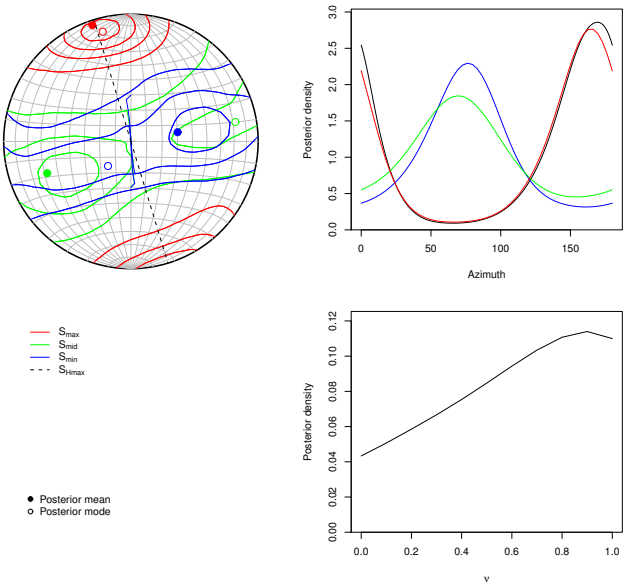

Figure A.11: Stress inversion result for cluster 13.

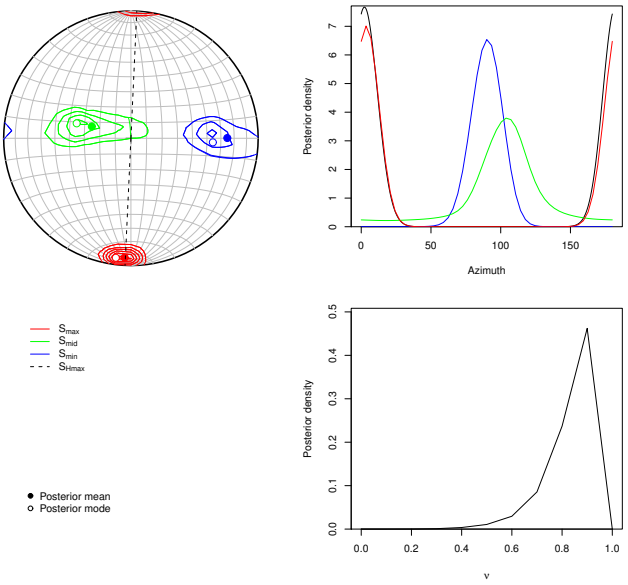

Figure A.12: Stress inversion result for cluster 14.

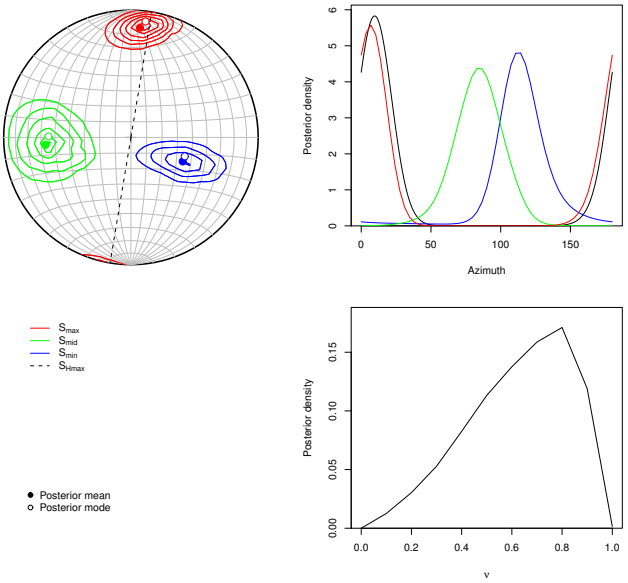

Figure A.13: Stress inversion result for cluster 15.

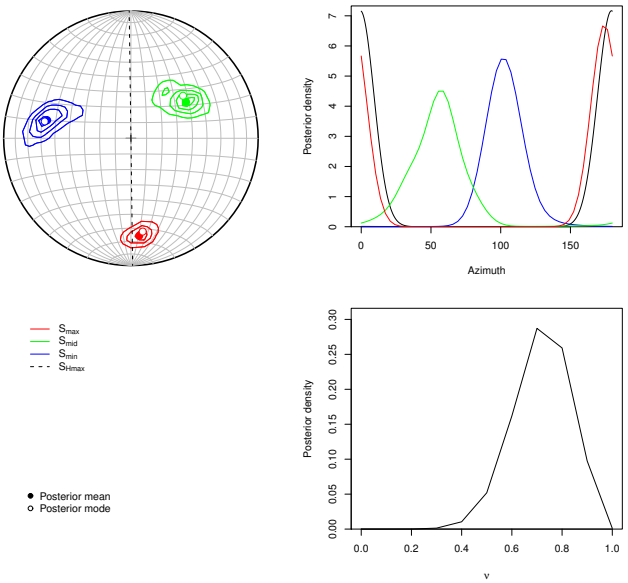

Figure A.14: Stress inversion result for cluster 16.

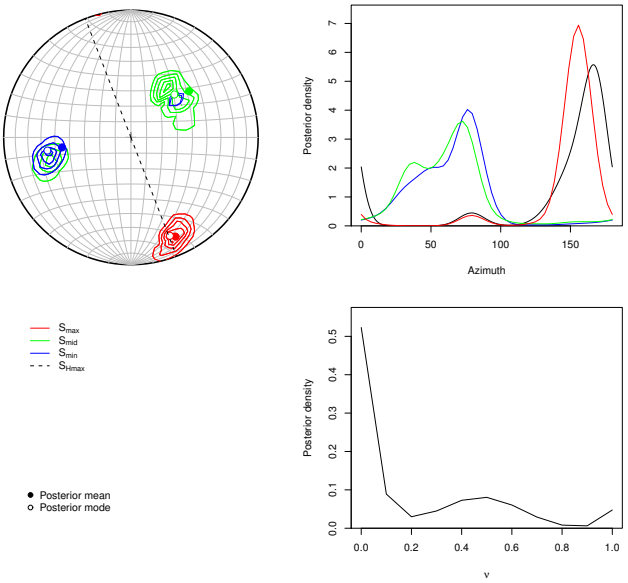

Figure A.15: Stress inversion result for cluster 17.

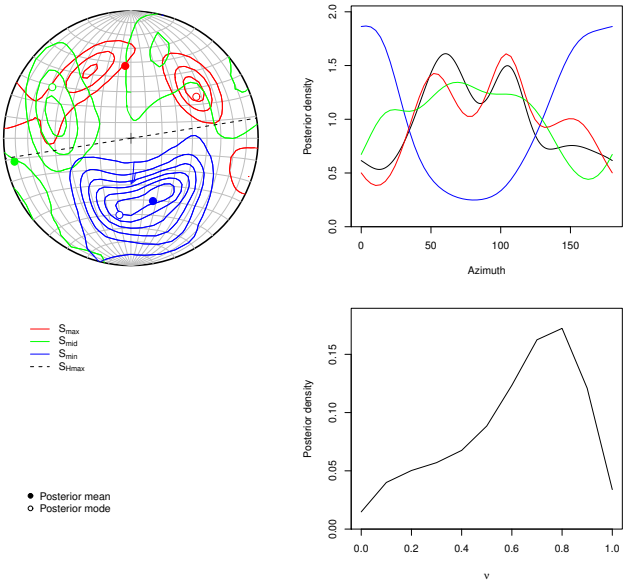

Figure A.16: Stress inversion result for cluster 18.

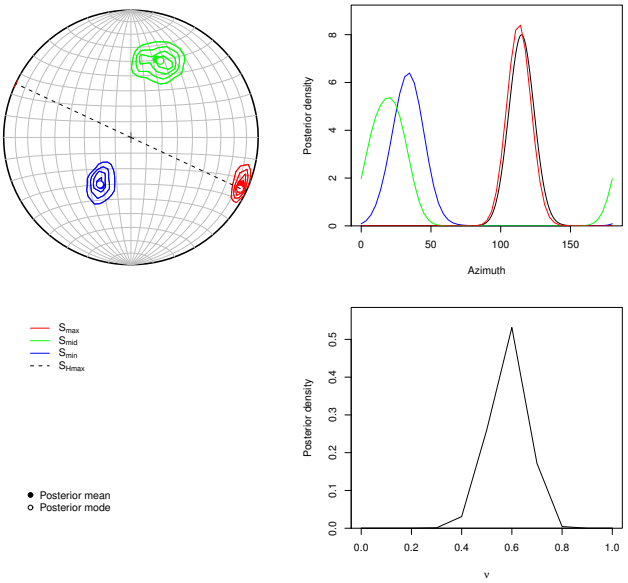

Figure A.17: Stress inversion result for cluster 19.

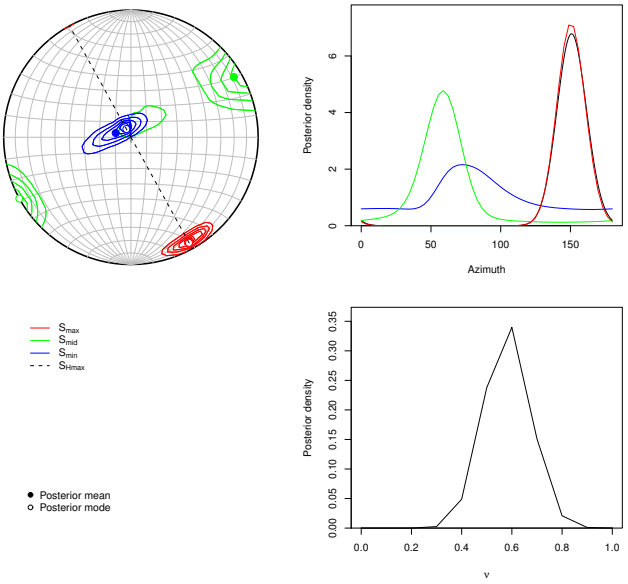

Figure A.18: Stress inversion result for cluster 20.

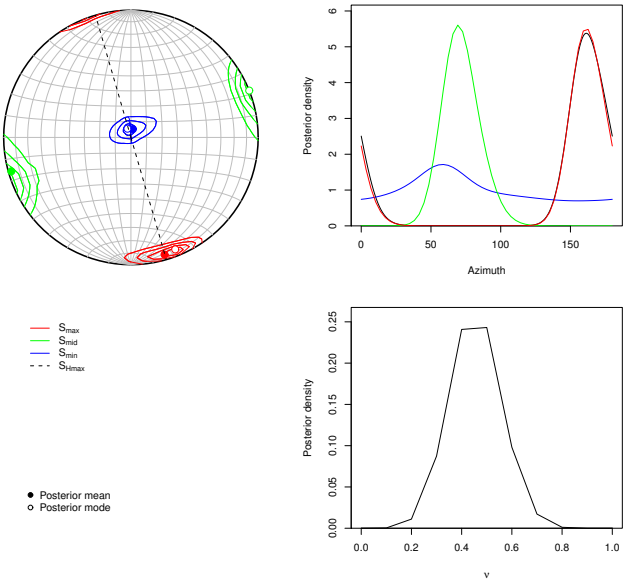

Figure A.19: Stress inversion result for cluster 21.

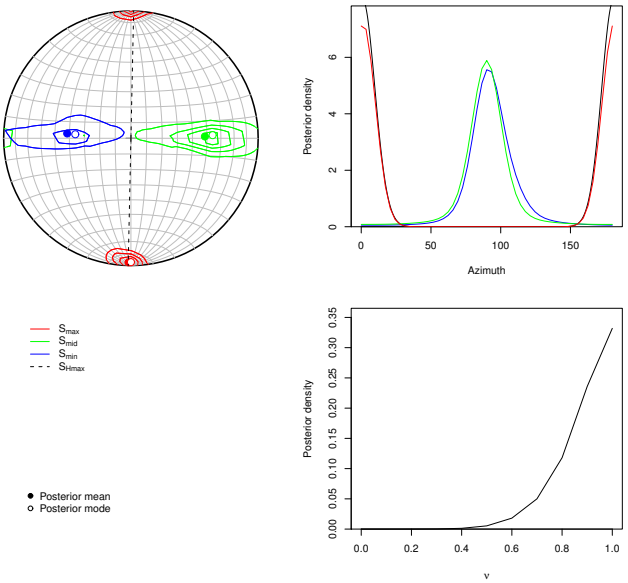

Figure A.20: Stress inversion result for cluster 22.

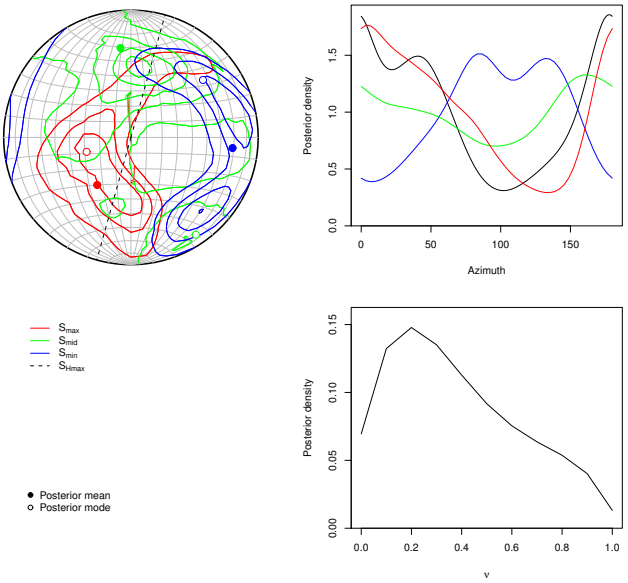

Figure A.21: Stress inversion result for cluster 23.

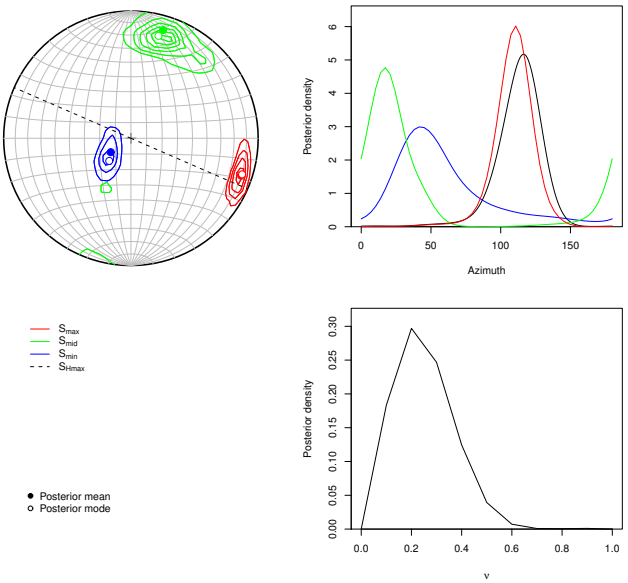

Figure A.22: Stress inversion result for cluster 24.

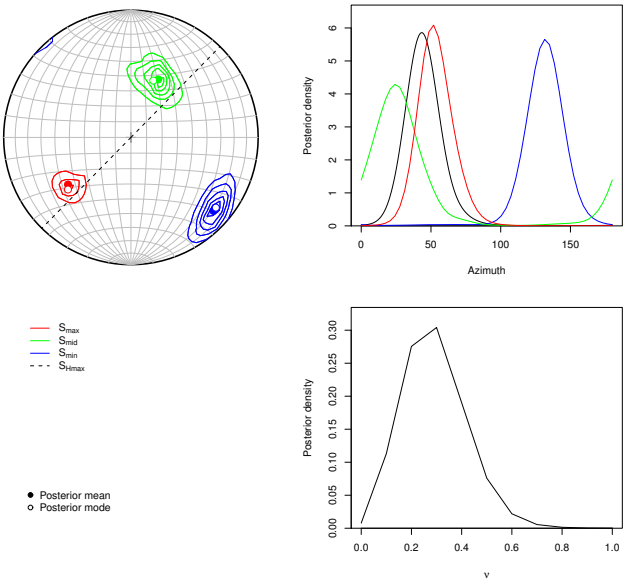

Figure A.23: Stress inversion result for cluster 25.

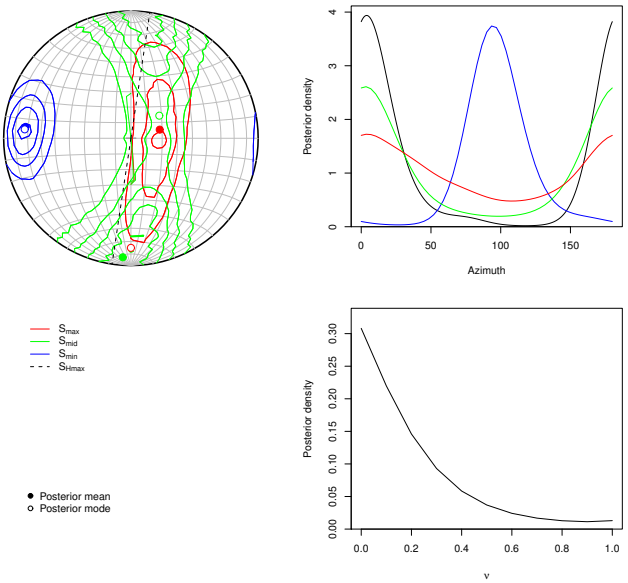

Figure A.24: Stress inversion result for cluster 27.

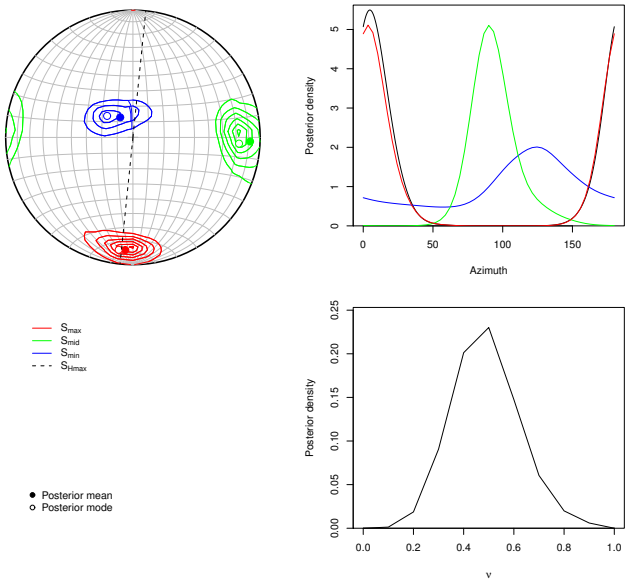

Figure A.25: Stress inversion result for cluster 28.

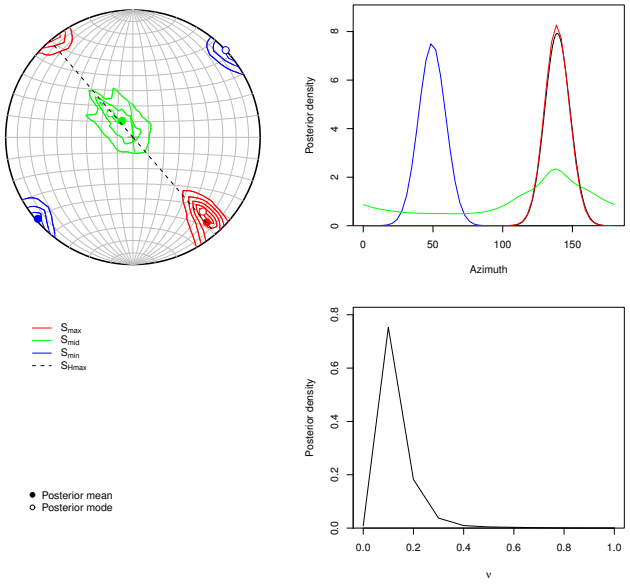

Figure A.26: Stress inversion result for cluster 29.

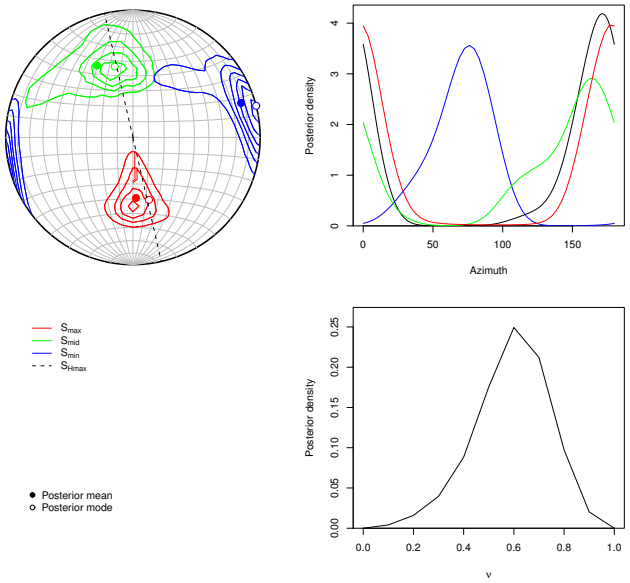

Figure A.27: Stress inversion result for cluster 30.

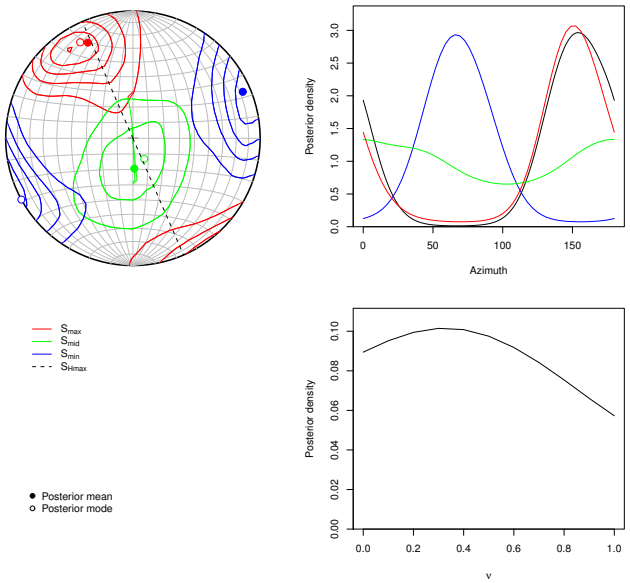

Figure A.28: Stress inversion result for cluster 31.

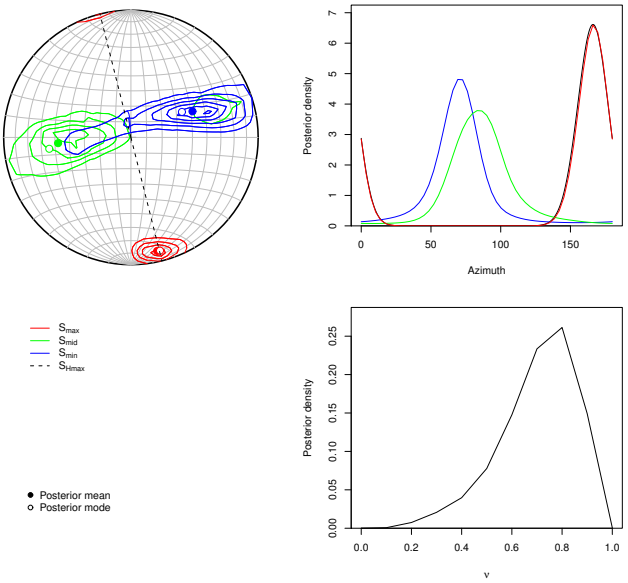

Figure A.29: Stress inversion result for cluster 32.

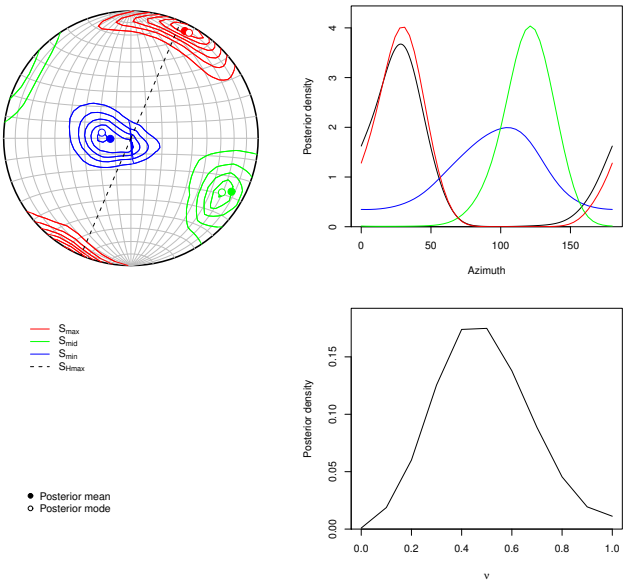

Figure A.30: Stress inversion result for cluster 33.

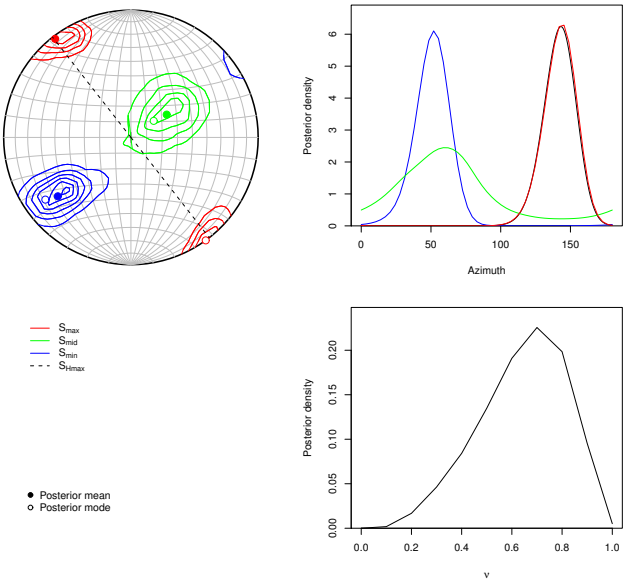

Figure A.31: Stress inversion result for cluster 34.

Appendix B

Splitting Results

This appendix includes a one-page figure summary of the splitting parameters observed at each station and a table of summary statistics for all stations. The summary figure includes: scatter plots of splitting parameters with depth and time, map of the station location and earthquakes used for shear-wave splitting, circle plot of the fast direction with back-azimuth and incidence angle (see Figure 4.7), and rose diagram of fast directions including the mean and standard deviation (see Figure 4.6). A description of each measurement can be found on the accompanying CD.

STA	Name of the station.
LAT	Latitude of the station.
LON	Longitude of the station.
ϕ	fast direction in degrees.
$\pm\phi$	standard deviation of the fast direction.
δt	Delay time in seconds.
$\pm\delta$t	standard deviation of the delay time

Table B.1: Mean and standard deviation of splitting results observed at each station.

STA	LAT	LON	ϕ	$\pm\phi$	δt	$\pm\delta$t
CBB	50.0328	-125.3653	27	42.4649	0.19	0.02
HNB	49.2745	-122.5792	25.9816	47.8183	0.06	0.04
NLLB	49.2274	-123.9881	-49.496	32.5483	0.07	0.05
SHB	49.5930	-123.8805	17.7904	25.8937	0.09	0.05
SNB	48.7760	-123.1712	-72.0681	35.0133	0.08	0.05
VGZ	48.4139	-123.3244	-35.0927	31.3787	0.11	0.05
LZB	48.6117	-123.8236	-43.3906	42.9752	0.09	0.04
PFB	48.5750	-124.4444	-54.8282	54.6866	0.19	0.15
MGB	49.0000	-124.6975	-59.3222	52.5206	0.09	0.06
OZB	48.9606	-125.4928	-58.4608	32.2482	0.10	0.05
EDB	49.8737	-127.1198	-59.7351	31.2486	0.10	0.05
PGC	48.6500	-123.4508	-41.6981	32.7683	0.12	0.07
YOUB	48.9009	-124.2618	-74.2044	44.9657	0.14	0.07
CLVB	49.3817	-123.1447	15.0553	19.9131	0.20	0.08
GHNB	49.30650	-124.23640	28.7058	38.1597	0.20	0.11
PHYB	49.08280	-123.84310	29.5522	48.6792	0.14	0.04
BMSB	48.83561	-125.13549	-24.2379	26.8659	0.14	0.06
TSJB	48.6013	-123.9885	-76.9205	37.0111	0.13	0.07
KHVB	48.56883	-123.46633	-49.0291	34.1024	0.18	0.11
SHVB	48.47232	-123.37375	-19.8055	29.7706	0.09	0.05
AHCB	48.93250	-123.73730	88.0012	2.16102	0.21	0.12
PIMB	49.2743	-122.6661	-2.48538	25.0751	0.11	0.04
ENGB	49.0080	-123.0889	-64.9981	11.9923	0.10	0.03
TOFB	49.1543	-125.9078	-66	90	0.08	0.02
BTB	49.4683	-125.5214	-20.5683	63.6489	0.20	0.05
THAB	49.28000	-124.91840	29.5369	24.6273	0.14	0.05
SOKB	48.3947	-123.67314	-75.3917	30.8366	0.08	0.04
CPLB	48.61181	-124.75119	-26.5	2.50159	0.14	0.06
JRBC	48.35872	-123.96005	82	6.02215	0.09	0.05
GOWB	48.7369	-123.1848	-65.2299	22.9152	0.12	0.06
SILB	48.6019	-123.2814	-51.6703	38.1055	0.11	0.05
SSIB	48.7558	-123.3875	-70.3348	24.6105	0.12	0.06
TWGB	48.6076	-124.2559	-36.497	30.6937	0.13	0.06
TWKB	48.6449	-123.7332	-57.2818	32.5737	0.14	0.08

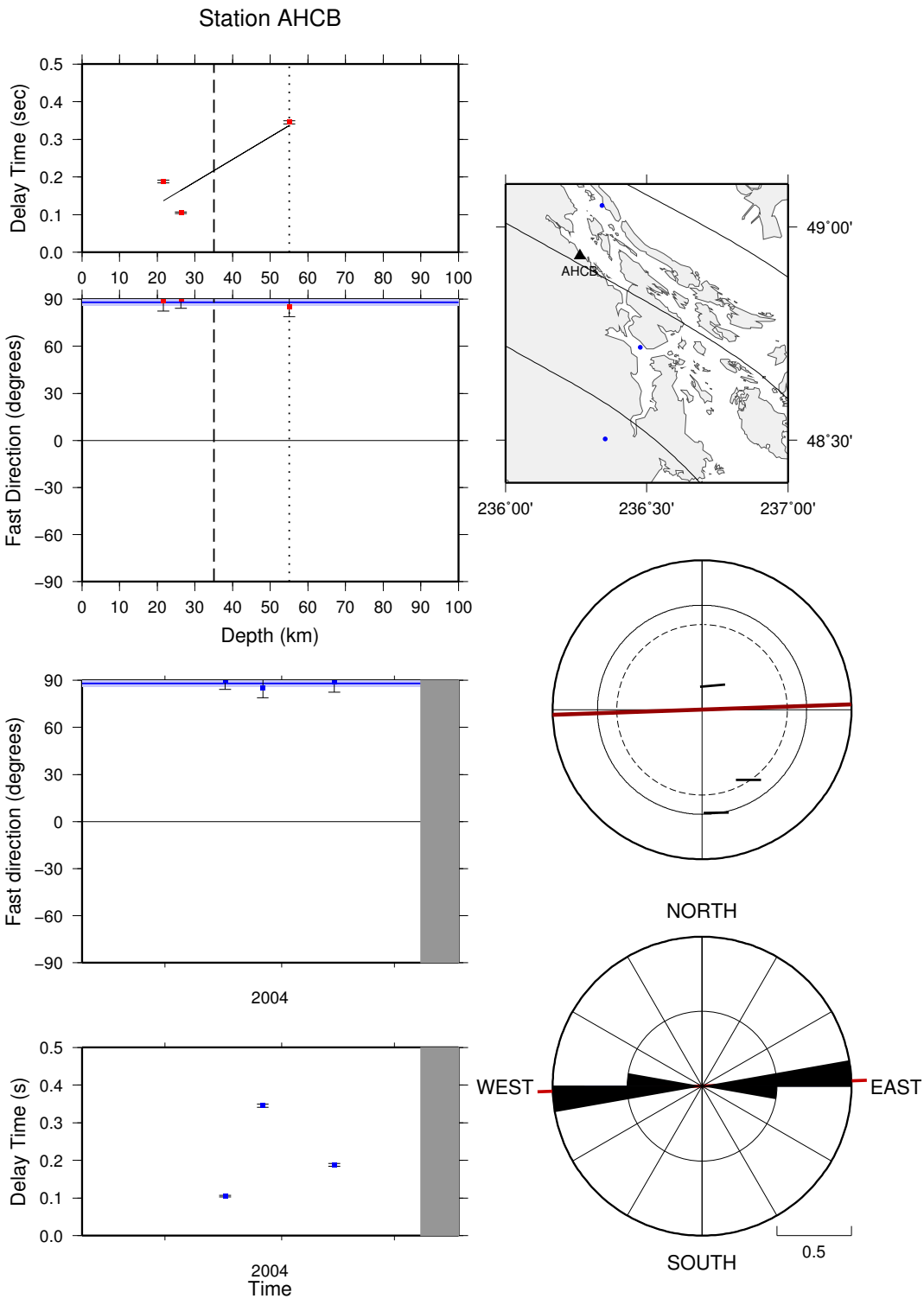

Figure B.1: Summary plots of shear-wave splitting results at station AHCB.

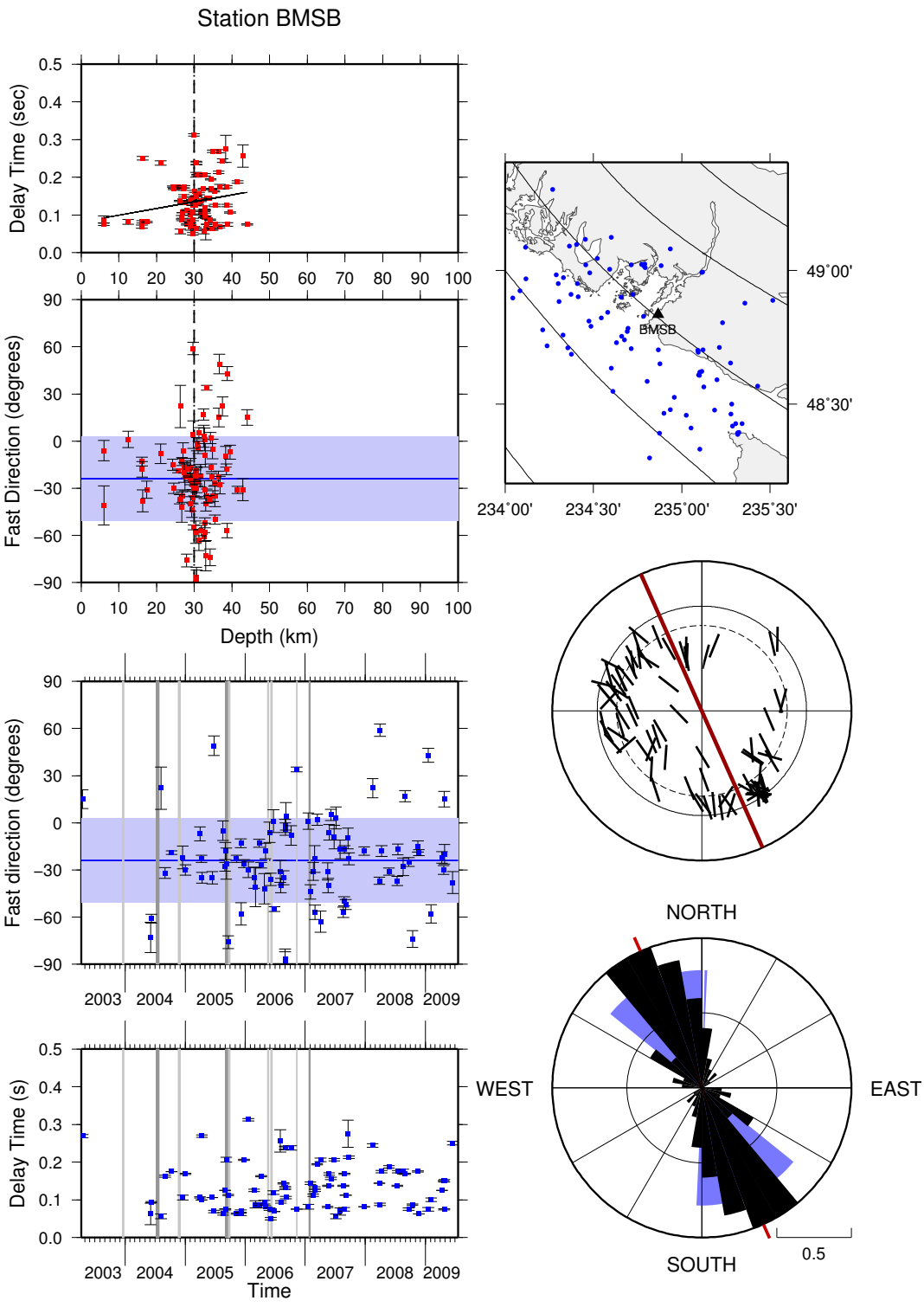

Figure B.2: Summary plots of shear-wave splitting results at station BMSB.

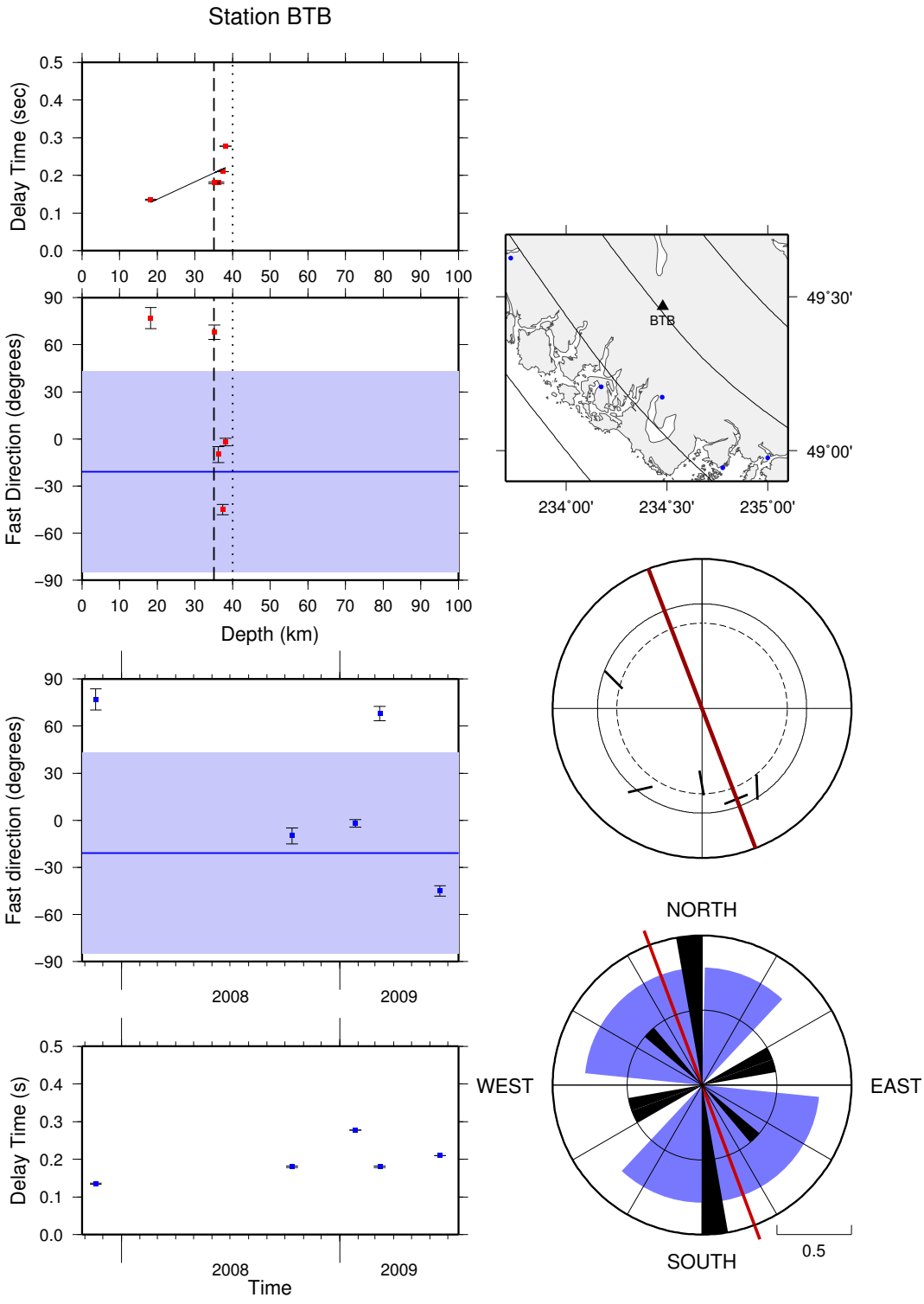

Figure B.3: Summary plots of shear-wave splitting results at station BTB.

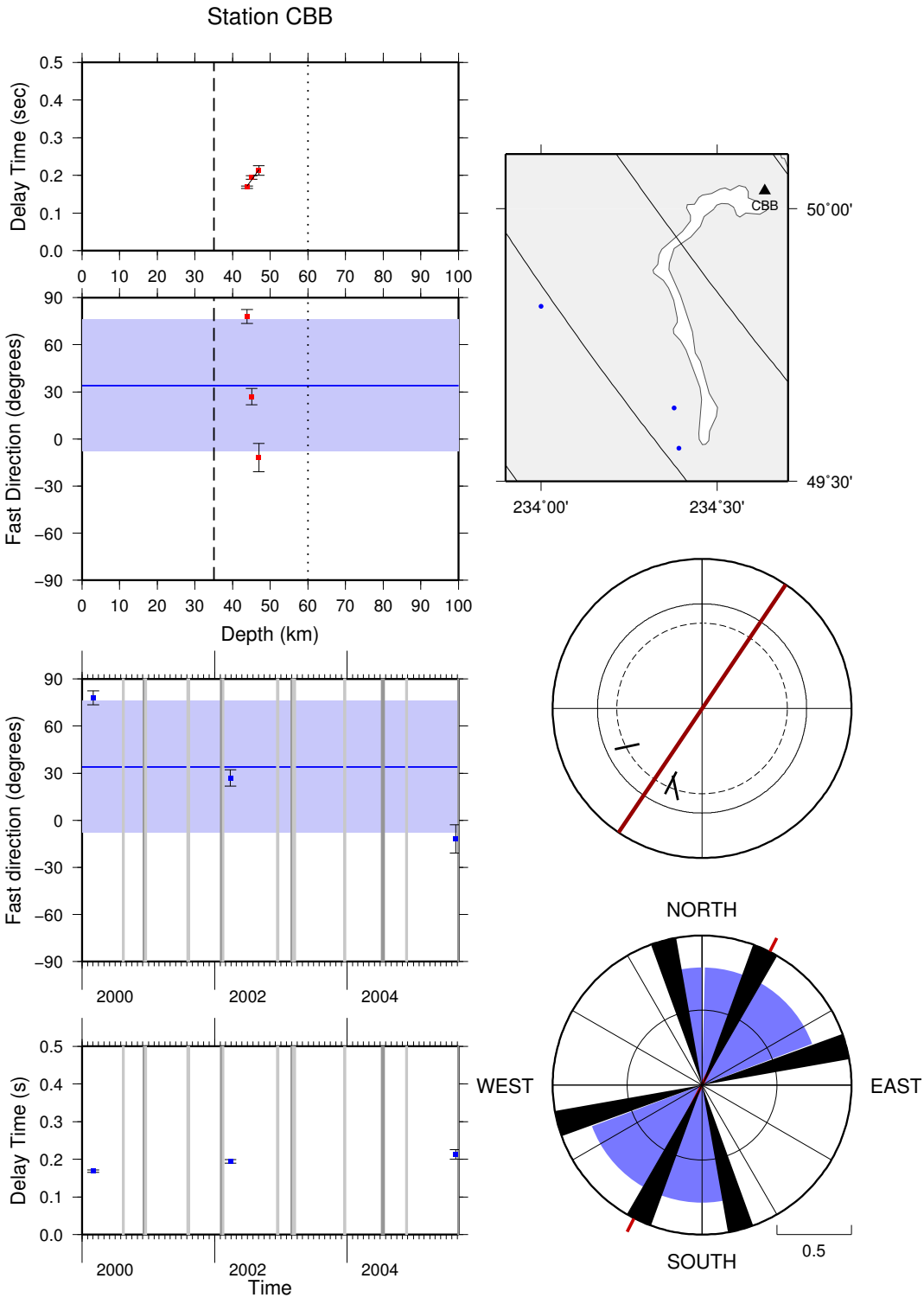

Figure B.4: Summary plots of shear-wave splitting results at station CBB.

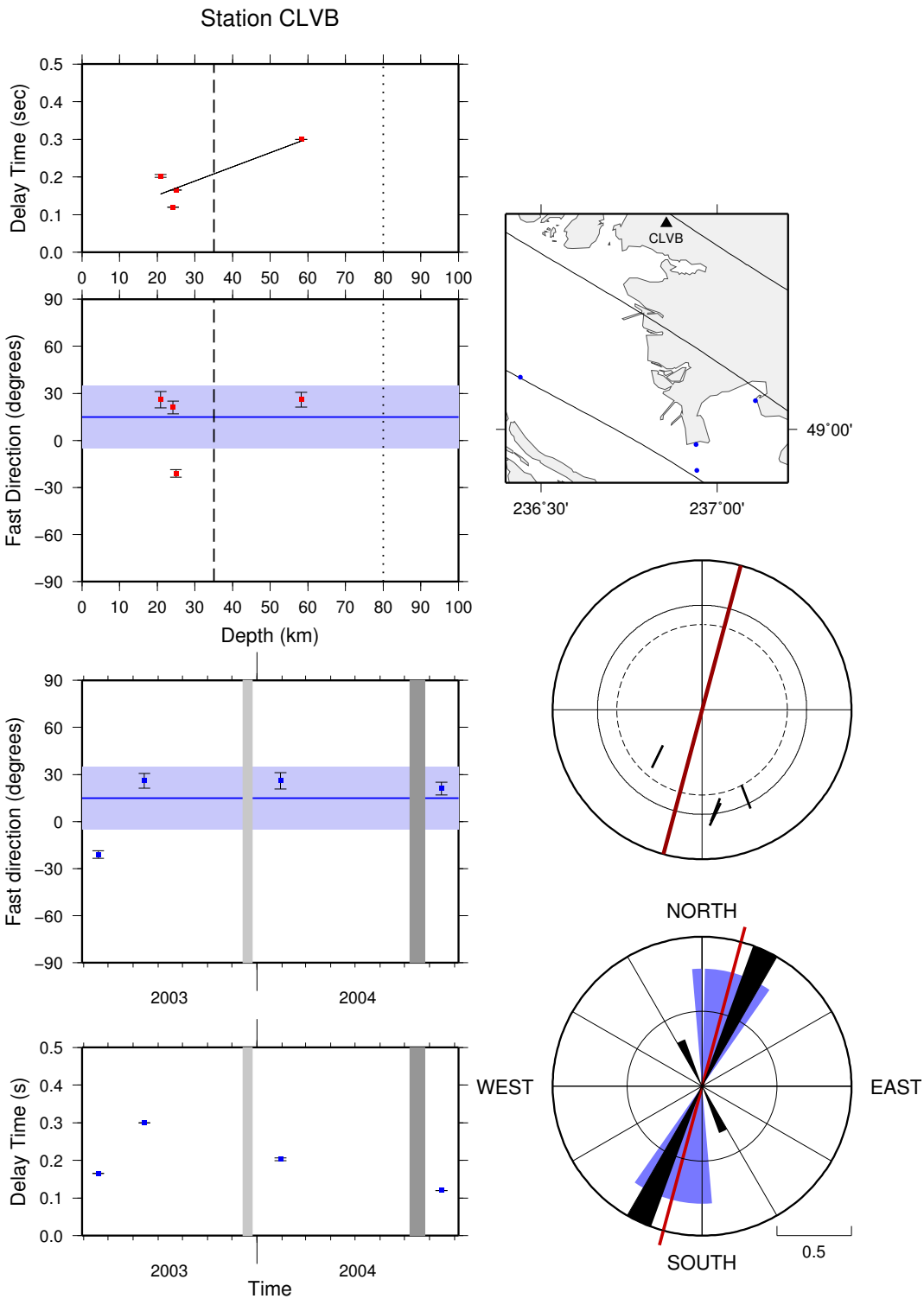

Figure B.5: Summary plots of shear-wave splitting results at station CLVB.

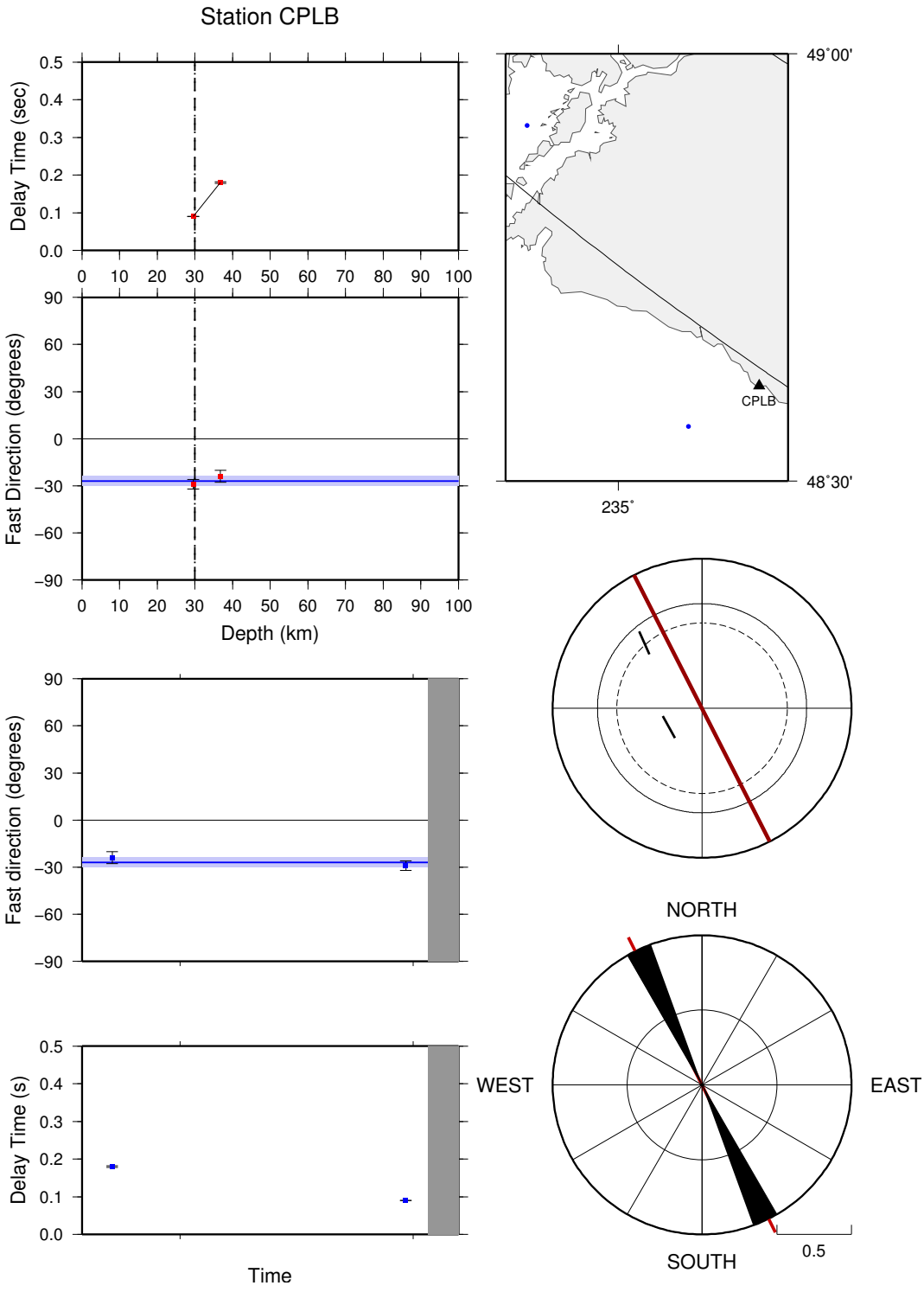

Figure B.6: Summary plots of shear-wave splitting results at station CPLB.

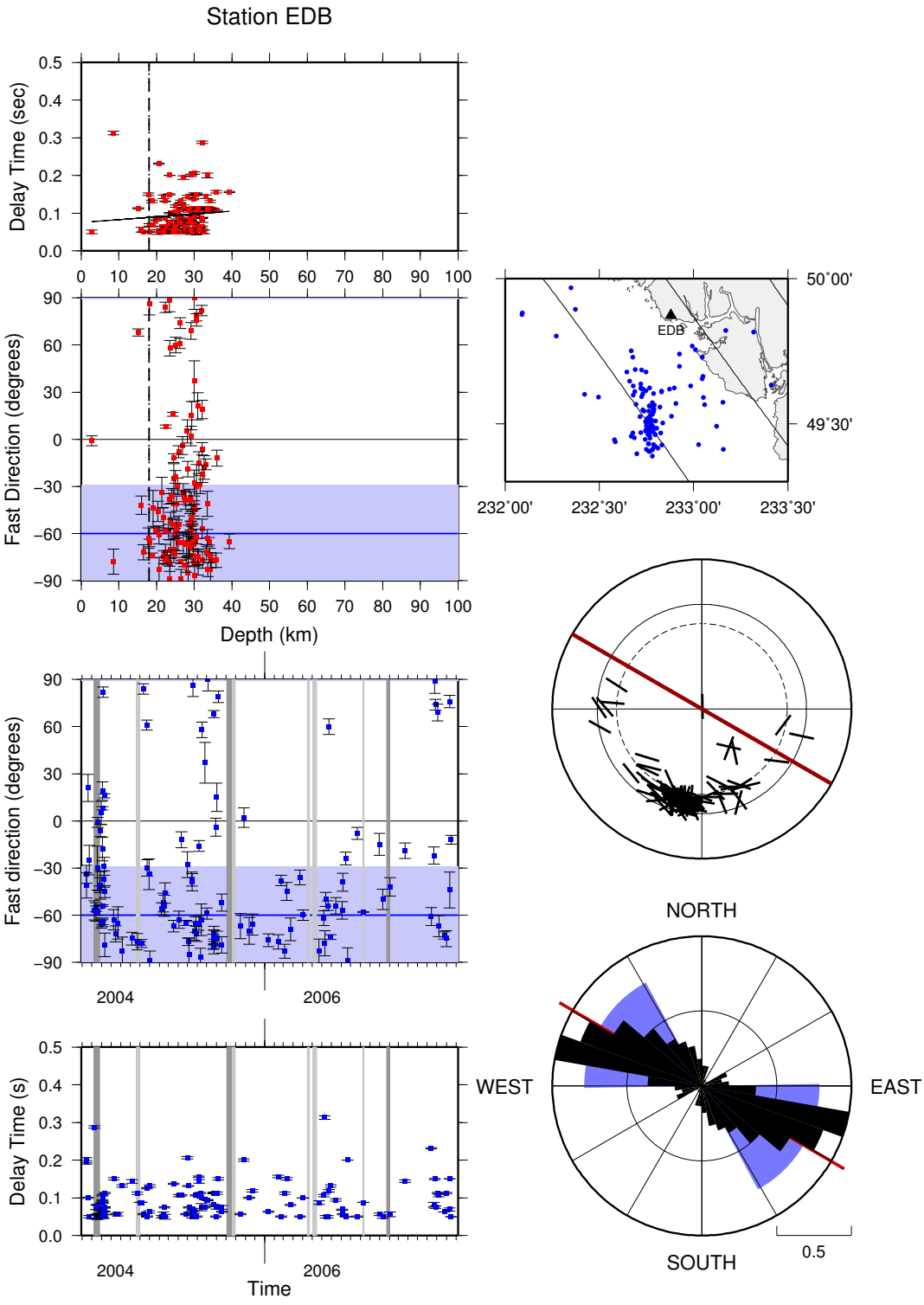

Figure B.7: Summary plots of shear-wave splitting results at station EDB.

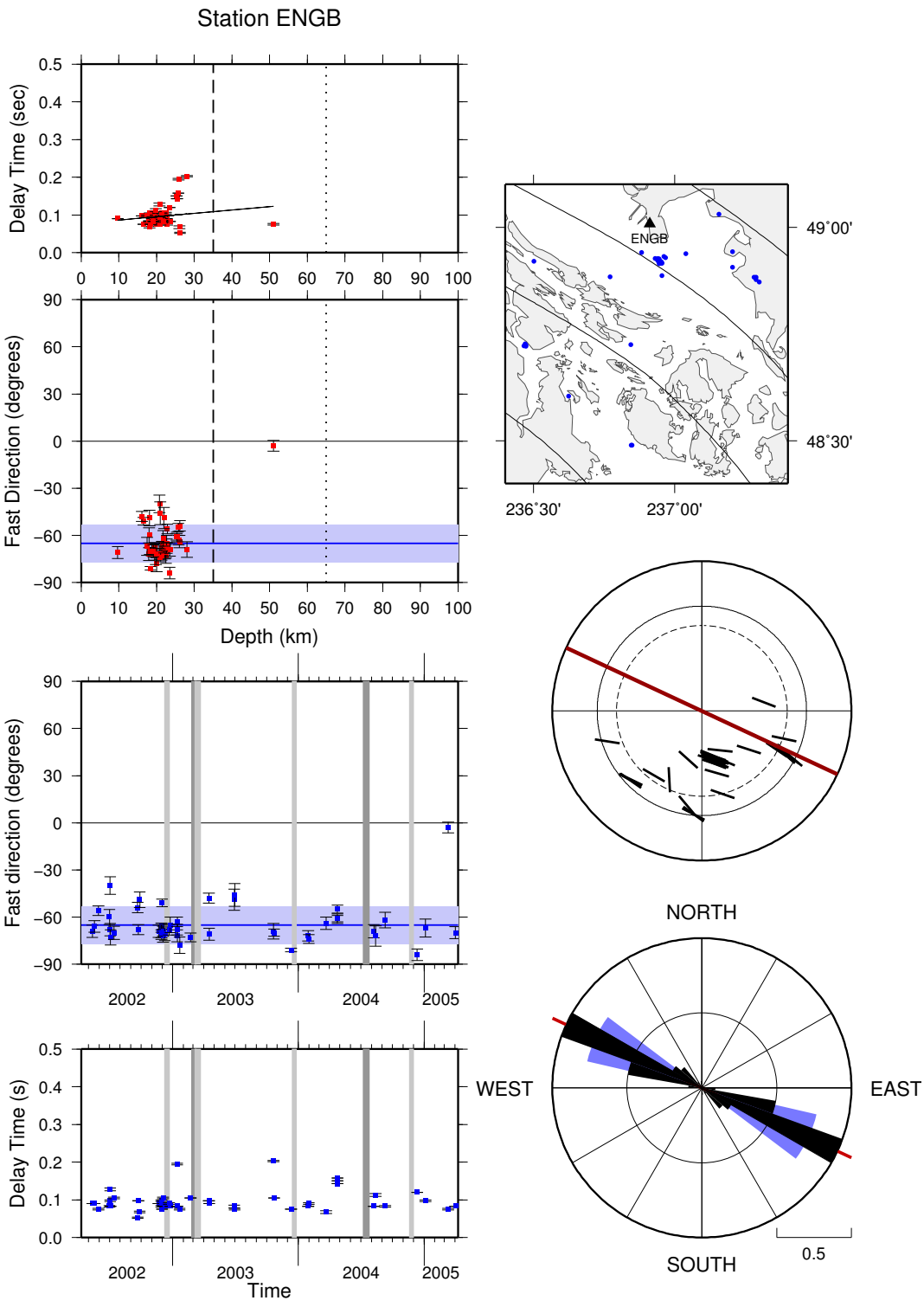

Figure B.8: Summary plots of shear-wave splitting results at station ENGB.

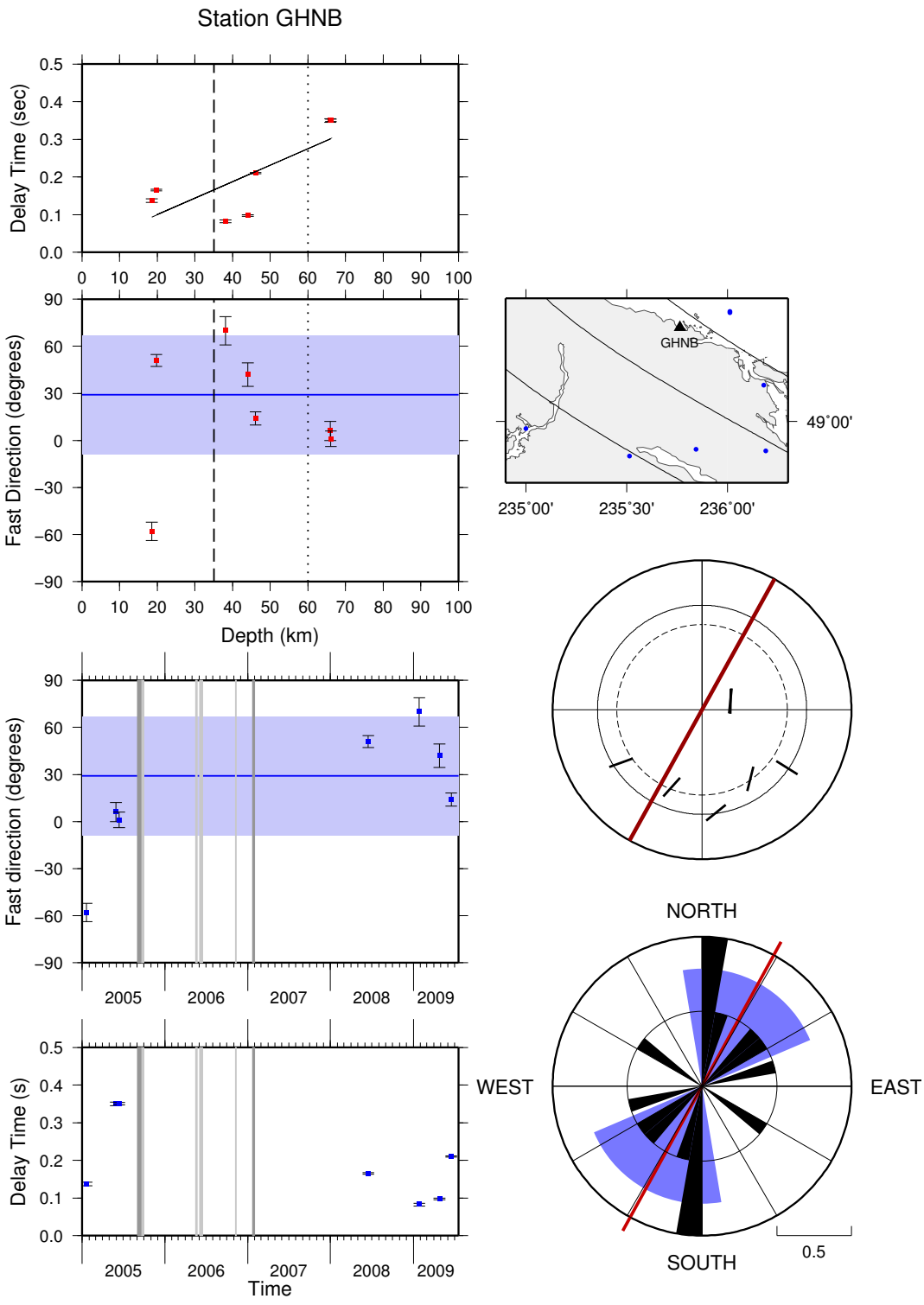

Figure B.9: Summary plots of shear-wave splitting results at station GNHB.

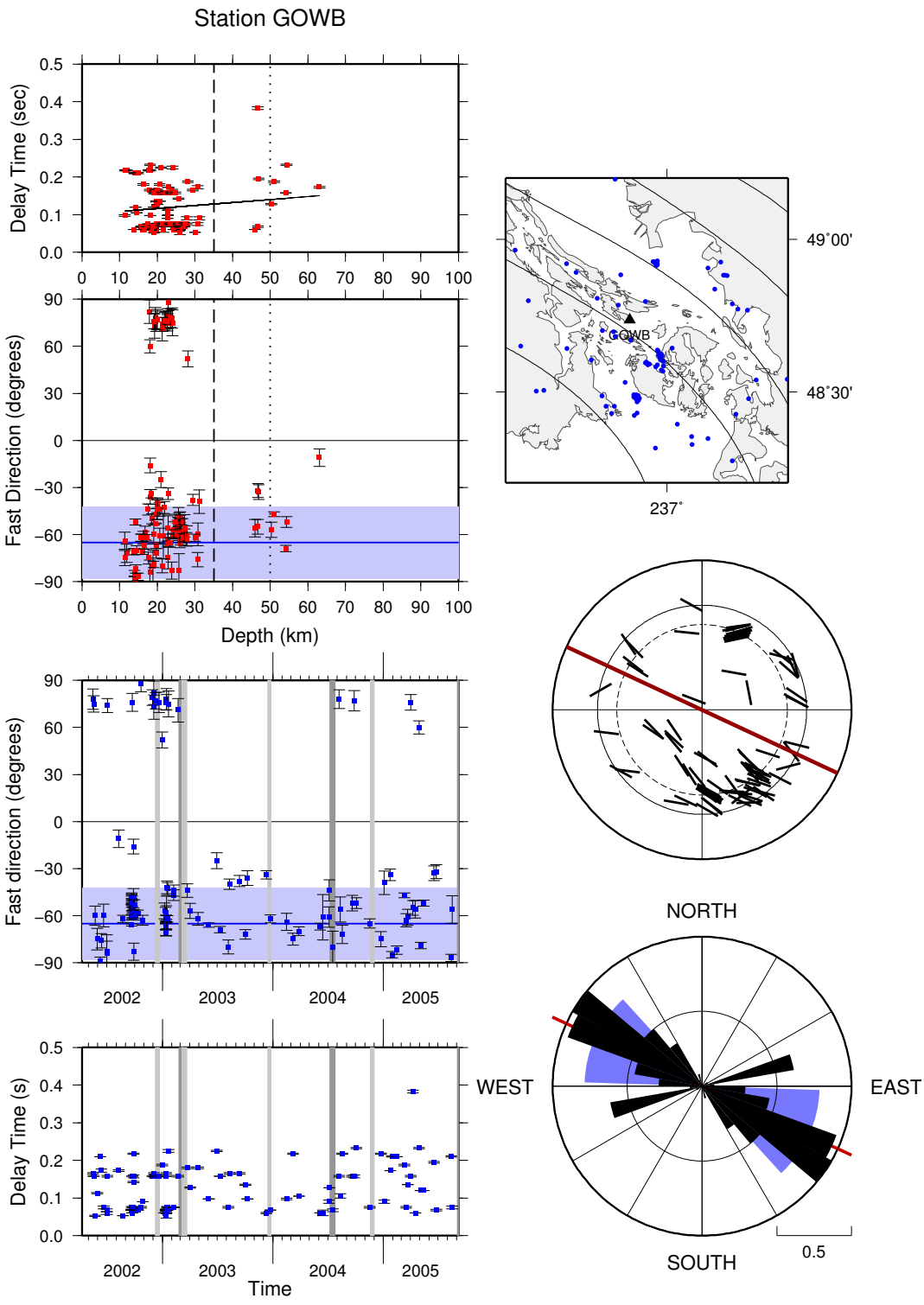

Figure B.10: Summary plots of shear-wave splitting results at station GOWB.

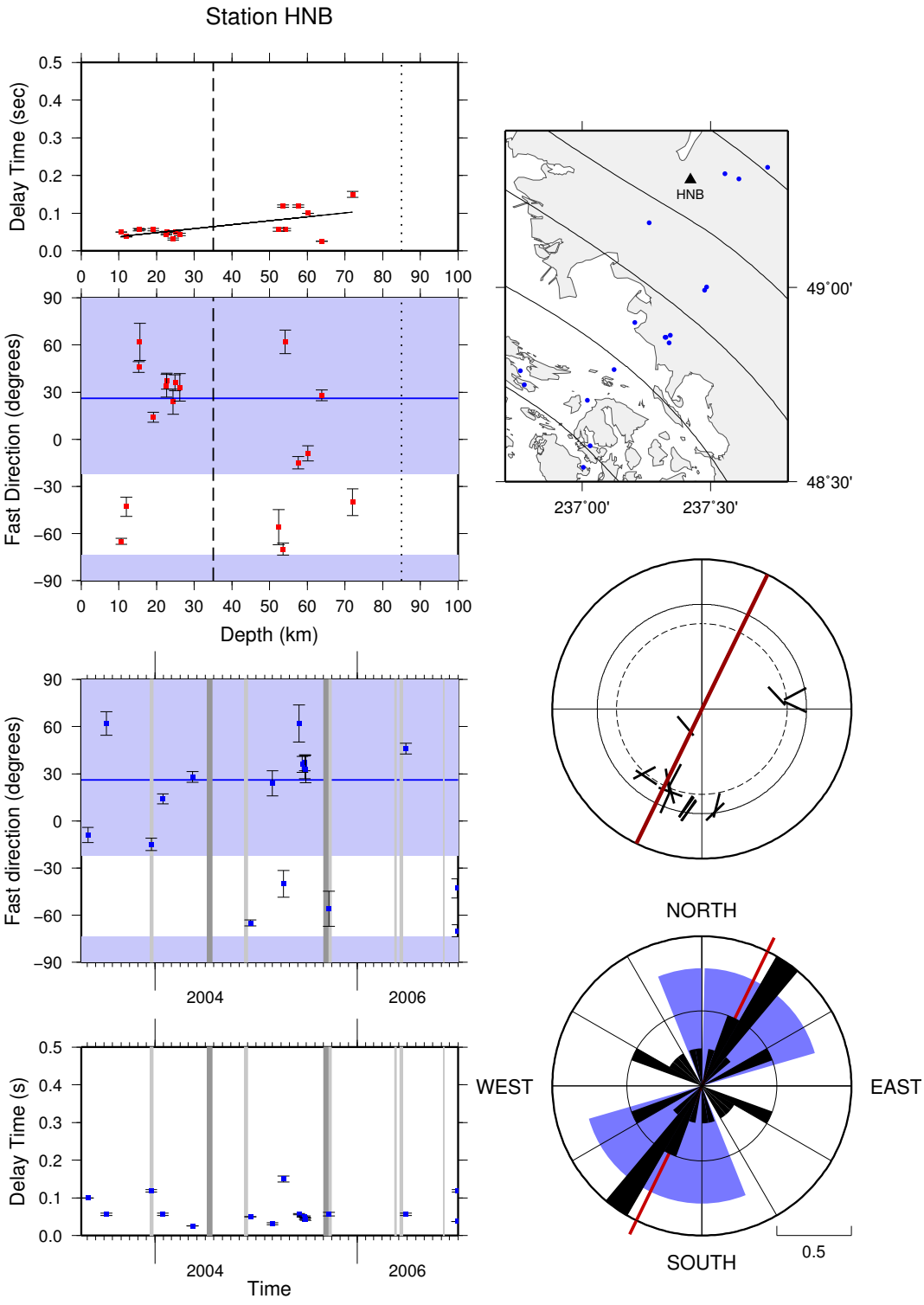

Figure B.11: Summary plots of shear-wave splitting results at station HNB.

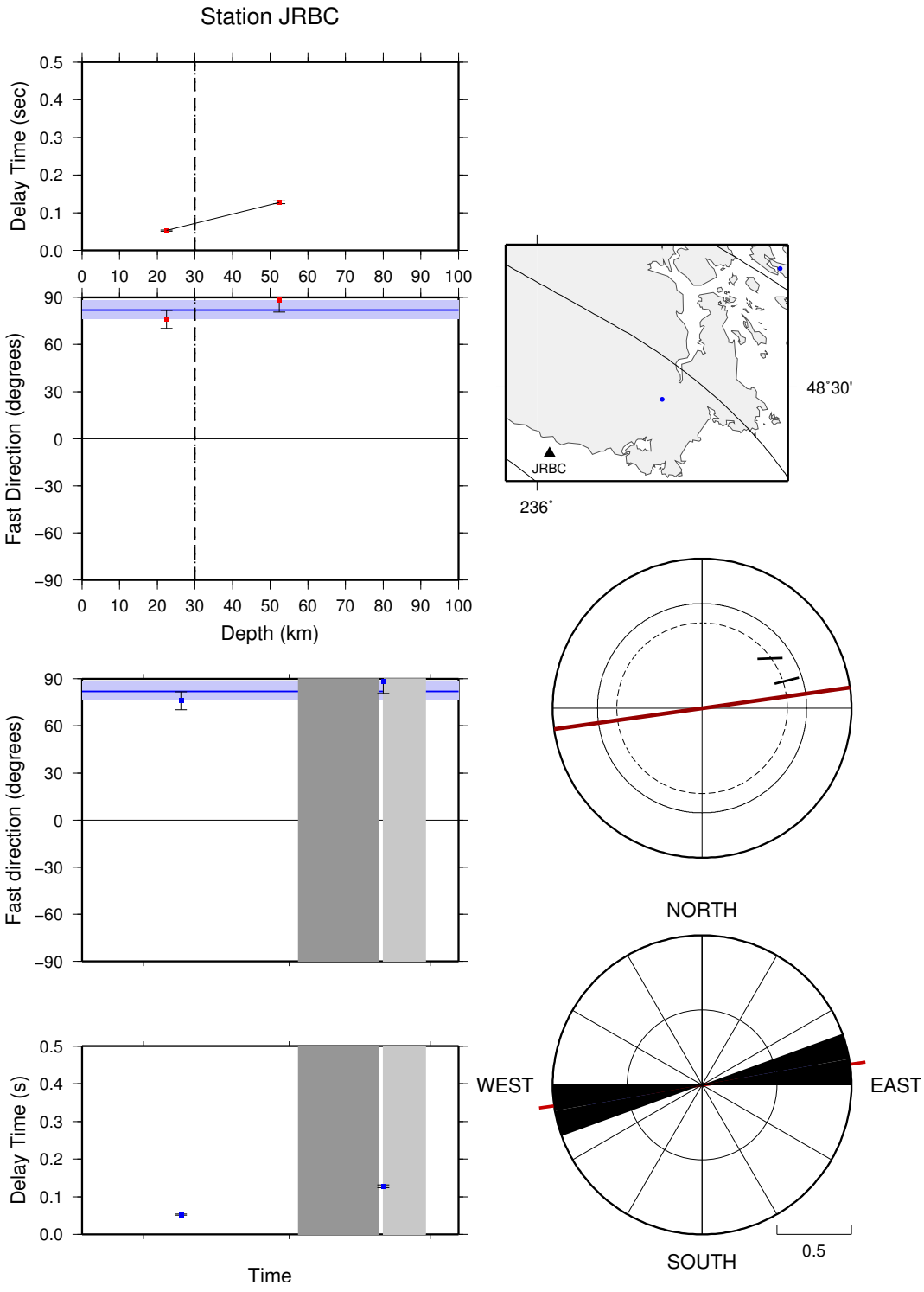

Figure B.12: Summary plots of shear-wave splitting results at station JRBC.

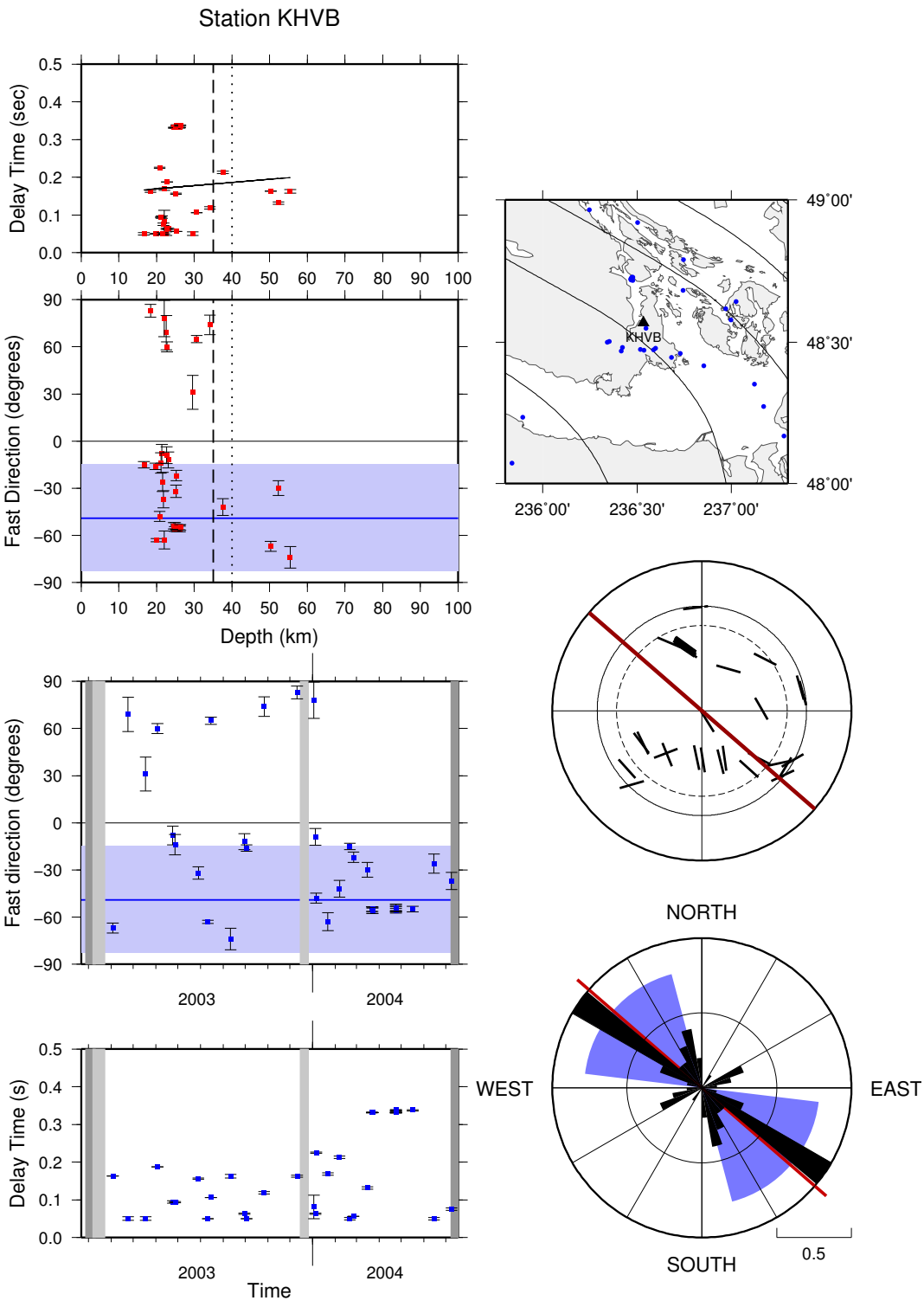

Figure B.13: Summary plots of shear-wave splitting results at station KHVB.

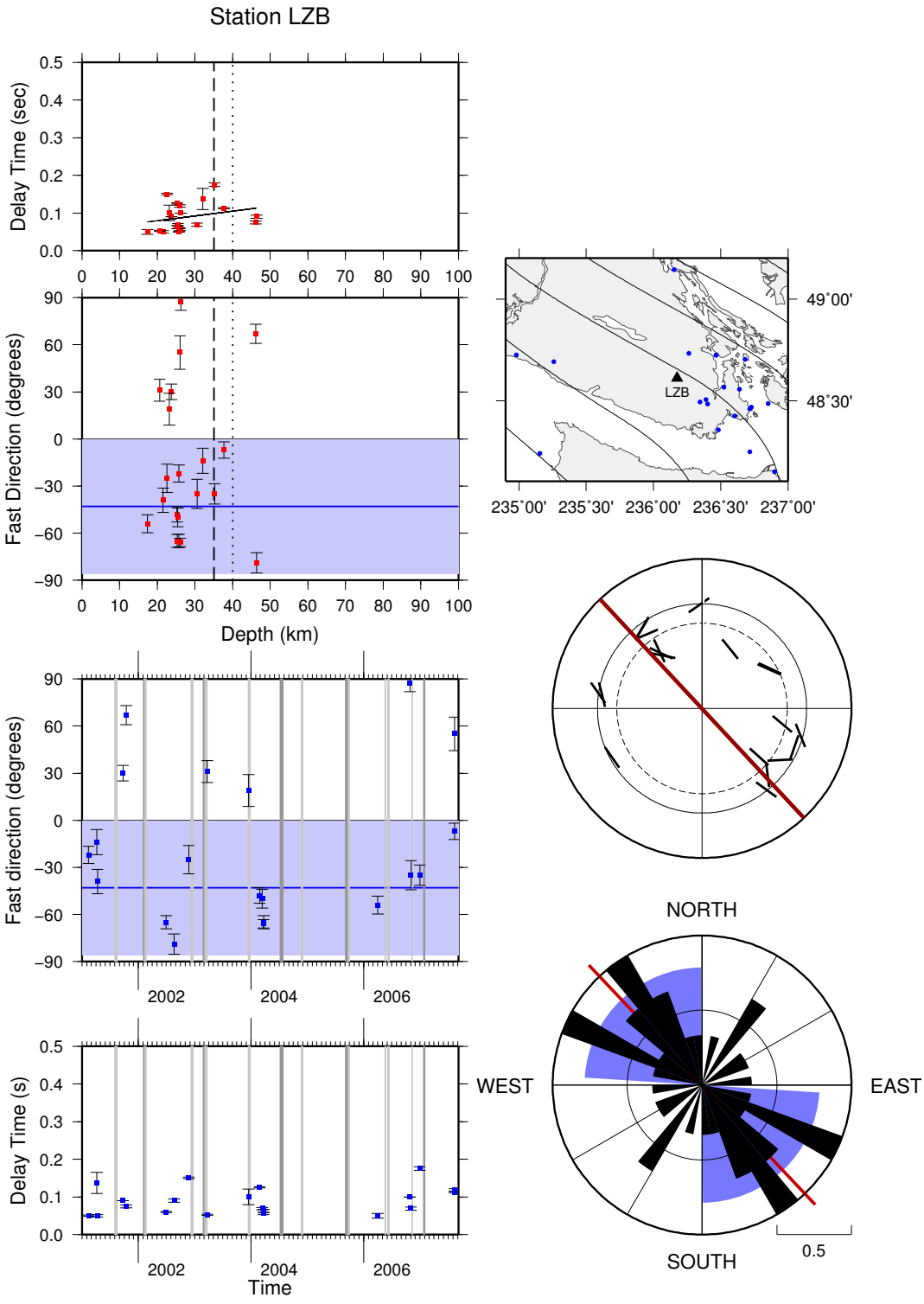

Figure B.14: Summary plots of shear-wave splitting results at station LZB.

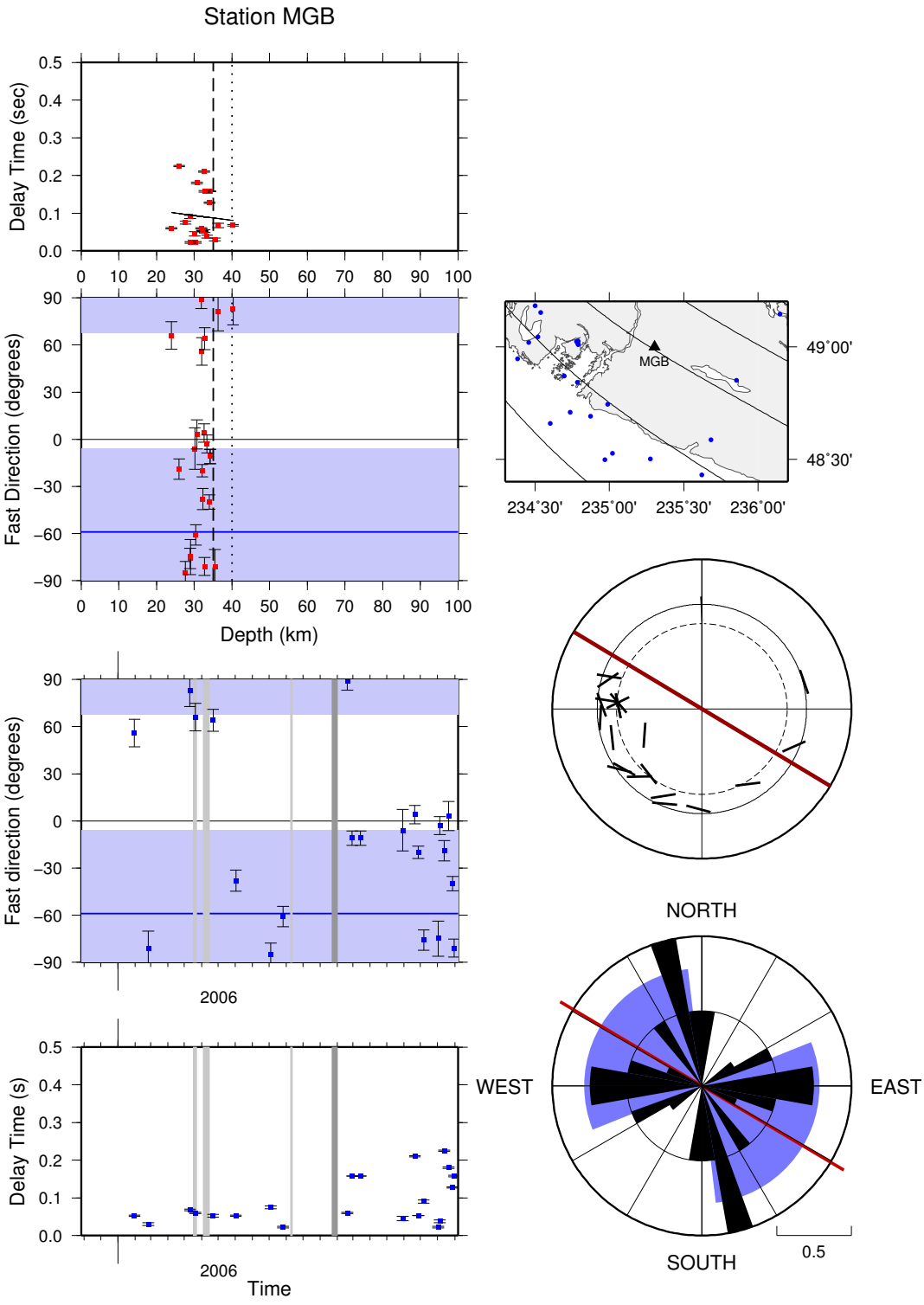

Figure B.15: Summary plots of shear-wave splitting results at station MGB.

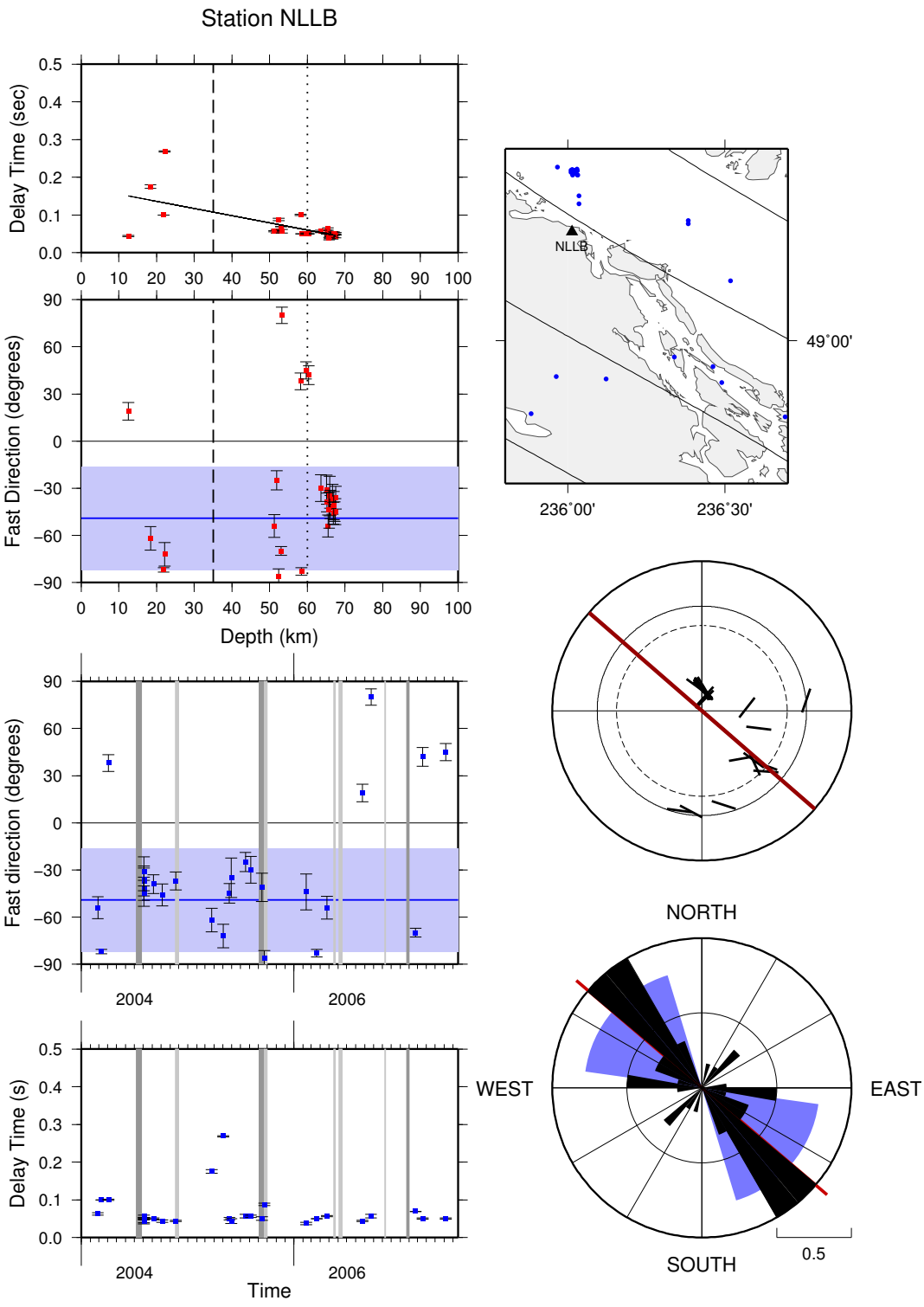

Figure B.16: Summary plots of shear-wave splitting results at station NLLB.

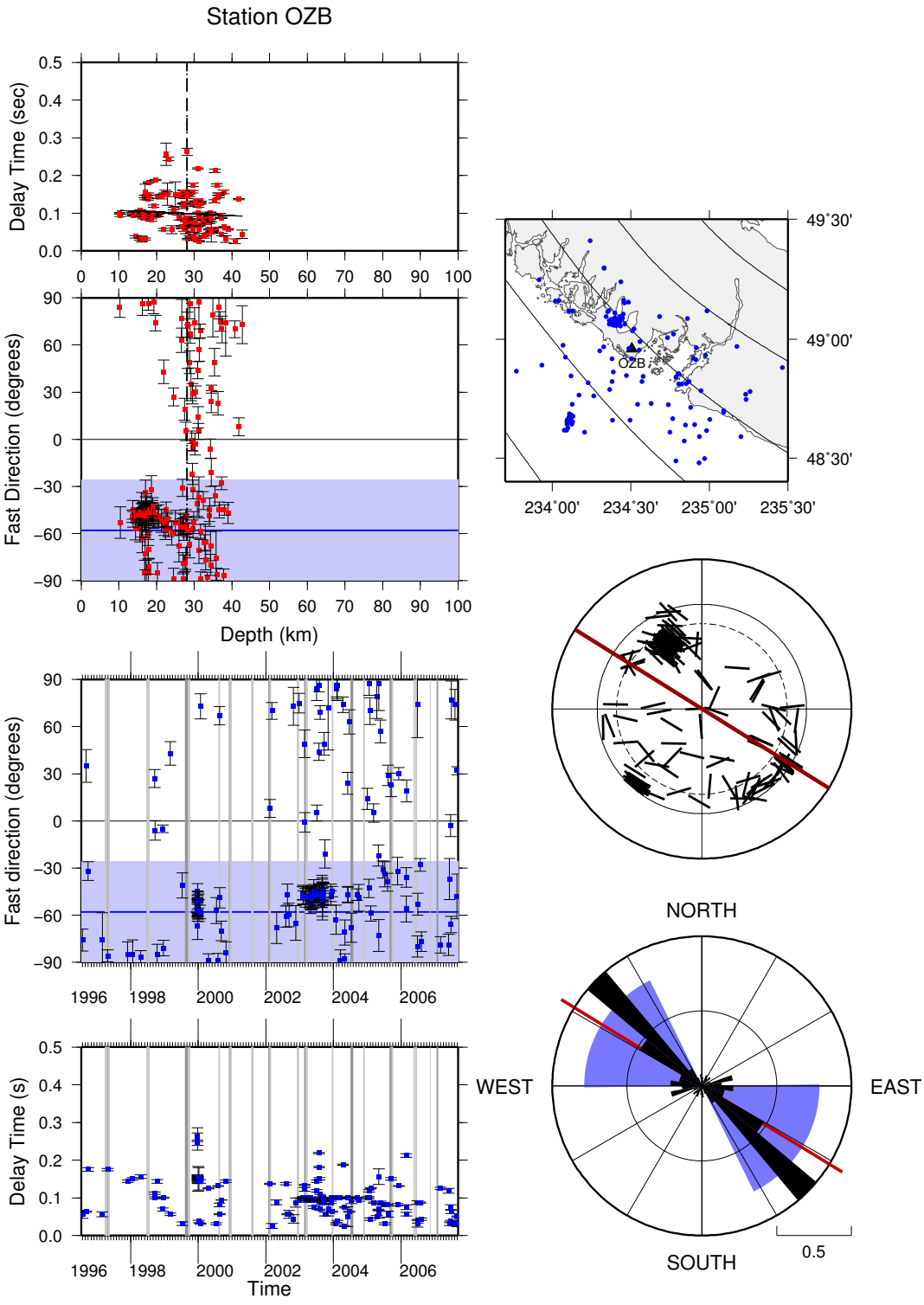

Figure B.17: Summary plots of shear-wave splitting results at station OZB.

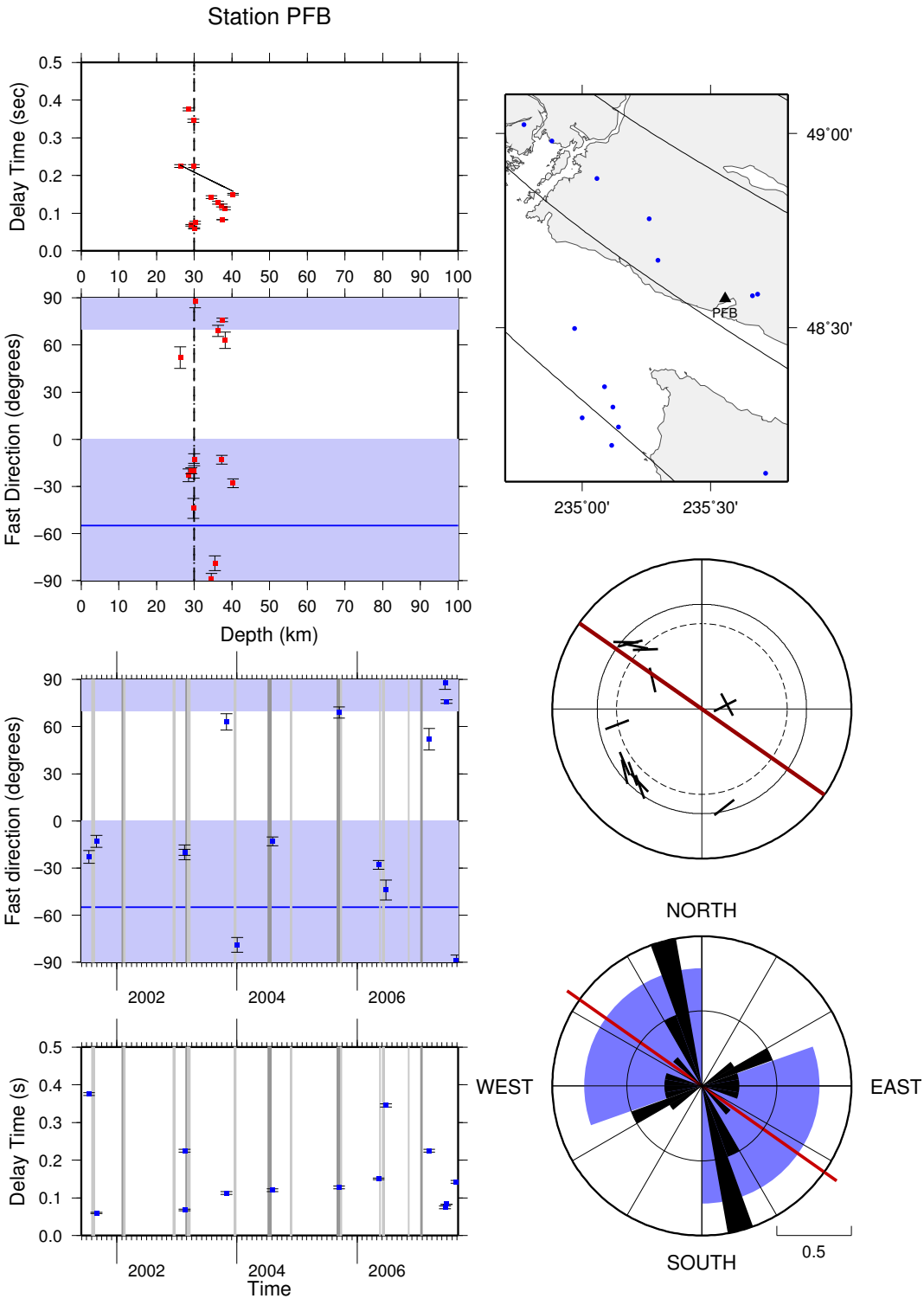

Figure B.18: Summary plots of shear-wave splitting results at station PFB.

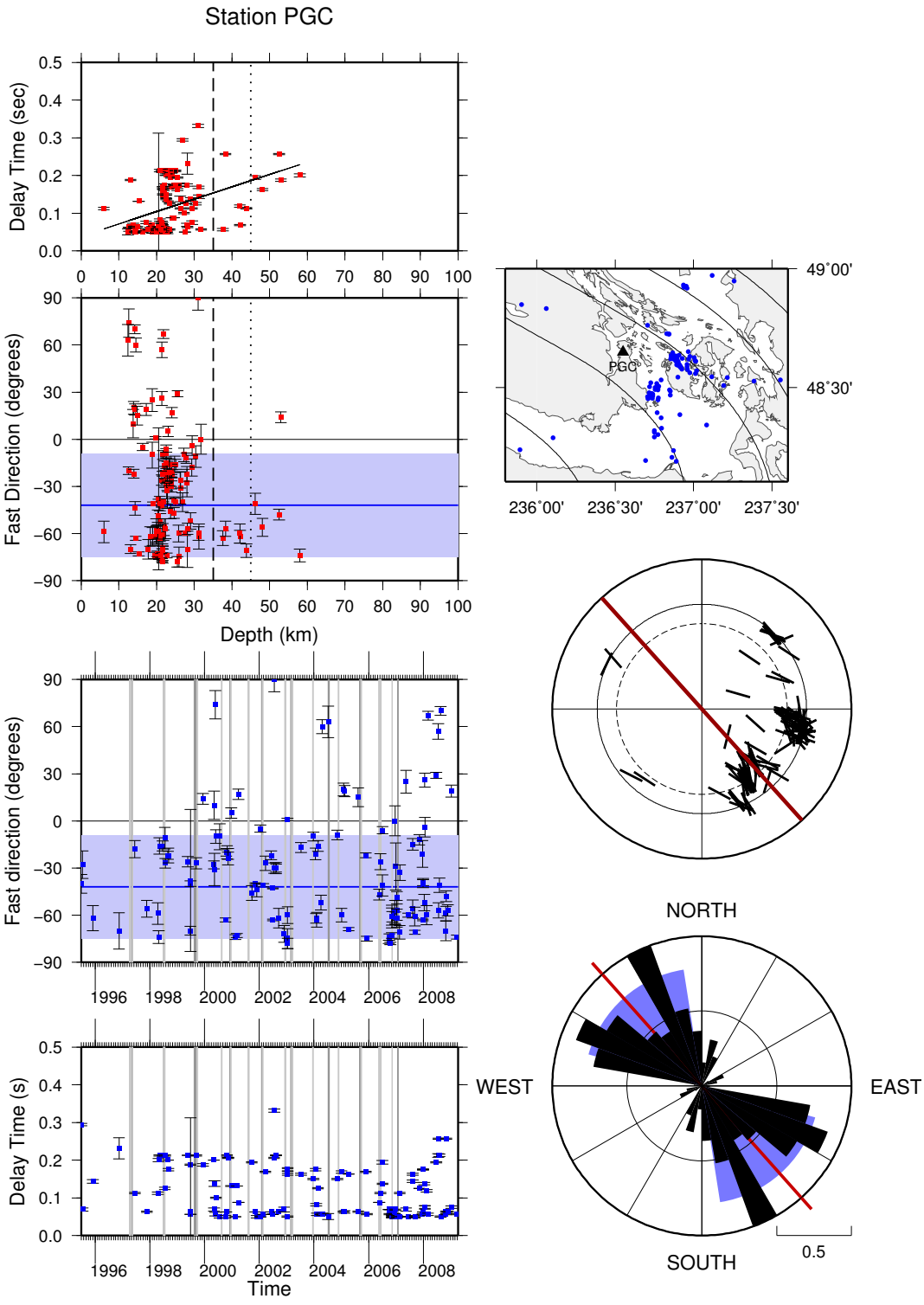

Figure B.19: Summary plots of shear-wave splitting results at station PGC.

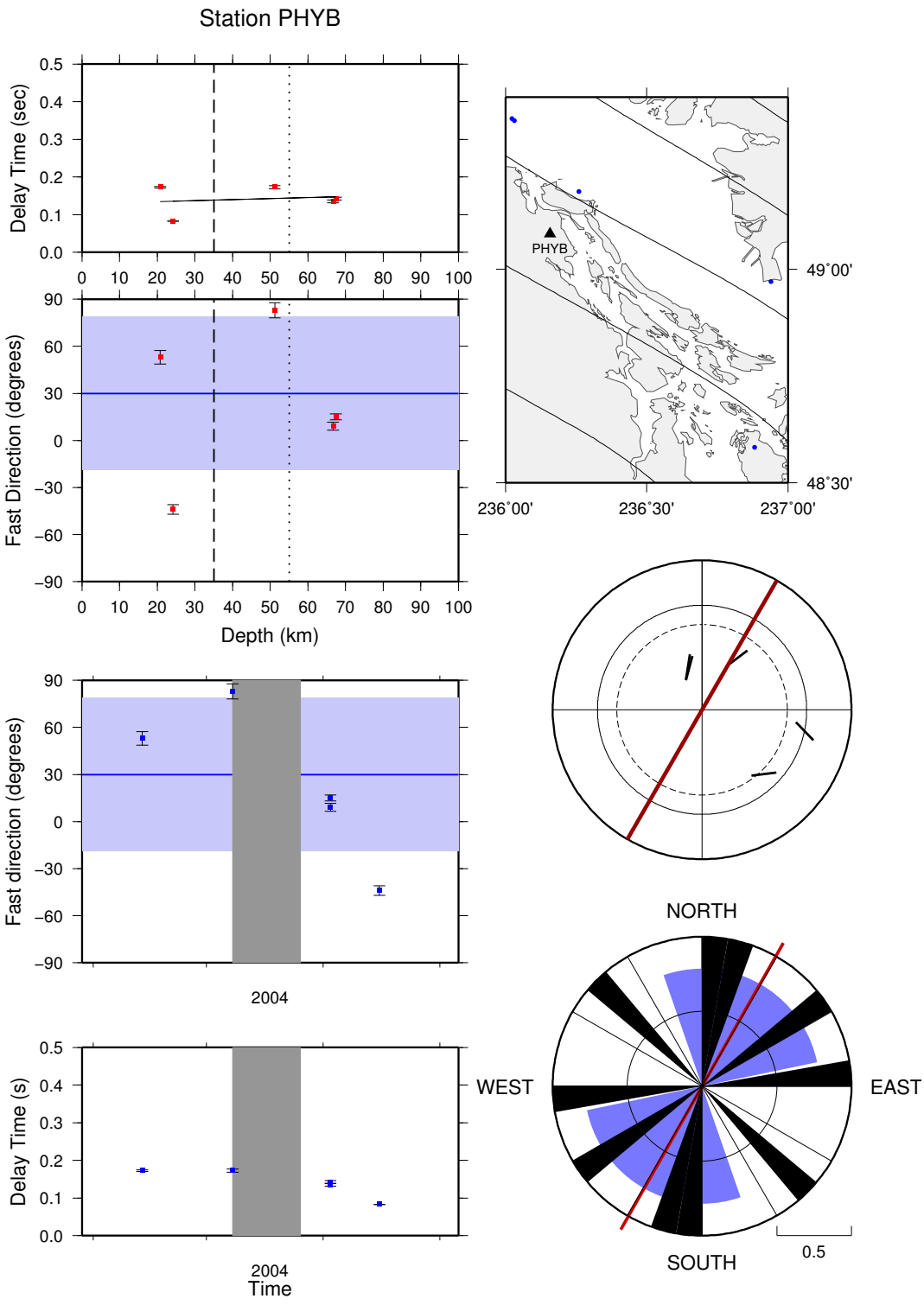

Figure B.20: Summary plots of shear-wave splitting results at station PHYB.

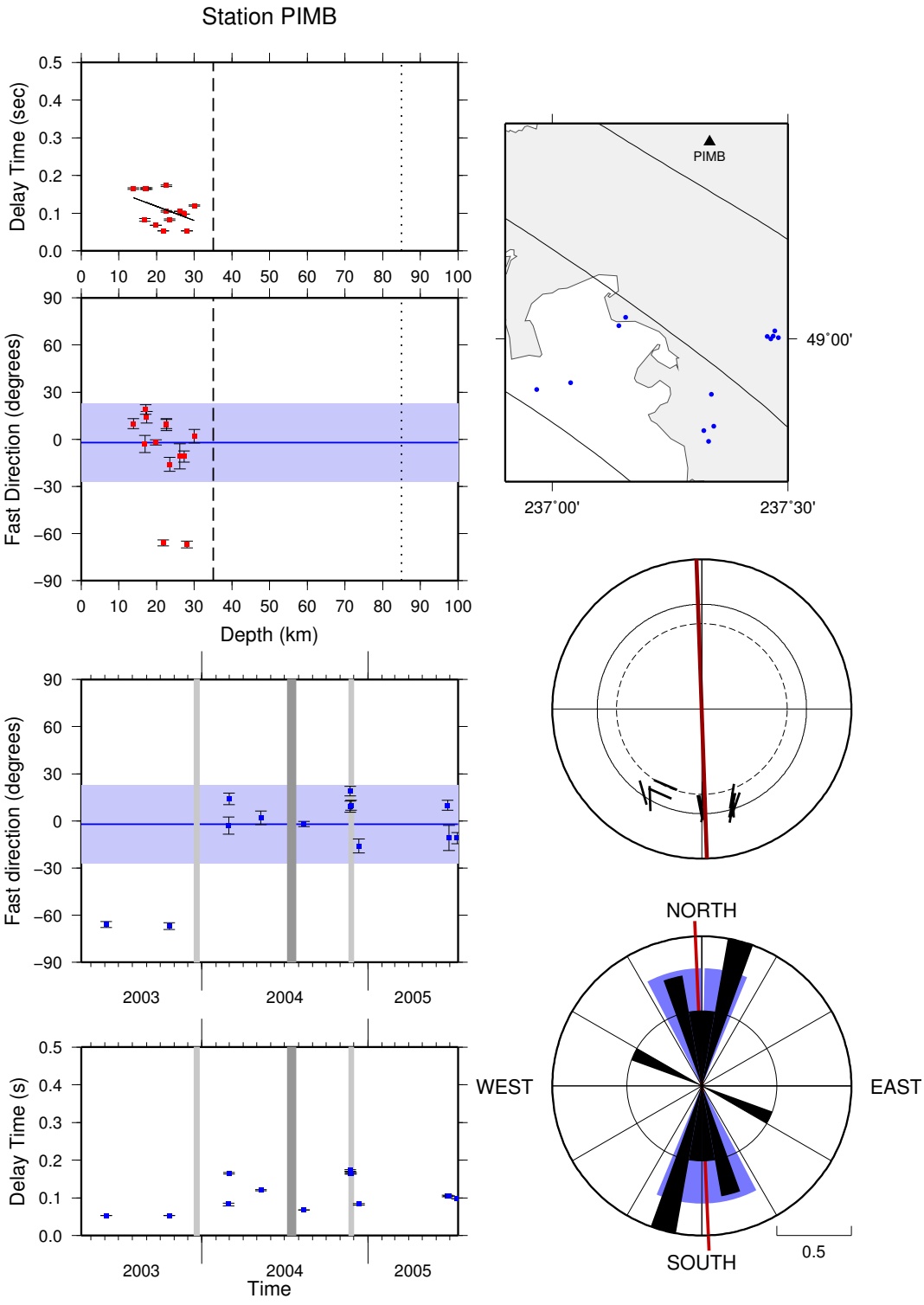

Figure B.21: Summary plots of shear-wave splitting results at station PIMB.

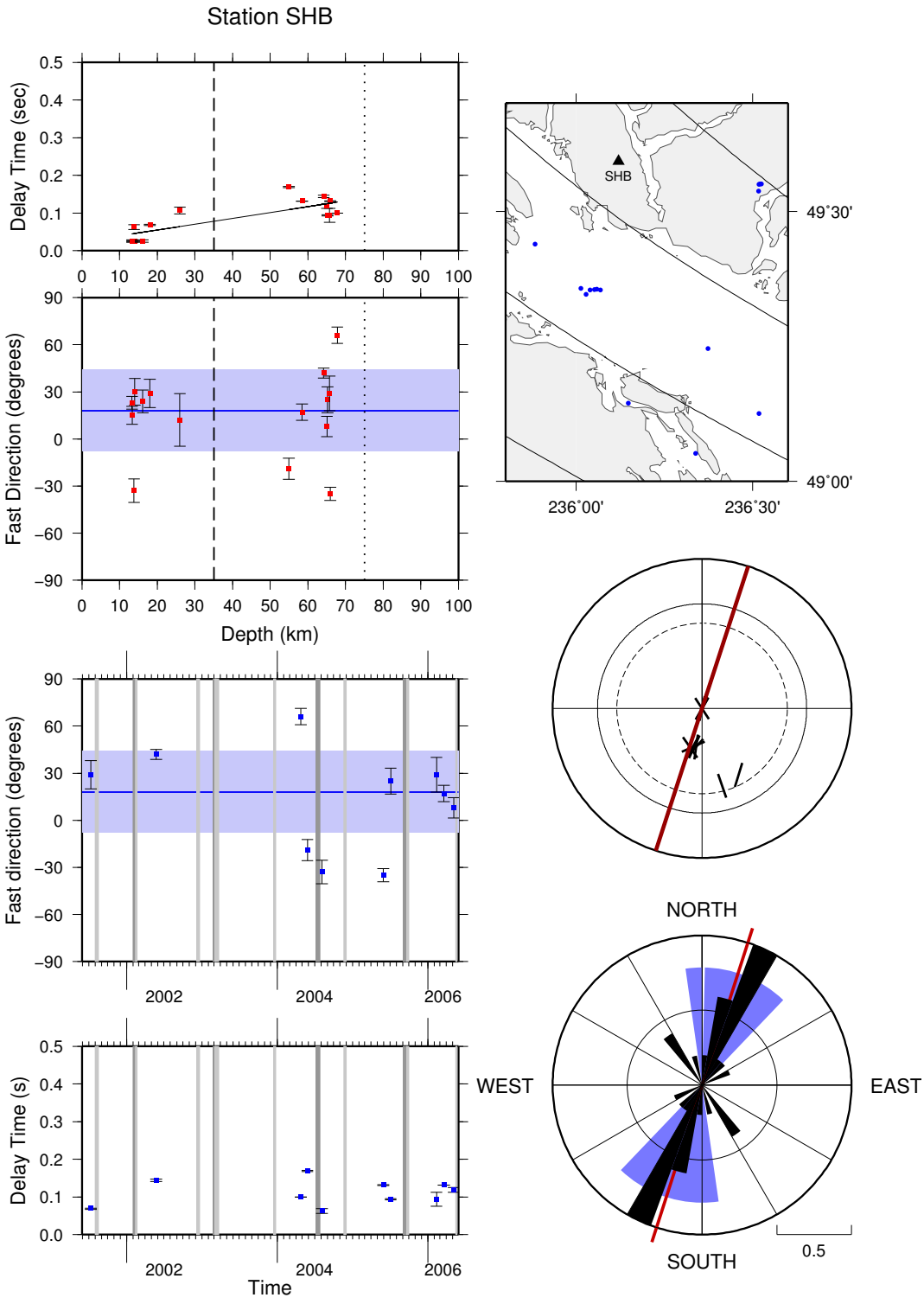

Figure B.22: Summary plots of shear-wave splitting results at station SHB.

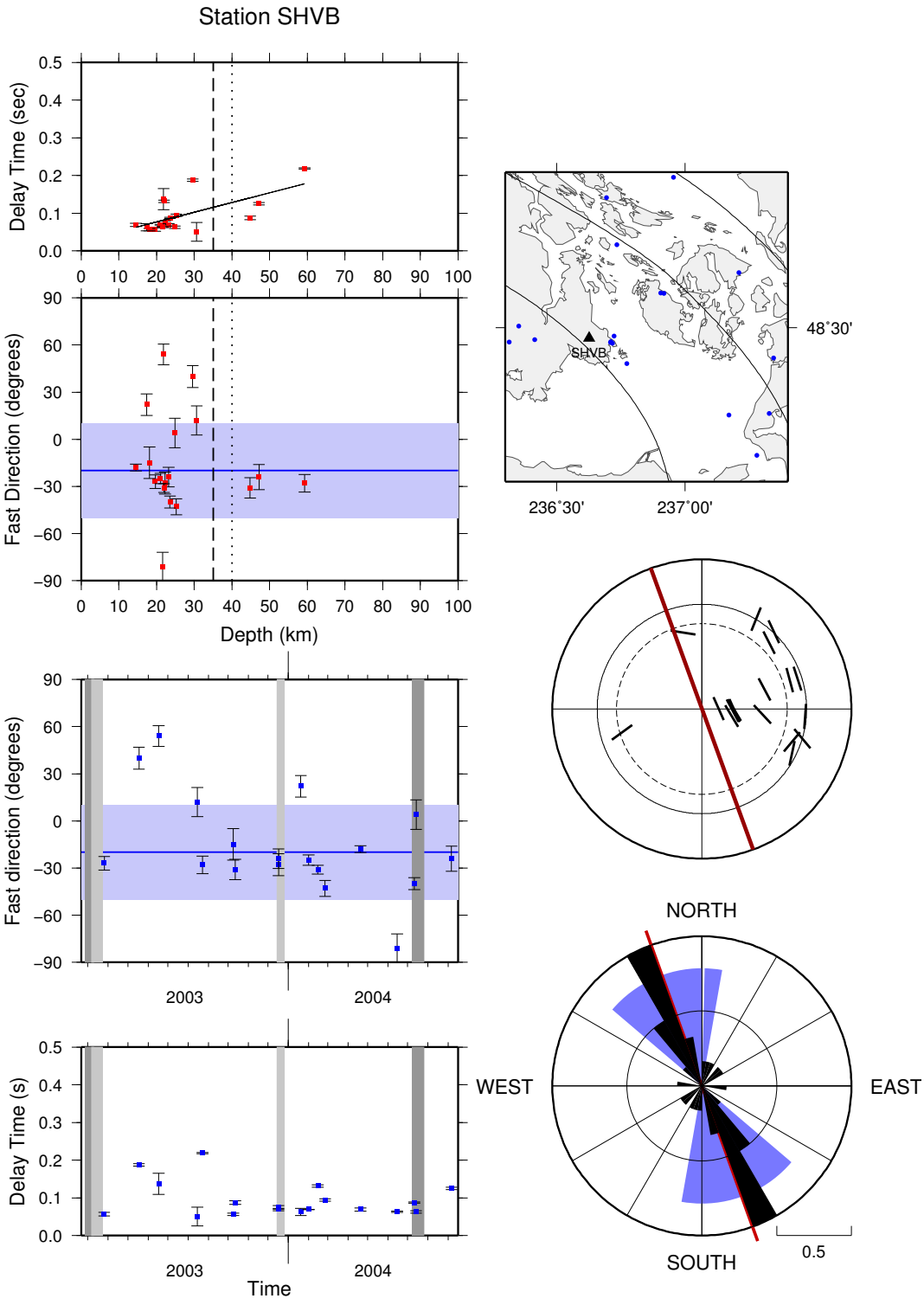

Figure B.23: Summary plots of shear-wave splitting results at station SHVB.

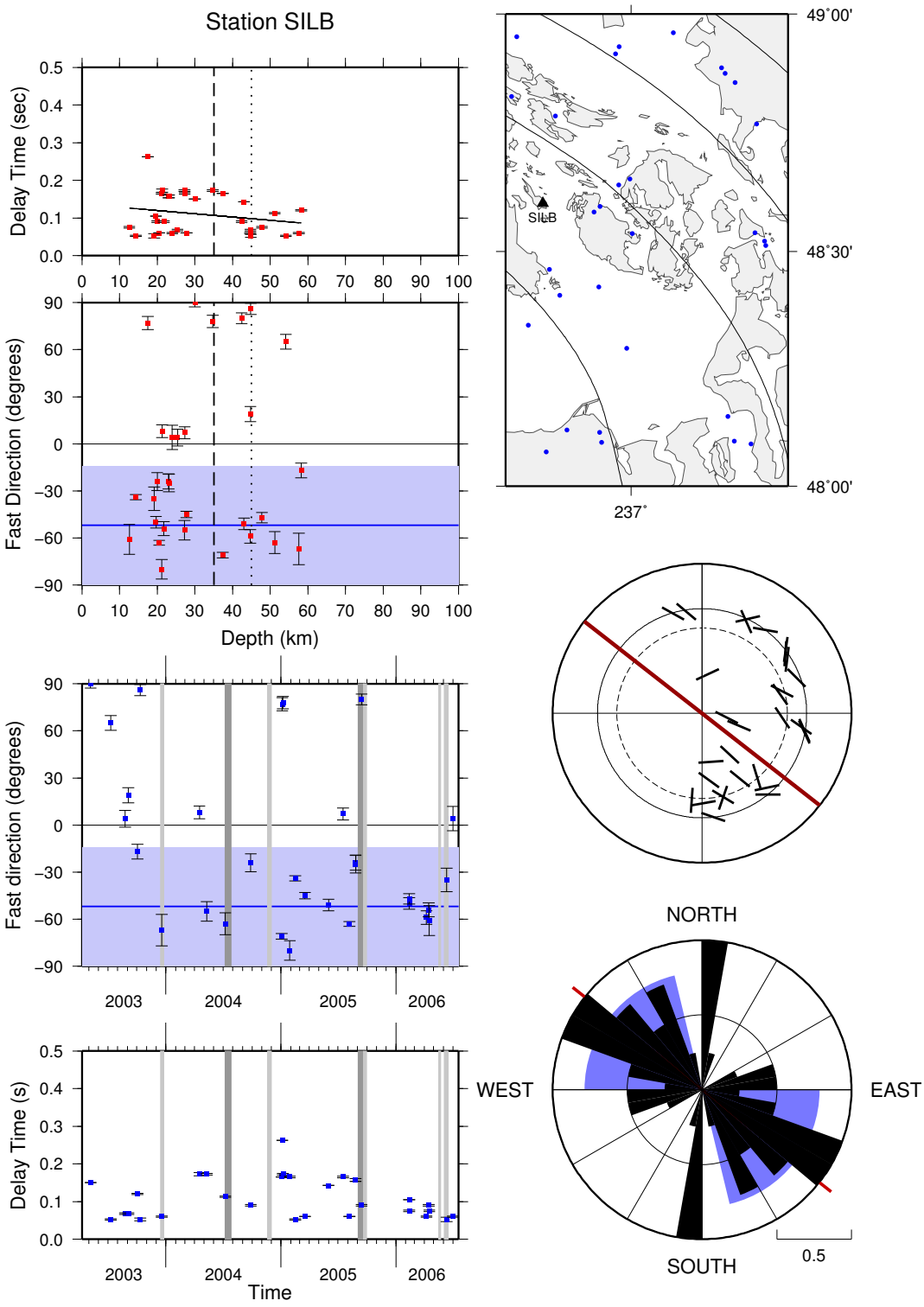

Figure B.24: Summary plots of shear-wave splitting results at station SILB.

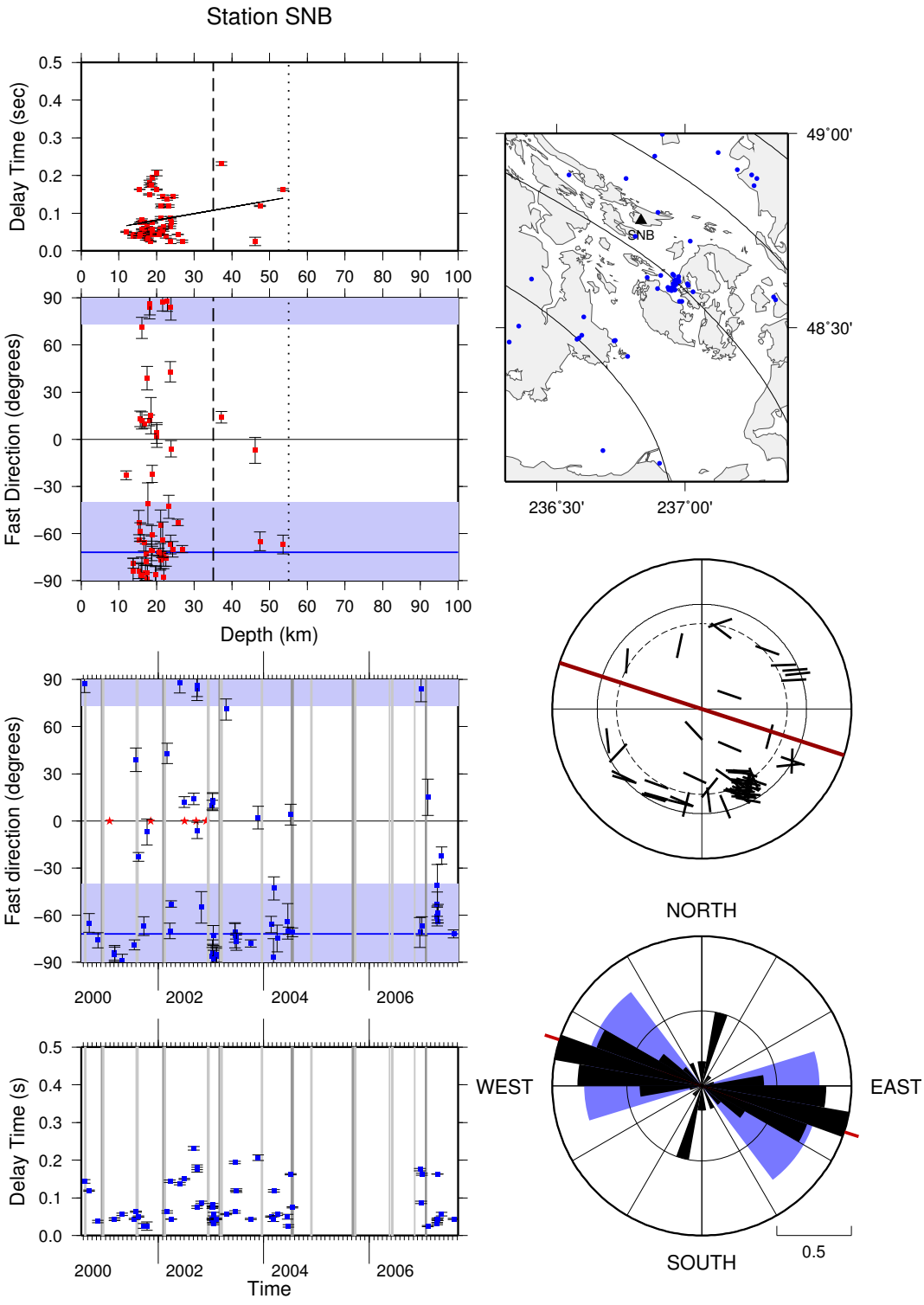

Figure B.25: Summary plots of shear-wave splitting results at station SNB.

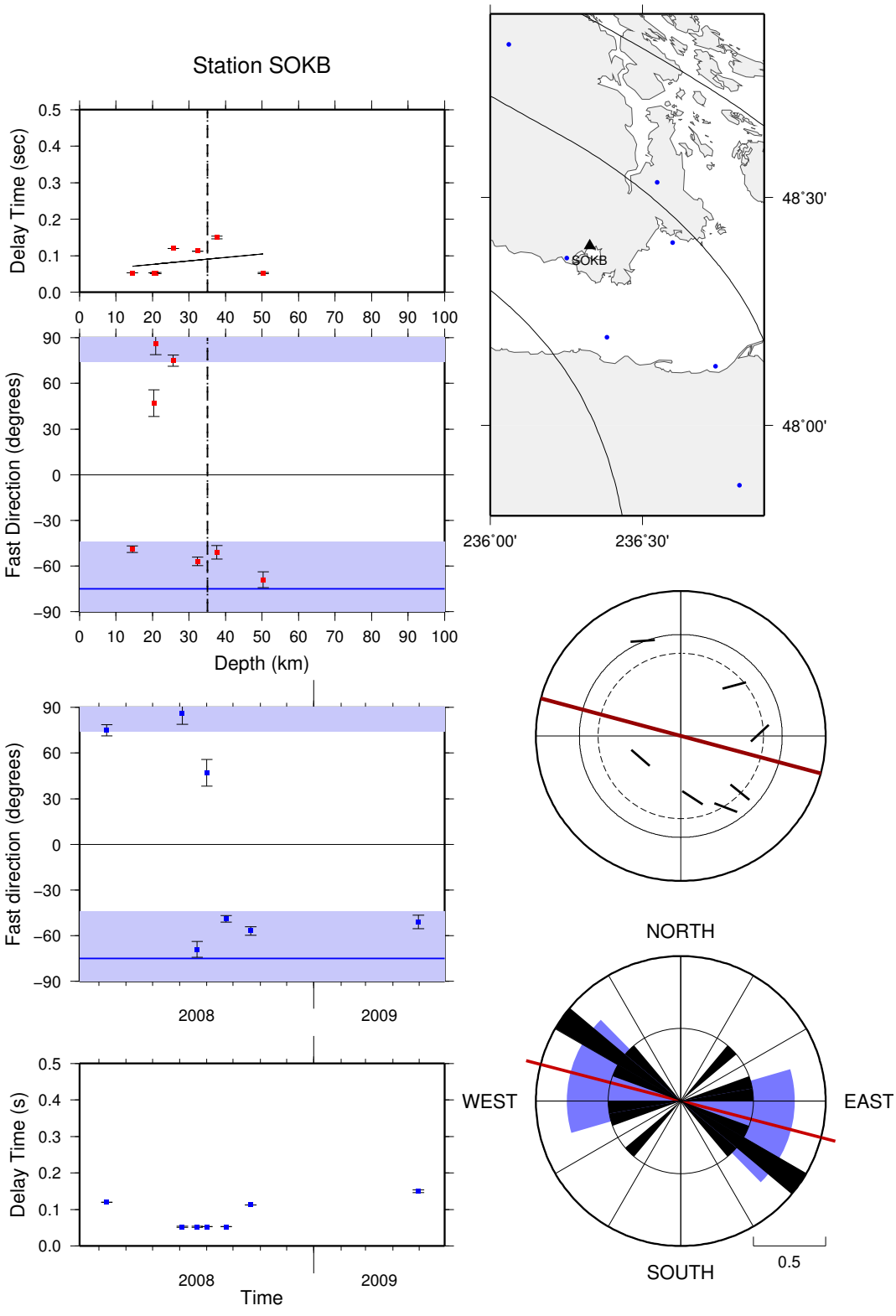

Figure B.26: Summary plots of shear-wave splitting results at station SOKB.

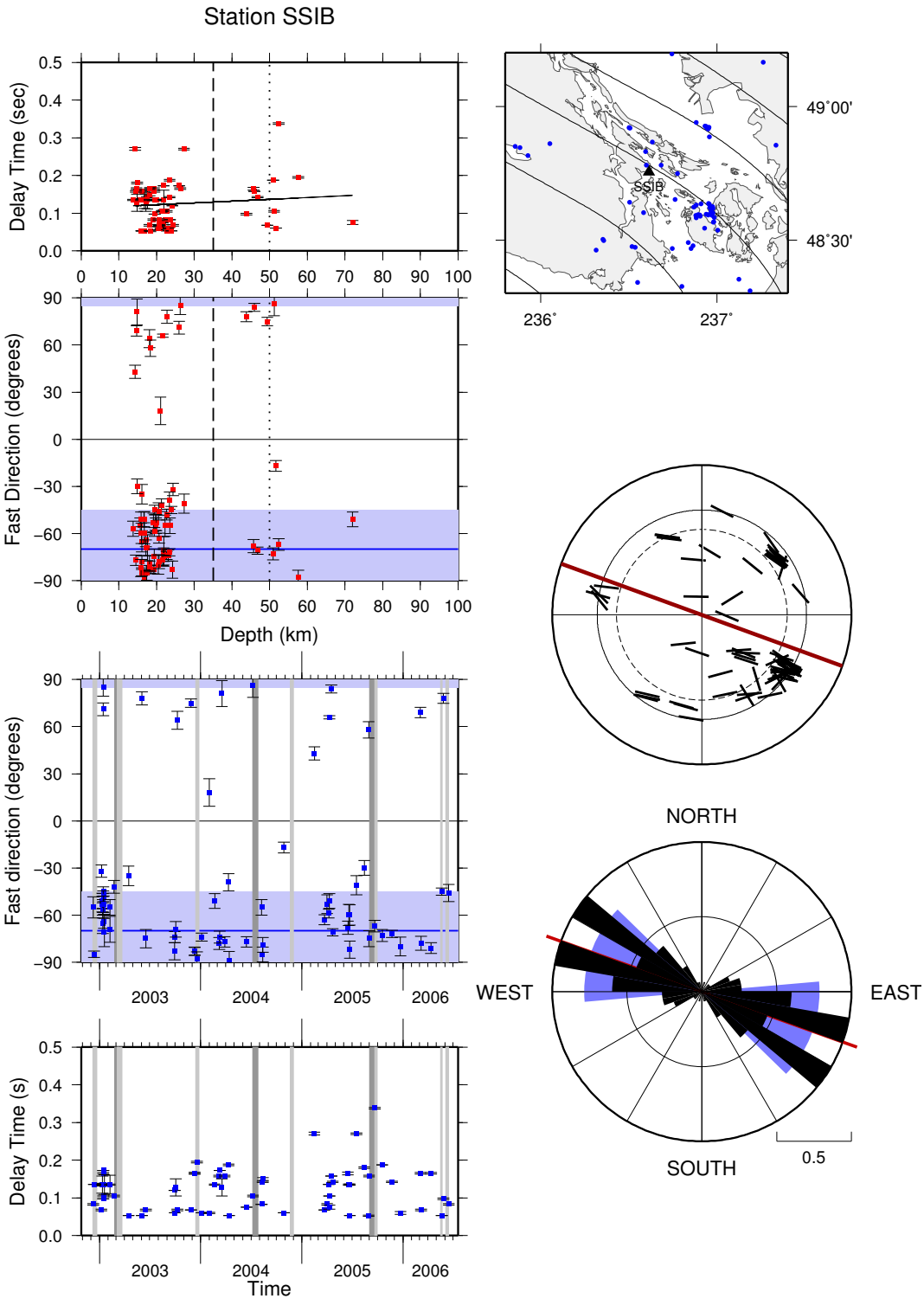

Figure B.27: Summary plots of shear-wave splitting results at station SSIB.

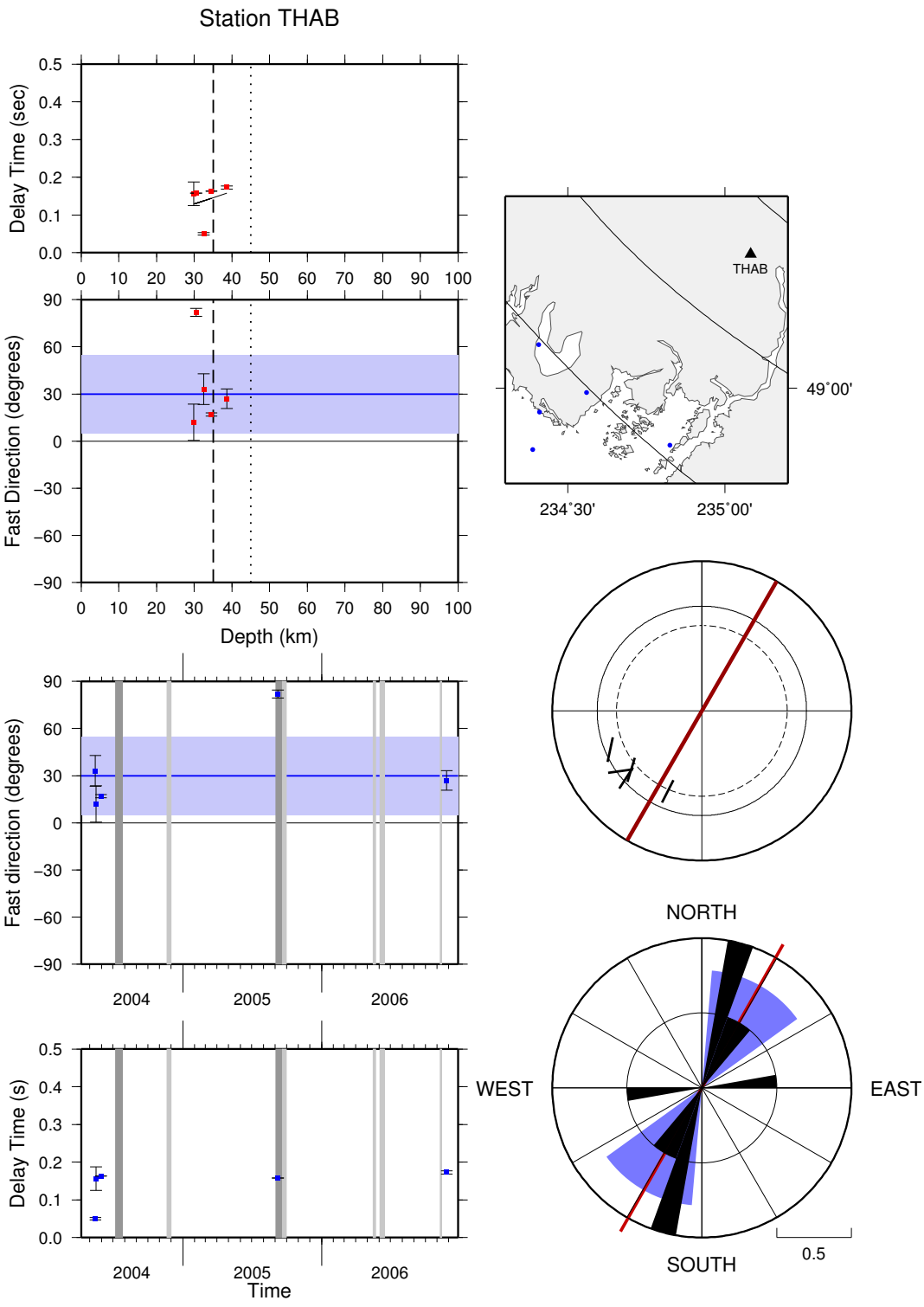

Figure B.28: Summary plots of shear-wave splitting results at station THAB.

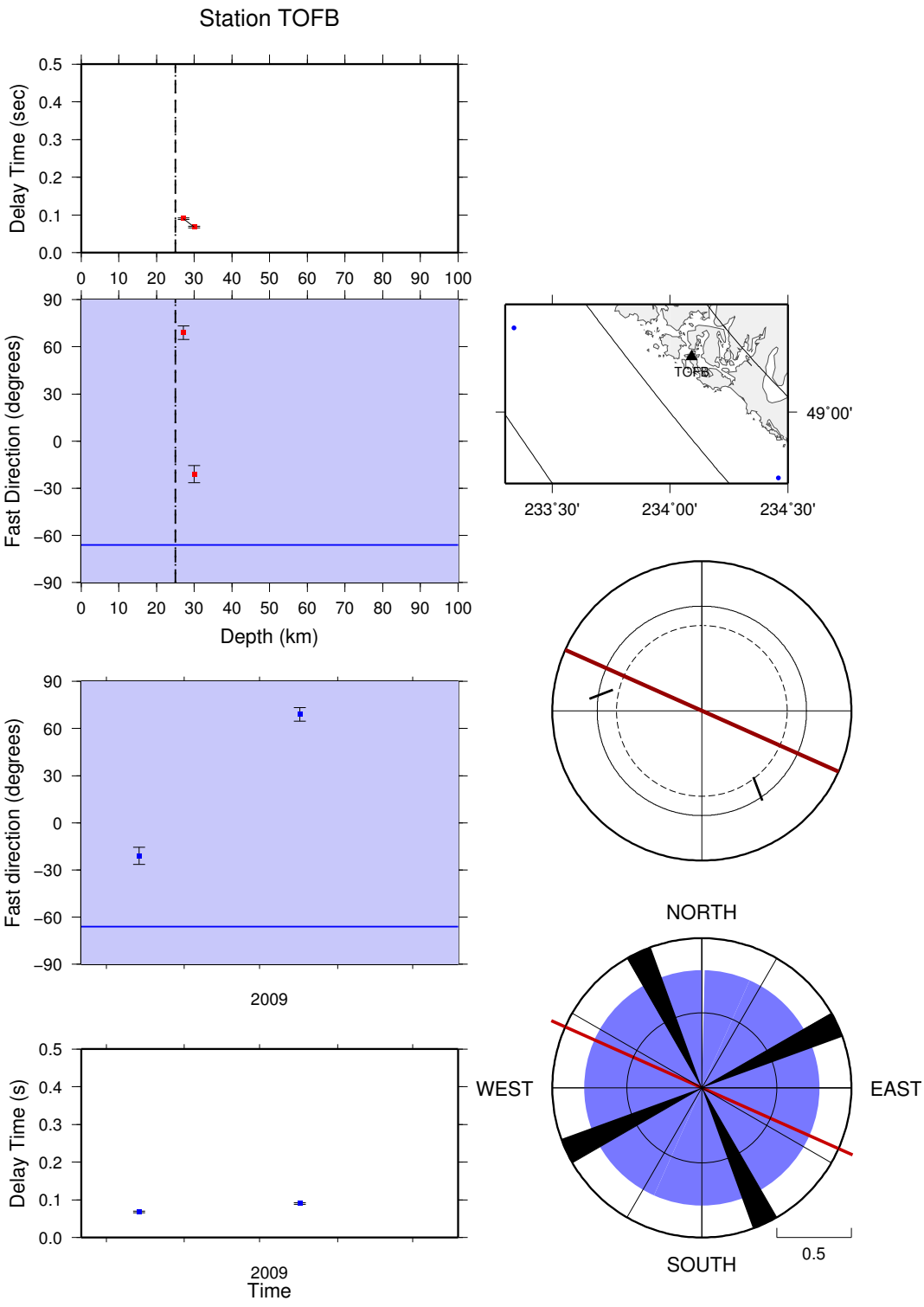

Figure B.29: Summary plots of shear-wave splitting results at station TOFB.

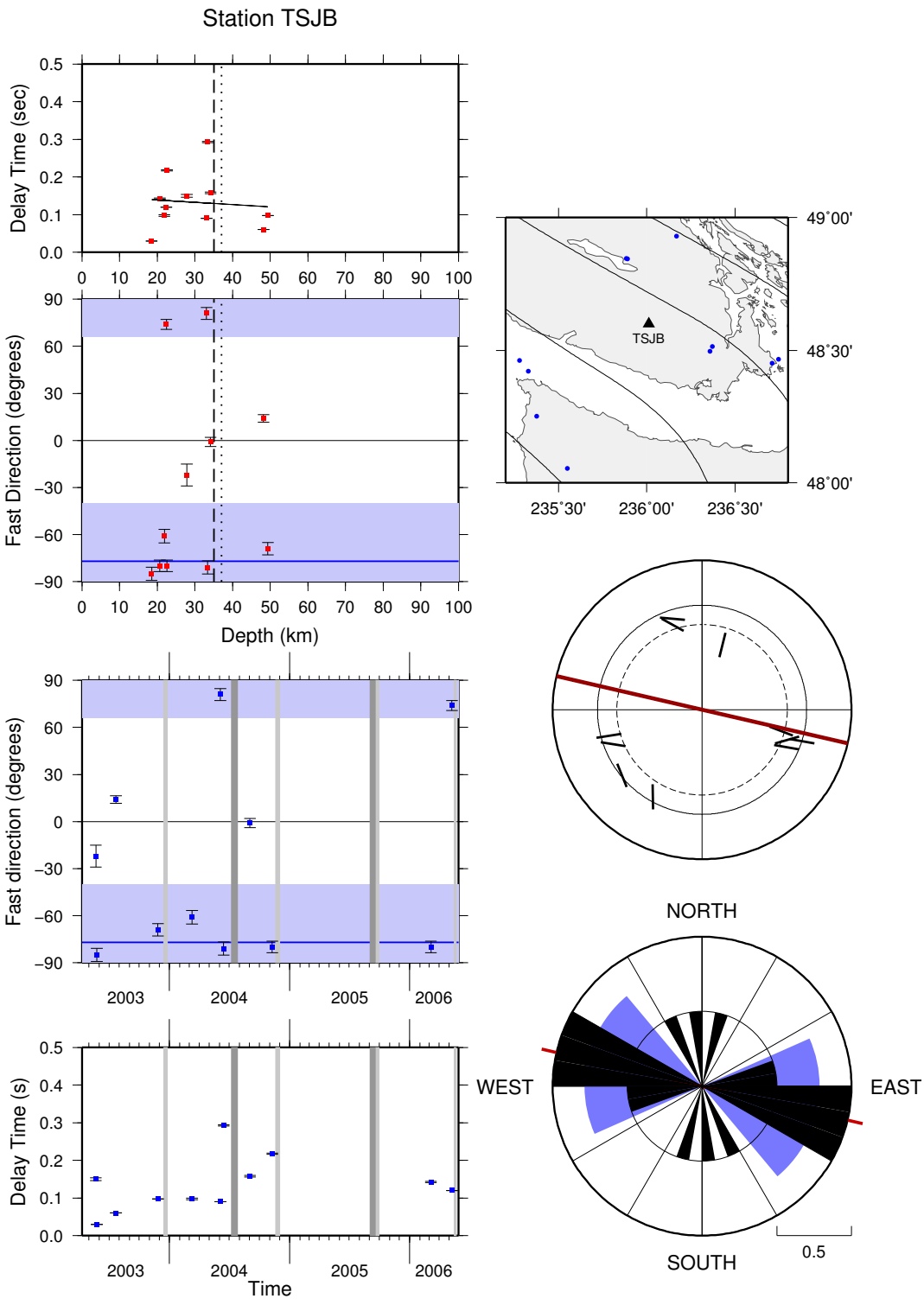

Figure B.30: Summary plots of shear-wave splitting results at station TSJB.

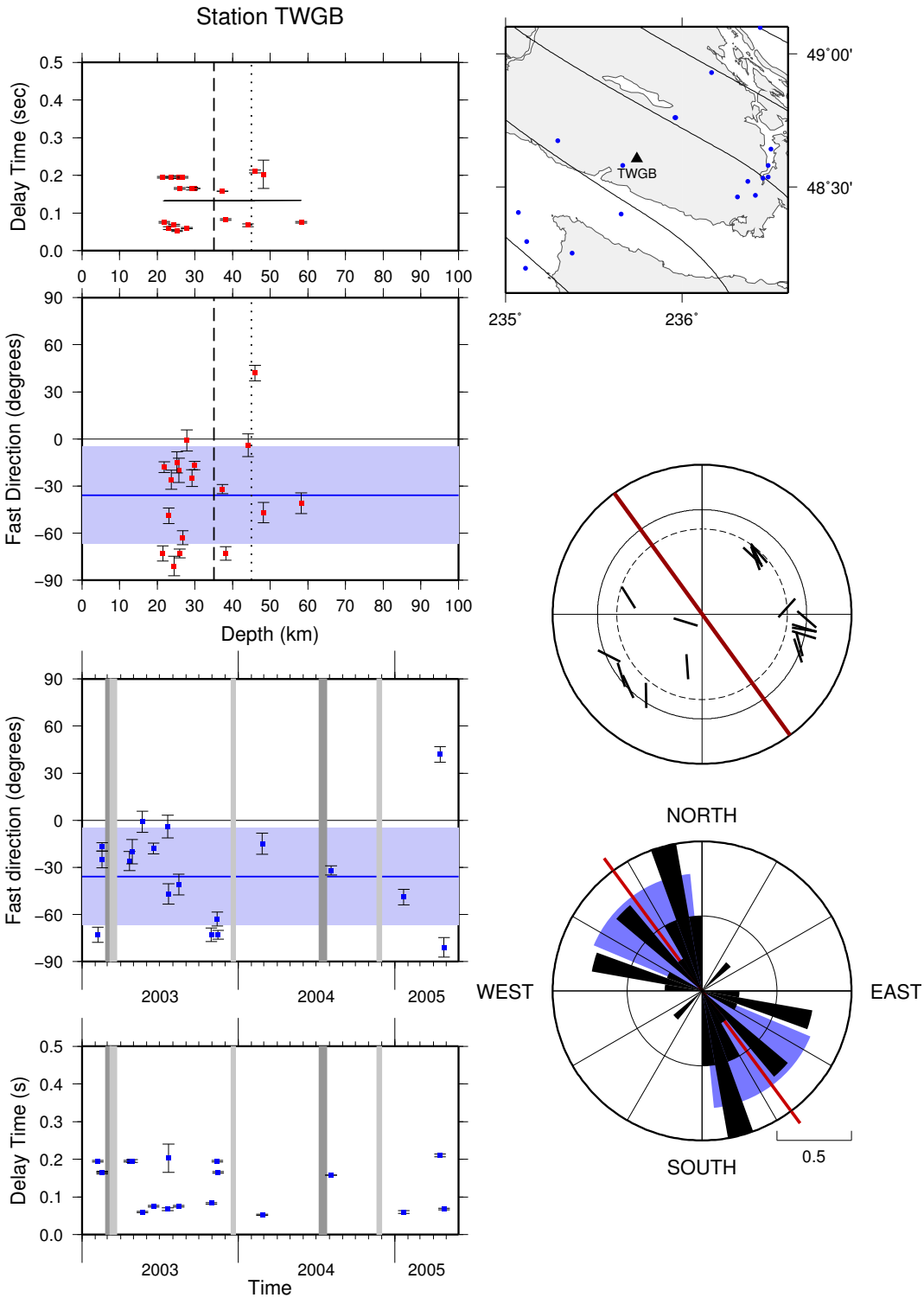

Figure B.31: Summary plots of shear-wave splitting results at station TWGB.

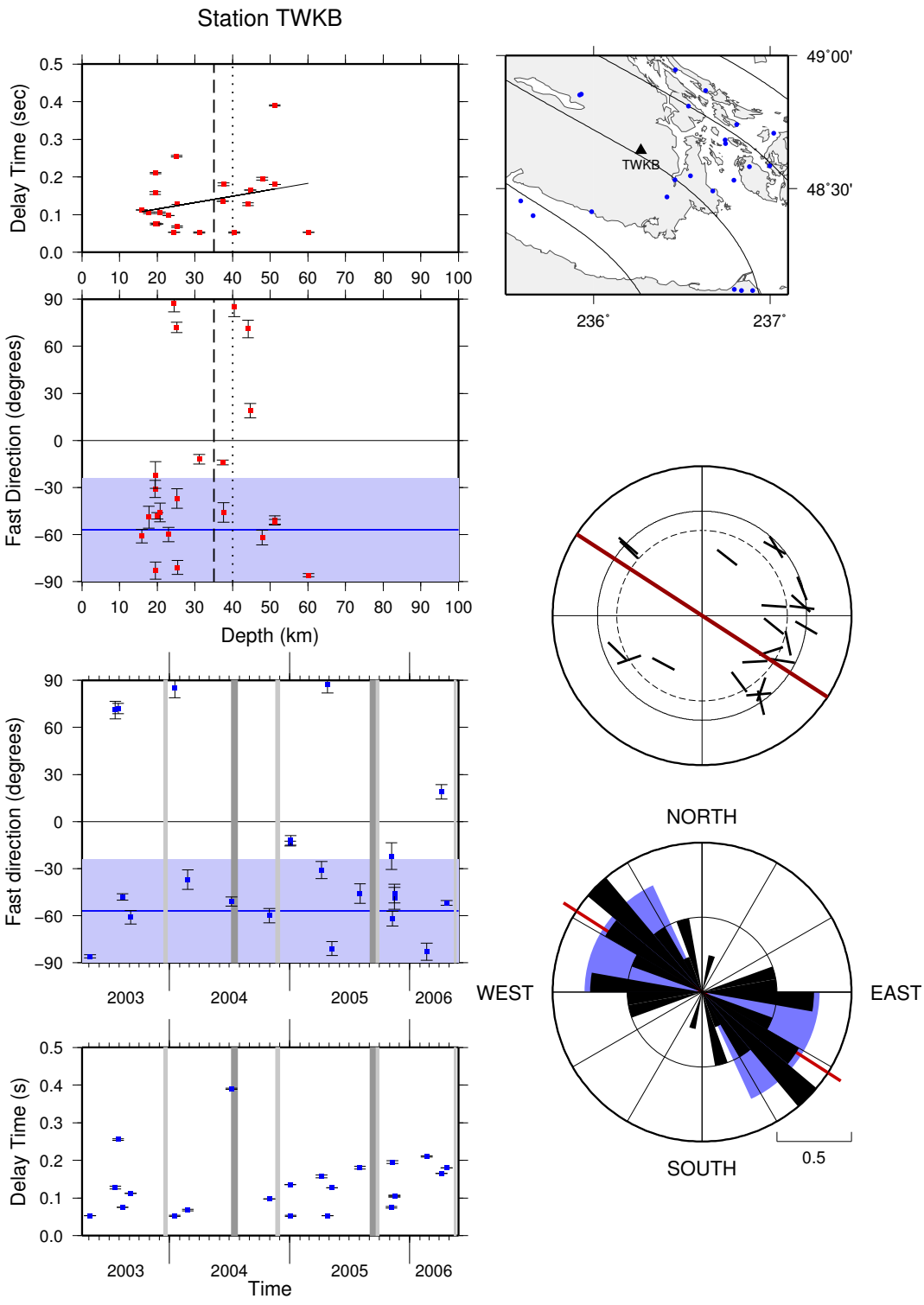

Figure B.32: Summary plots of shear-wave splitting results at station TWKB.

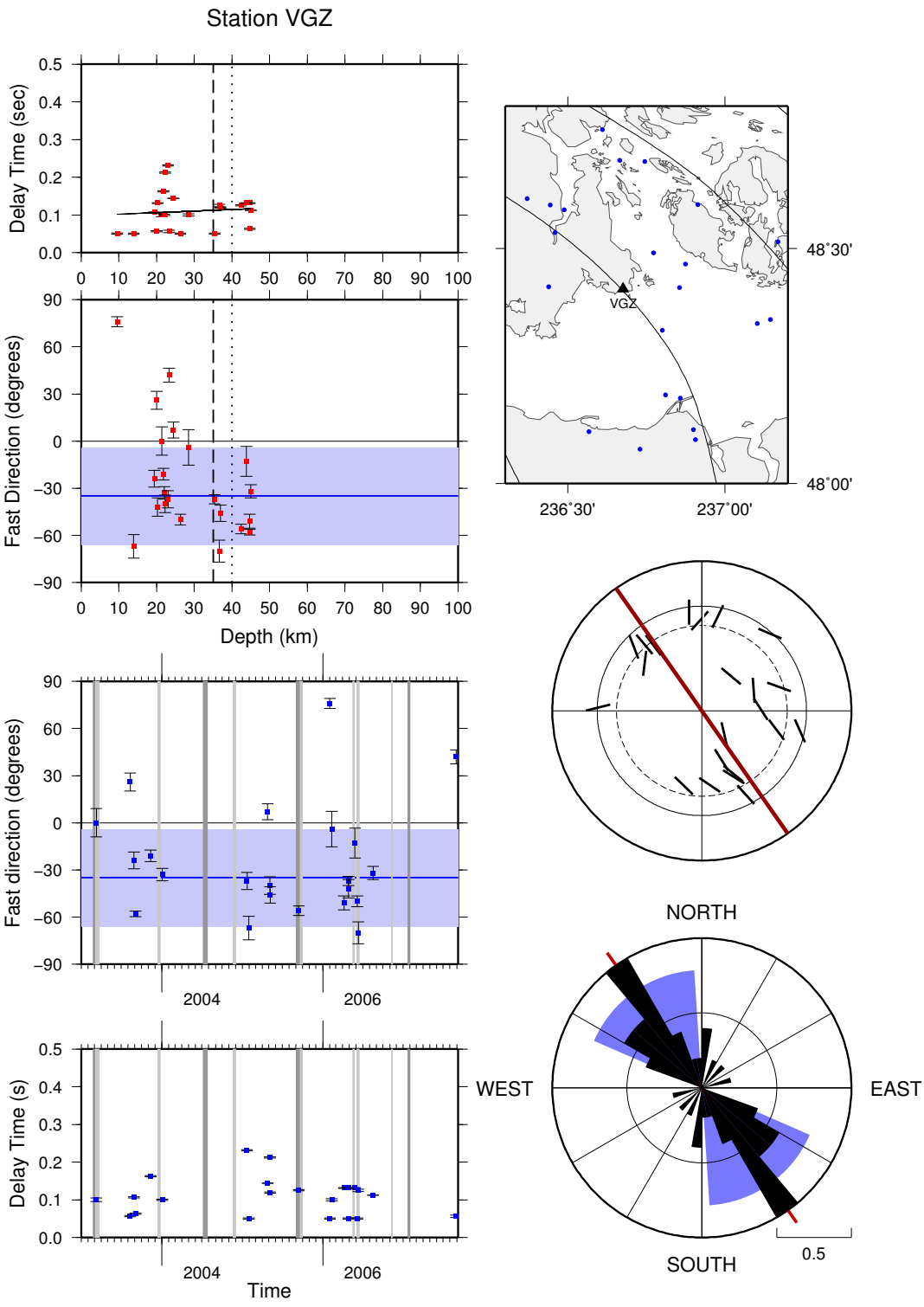

Figure B.33: Summary plots of shear-wave splitting results at station VGZ.

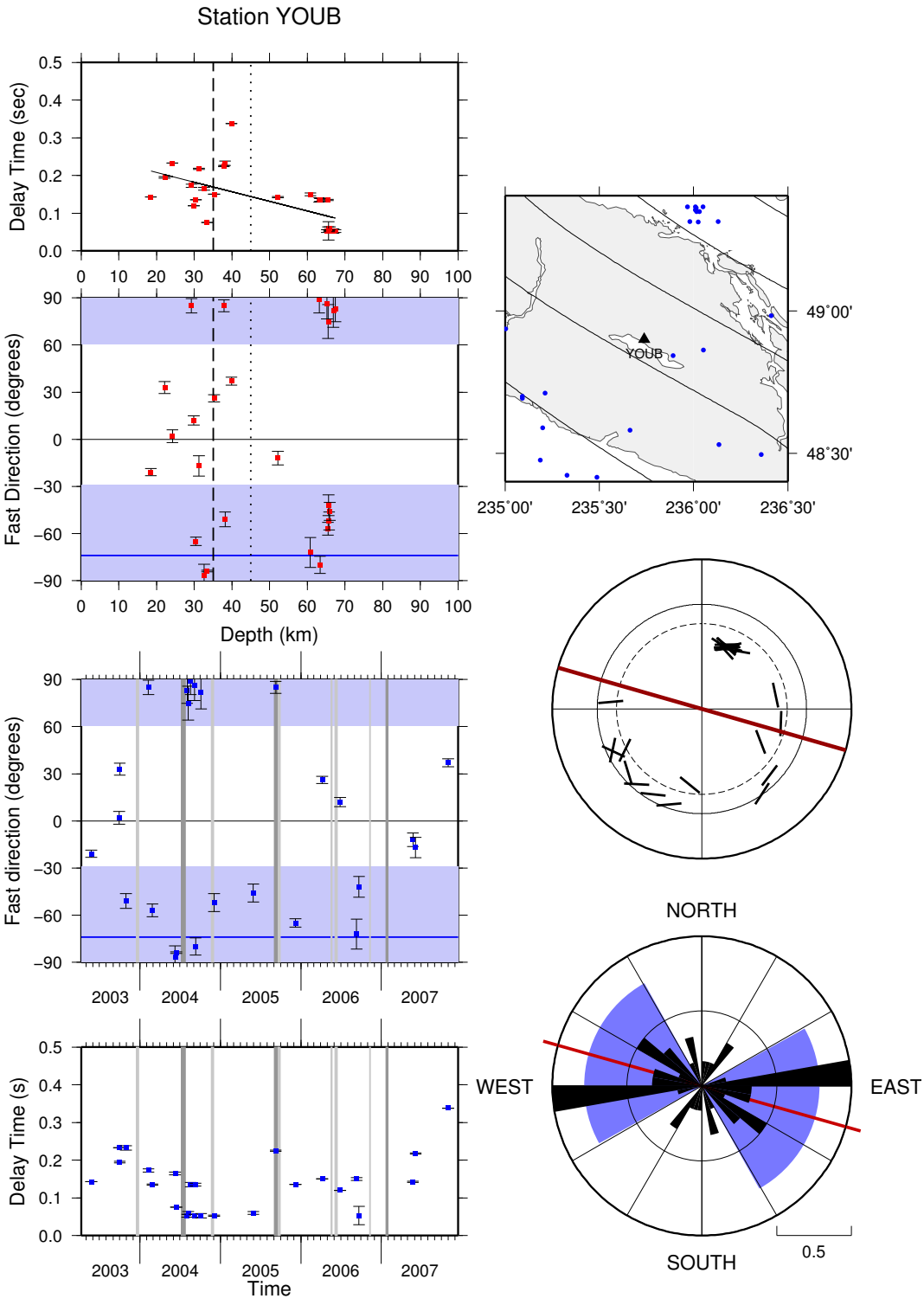

Figure B.34: Summary plots of shear-wave splitting results at station YOUB.